JPL PUBLICATION 80-77, Volume I

Control and Dynamics Study for the Satellite Power System

Volume I. MPTS/SPS Collector Dynamic Analysis and Surface Deformation

S. J. Wang

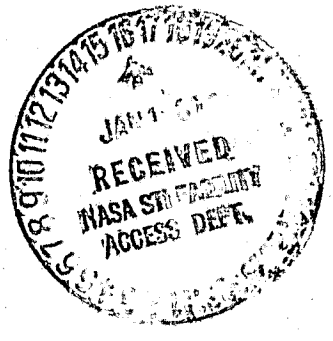

September 1, 1980

National Aeronautics and Space Administration

Jet Propulsion Laboratory
California Institute of Technology
Pasadena, California

JPL PUBLICATION 80-77, Volume I

Control and Dynamics Study for the Satellite Power System

Volume I. MPTS/SPS Collector Dynamic Analysis and Surface Deformation

S. J. Wang

September 1, 1980

National Aeronautics and
Space Administration

Jet Propulsion Laboratory
California Institute of Technology
Pasadena, California

The research described in this publication was carried out by the Jet Propulsion Laboratory, California Institute of Technology, under NASA Contract No. NAS7-100.

Acknowledgements

The author wishes to express his appreciation to R.C. Chernoff, R.M. Dickinson, J.N. Juang, S.L. Miller and G. Rodriguez of JPL, to R.C. Ried, and F.J. Stebbins of NASA JSC, and to S.V. Manson of NASA Headquarters for their valuable contributions and assistance.

Abstract

This report presents the results of Part I of the dynamics and control analysis for the MPTS antenna and collector interactions. The objectives of this part of the study have been to establish the basic dynamic properties and performance characteristics of the antenna so that the results can be used for developing criteria, requirements, and constraints for the control and structure design. Specifically, the vibrational properties, the surface deformation, and the corresponding scan loss under the influence of disturbances have been studied.

TABLE OF CONTENTS

List of Illustrations

Page

List of Tables

SECTION 1

INTRODUCTION AND SUMMARY

This report presents the results of Part I of a two-part study of the dynamics and control analysis of the MPTS* Antenna and its interaction with the solar collector. The effort reported here deals with the dynamics problem of the antenna/collector, especially the surface deformation and the effects of the power loss due to the warping of the antenna surface. The second part of this work deals with the attitude and pointing control problems which will be summarized in Volume II of this report. Although the main emphasis of this report is on the MPTS antenna, the overall results of this study apply to the SPS configuration formed by a collector structure plus two end-mounted antennas (see Fig. 1, in Section 2.2).

1.1 GENERAL BACKGROUND

The SPS is the largest space system conceived to date that appears feasible with reasonable extensions of existing control technology. It represents a class of large platform-like structures that are several orders of magnitude larger than any of the other large space systems (multiple-payload platforms, parabolic reflectors, etc.) currently in planning within NASA. The SPS has in common with all large space systems many control problems that are widely recognized within the controls community. These problems include attitude errors due to disturbances, potential instabilities due to truncated modes and other model errors, lack of damping, inaccurate preflight knowledge of the vehicle dynamics, and the parameter variations while the system is in operation. The qualitative nature of these problems (model errors, concentrated stresses due to large actuator size, etc.) has emerged as a result of studies in the general area of control of large space structures. However, there is a need at this time to investigate the dynamics and control problems specifically related to the Satellite Power System to assess performance of selected control concepts, and to identify and initiate development of advanced control technology that could enhance feasibility and performance of the

*MPTS stands for Microwave Power Transmission System.

SPS system. Two of the areas that have been under investigation are the dynamics and control of the solar collector with the MPTS antennae treated as point masses and the dynamics and control of the MPTS antenna with the solar collector treated as a dynamic disturbance source. This report covers the most basic problems of the latter, that is, the dynamic properties and the performance characteristics of the MPTS antenna.

It is a known fact that the losses accrued at the later stages of a process are more costly than those accrued at the early stages. This is also true in the context of the power collection-conversion-transmission process of the SPS system. Since the antenna power transmission constitutes the last part of the efficiency chain for the in-orbit operation, a great deal of emphasis has been made directly to the pointing accuracy. However, due to the high weight penalty at synchronous altitude and the huge array size (1000-meter diameter), the structure cannot be made arbitrarily rigid, and the structure stiffness and hence the surface deformation of the antenna plays an important role in the determination of the performance of the antenna. It is this latter subject area which this study is focussed on.

1.2 PERFORMANCE REQUIREMENT GUIDELINE

In References 2 and 3, the requirement of mechanical pointing and alignment accuracy of 2 to 3 arc minutes has been considered. In this report, the performance requirement of 3 arc minutes for the surface flatness is used as a base for discussion.

1.3 OBJECTIVES AND SCOPE

The combination of flexibility, huge dimensions, high disturbances, and the nature of the operation make the MPTS/SPS antenna uniquely different from any antenna or spacecraft that the aerospace community has ever designed. The objectives of this part of the study have been to establish the basic dynamic properties and performance characteristics of the antenna so that this knowledge can be utilized to form a new base, requirement, and constraints to aid the control system design. Specifically, the following subject areas have been addressed based on the most up-to-date MPTS data,

1. The vibrational properties such as the mode shapes and natural frequencies of the antenna and their effect to the SPS structure properties as a whole.
2. The surface deformation of the antenna structure and its effect on the scan losses.
3. The effects of disturbances including thermal distortions of the solar collector to the flatness of the antenna surface.
4. Application of the linear analysis technique to extend the results obtained through simulation.

The approach employed here has been one of the time domain analysis techniques, i.e., a combined modeling, analysis, and computer simulation approach.

In Section 2, the necessary mathematical formulations of the model and the performance related terms and quantities are presented. The structural flexibility properties, the estimates of the disturbances, the thermal effects, the dynamic interactions, and the main results of the simulation and their linear extensions are presented in Section 3.

1.4 STUDY RESULTS AND CONCLUSIONS

The main contribution of this part of the study is that it has established the performance characteristics of the antenna, especially the local warping and its effects on the antenna scan losses. The performance characteristics are plotted as time histories of a number of quantities and they have also been summarized in tabulated forms in Section 3. In addition, these results have been extended in the parameter space as shown in Figs. 23, 24, and 25 (these figures are reproduced here for quick reference).

Throughout this study, a great deal of insight and experience have been gained such as how certain types of vibration modes react to given types of signals (forcing functions) and their position of execution; how modal dominance varies with the frequencies and the properties of the forcing functions; the importance of signal shaping and timing; the distribution of modal energy and its time dependence, etc. All of these are invaluable information for the control system design.

Computer simulation programs have been developed which have proved to be an effective and necessary tool for this study and it will be an essential part of the facility for our future work. These programs are listed in Appendices A and B for reference purposes.

The major conclusions of this study are as follows:

1. The structural damping is essential for the maintenance of a flat radiation surface. This is especially important for dissipating the otherwise prolonged presence of high surface transient caused by disturbances. The decay rate of the surface deformation in general agrees with that of the amplitude of the dominant mode. A structure damping ratio of .005 has been used; a higher value will be more desirable.
2. The most significant sources of disturbance that affect the antenna performance perhaps come from the dynamic and control interactions between the antenna and the collector. The effects of these disturbances may be reduced significantly by
    a. decoupling the antenna from the collector motions, especially the translational motions;
    b. actively controlling the collector bending motions at the interface boundary. Large amplitude oscillations at the collector tips must be actively suppressed.

    Figures 23 and 24 show the performance characteristics of the antenna surface as a function of the amplitude of oscillation (cosine function) for collector bending and torsional motions, respectively. A suddenly applied bending oscillation of slightly over 1/4000 of the length of a 20 km collector will cause a maximum RMS local slope angle of 0.05° or 3 arc minutes.

3. External disturbances such as the gravity gradient, solar pressure, etc., will not have a direct impact on the surface flatness with the possible exception of the thermal distortion of the collector structure. High temperature gradient with short thermal lag time after shadowing, can set the collector to sudden bending oscillation. Unless low coefficient of thermal expansion (CTE) graphite composite material is used, this could be a source of serious problems. Figure 25 shows the estimates of the collector bending amplitude as a function of the CTE for a number of temperature gradient values. By using this estimate with the performance data of Fig. 23, a suitable CTE value may be determined.
4. Signal shaping and timing are of critical importance to the performance of the MPTS/SPS system. The shape of an actuator force should be designed so that the least amount of energy may be absorbed by the flexible modes. The cut off time of a thrusting force determines the amount of energy left in the flexible modes. To reduce the level of surface vibration, the modal state of the dominant mode should be monitored so that the cutoff of a major thruster should be timed such that the modal energy of this mode is at its minimum.
5. The MPTS/SPS has the following structural properties:
    a. The natural frequencies of the antenna and the SPS are 2 to 3 orders of magnitude greater than the orbital frequency. That means that these modes and orbit will not couple.
    b. The frequency of the lowest flexible mode of the antenna is about one order of magnitude greater than that of the collector. However, the first 3 flexible modal frequencies of the MPTS overlap with the 8th of the collector, and the excitation of the latter should be avoided.

c. Due to its location, the antenna mass will have more influence on the SPS normal frequencies than the same mass distributed over the solar collector. The antenna mass is about 30% of the total SPS mass, its existence has decreased the fundamental frequency by a factor of 0.4 and its effect on the higher frequencies is less [5]. The stiffness of the coupling structure also affects the normal frequencies. The significance of these effects to design alterations are yet to be determined.

d. The most significant factors that affect the modal properties are the geometrical parameters of the structure.

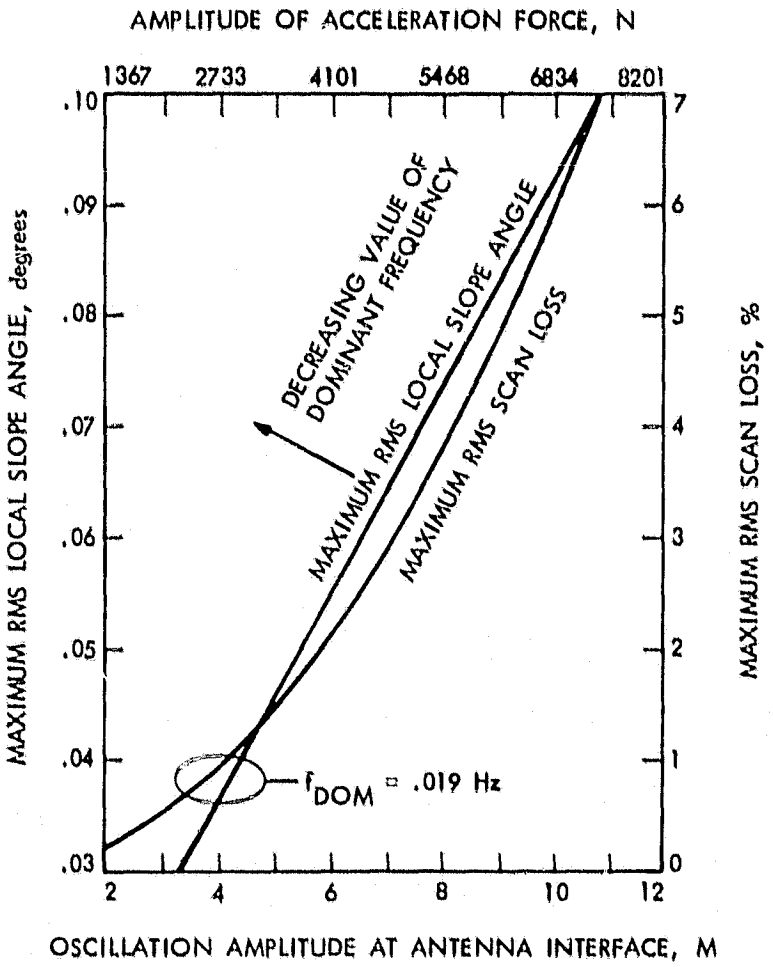

Figure 23. MPTS Surface Deformation vs. Amplitude of Collector Bending Oscillation

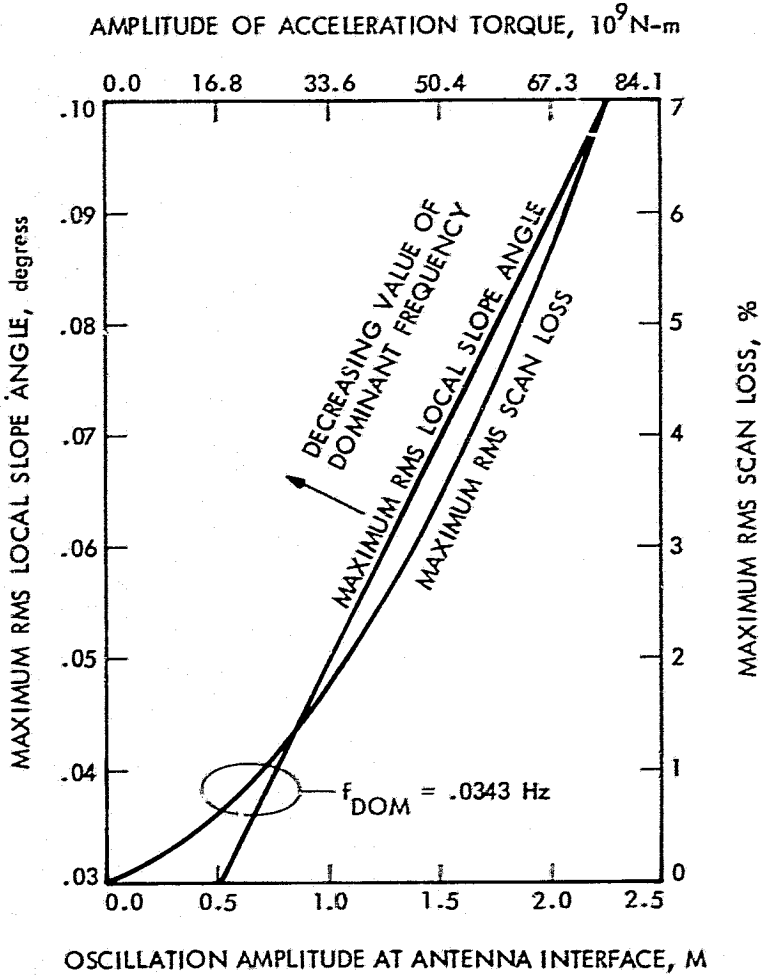

Figure 24. MPTS Surface Deformation vs. Amplitude of Collector Torsional Oscillation

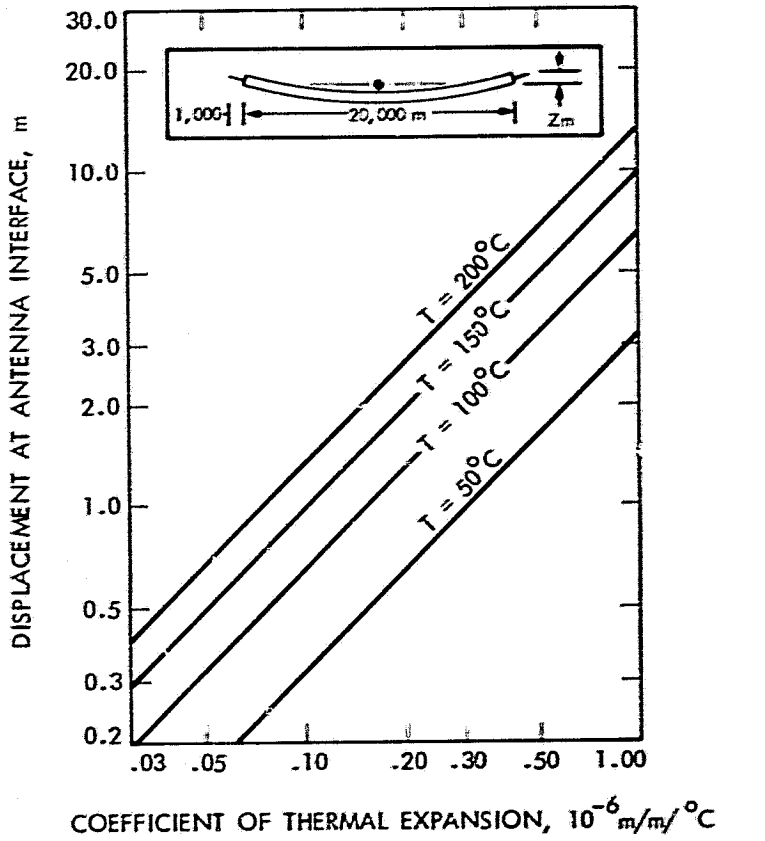

Figure 25. Collector/Antenna Boundary Displacement vs. Coefficient of Thermal Expansion of Solar Collector Structure

SECTION 2

DYNAMIC MODEL AND PERFORMANCE RELATED EQUATIONS

2.1 THE DYNAMIC EQUATIONS AND ENERGY OF CONCENTRATED MASSES

Dynamic Equations

In Reference 1, finite element models of the MPTS antenna have been discussed. In this section only the key elements of the model that have been implemented in the simulation programs are discussed.

The model consists of 20 decoupled second order differential equations representing the modal amplitudes of the 6 rigid body modes and the 14 lower order flexible modes,

$$\underline{M}\ddot{q} + \underline{K}q = \underline{\Phi}^T f \tag{1}$$

where q is the 20-modal amplitude vector; f, the 498-force vector; $\underline{M}$ and $\underline{K}$ are the 20x20 generalized mass and generalized stiffness matrices (both diagonal), respectively; and $\underline{\Phi}$ is the matrix of eigenvectors of dimension 498x20. For convenience, (1) is written in the following form,

$$\ddot{q} + \underline{\Lambda}q = \underline{\tilde{\Phi}}^T f \tag{2}$$

where

$$\underline{\Lambda} = \underline{M}^{-1}\underline{K} = \begin{bmatrix} \ddots & \\ & \omega_k^2 \\ & & \ddots \end{bmatrix} \tag{3}$$

where ω_k is the angular frequency of the kth mode for k=7,...,20 and $\omega_k = 0$ for k=1,...,6; and

$$\underline{\tilde{\Phi}} = \underline{\Phi}(\underline{M}^{-1})^T = \underline{\Phi}\ \underline{M}^{-1} \qquad (\underline{M} \text{ is diagonal}) \tag{4}$$

In this study, structural damping is also considered. Since there is no available information, a damping term, with $\zeta = .005$, has been added to the kth flexible mode as follows, in the expanded form,

$$\ddot{q}_k = \phi_k^T M_k^{-1} f \quad , \qquad k=1,...,6 \tag{5a}$$

$$\ddot{q}_k + 2\zeta\omega_k\dot{q} + \omega_k^2 q = M_k^{-1}\,\phi_k^T\, f, \qquad k=7,\ldots,20 \qquad (5b)$$

where ϕ_k is the kth column of $\underline{\Phi}$ and M_k^{-1} is the kth diagonal element of $\underline{M}_k^{-1}$. Since these equations are linear time invariant, analytical solutions are readily known. Compact solutions were therefore used in the simulation programs instead of the more time consuming methods of numerical integrations. In the following, let T be the interval of each computation step, and $\phi = \omega_k\sqrt{1-\zeta^2}\,T$, $C_\phi = \cos\phi$, $S_\phi = \sin\phi$, and $q(n) \triangleq q(nT)$, then in each computation step, the following is evaluated,

For k = 1,...,6

$$\begin{bmatrix} q(n+1) \\ \dot{q}(n+1) \end{bmatrix} = \begin{bmatrix} 1 & T \\ 0 & 1 \end{bmatrix} \begin{bmatrix} q(n) \\ \dot{q}(n) \end{bmatrix} + \begin{bmatrix} T^2/2 \\ T \end{bmatrix} \phi_k^T\, M_k^{-1}\, f(n) \qquad (6a)$$

For k = 7,...,20

$$\begin{bmatrix} q(n+1) \\ \dot{q}(n+1) \end{bmatrix} = e^{-\zeta\omega_n T} \begin{bmatrix} C_\phi + \frac{\zeta}{\sqrt{1-\zeta^2}} S_\phi & \frac{1}{\omega_k\sqrt{1-\zeta^2}} S_\phi \\ -\frac{\omega_k}{\sqrt{1-\zeta^2}} S_\phi & -\frac{\zeta}{\sqrt{1-\zeta^2}} S_\phi + C_\phi \end{bmatrix} \begin{bmatrix} q(n) \\ \dot{q}(n) \end{bmatrix}$$

$$+ \frac{1}{\omega_k^2} \begin{bmatrix} 1 - e^{-\zeta\omega_k T}\left(C_\phi + \frac{\zeta}{\sqrt{1-\zeta^2}} S_\phi\right) \\ \frac{\omega_k}{\sqrt{1-\zeta^2}} S_\phi \end{bmatrix} \phi_k^T\, M_k^{-1}\, f(n) \qquad (6b)$$

where f(n) is the force vector evaluated at t = nT and n = 0,1,...,t_f/T; t_f is the final time.

With the availability of q_k, the displacement of node i, i = 1,...,166, due to elastic deformation alone, at t = nT, can be evaluated as the linear combination of q_k, i.e.,

$$u_i(n) = \sum_{k=7}^{20} \phi_{ki}\, q_k(n) \tag{7a}$$

$$v_i(n) = \sum_{k=7}^{20} \phi_{k(166+i)}\, q_k(n) \tag{7b}$$

$$w_i(n) = \sum_{k=7}^{20} \phi_{k(332+i)}\, q_k(n) \tag{7c}$$

and the displacement due to the rigid body modes,

$$\bar{u}_i(n) = \sum_{k=1}^{6} \phi_{ki}\, q_k(n) \tag{8a}$$

$$\bar{v}_i(n) = \sum_{k=1}^{6} \phi_{k(166+i)}\, q_k(n) \tag{8b}$$

$$\bar{w}_i(n) = \sum_{k=1}^{6} \phi_{k(332+i)}\, q_k(n) \tag{8c}$$

The actual position of node i, at t = nT, is

$$x_i(n) = X_i + \bar{u}_i(n) + u_i(n) \tag{9a}$$

$$y_i(n) = Y_i + \bar{v}_i(n) + u_i(n) \tag{9b}$$

$$z_i(n) = Z_i + \bar{w}_i(n) + w_i(n) \tag{9c}$$

where X_i, Y_i, Z_i are the coordinates of node i when the system is at rest. Equation (9) was used to generate the antenna surface and the local slopes with the rigid body motion suppressed, i.e.,

$$\bar{x}_i(n) = X_i + u_i(n) \tag{10a}$$

$$\bar{y}_i(n) = Y_i + v_i(n) \tag{10b}$$

$$\bar{z}_i(n) = Z_i + w_i(n) \tag{10c}$$

where $(\bar{x}_i(n), \bar{y}_i(n), \bar{z}_i(n))$ may be interpreted as the coordinates of node i at t = nT projected onto the body frame, whereas $(x_i(n), y_i(n), z_i(n))$ is that expressed in terms of an inertia frame.

Energy of Concentrated Masses

The body energy of concentrated masses is of great interest to this analysis since it is a good measure of modal activities of the antenna

under disturbance. Let E be the sum of kinetic and potential energy of the antenna. Recall that the antenna is modelled as a collection of concentrated masses which are connected and having finite stiffness. E may be expressed

$$E = \frac{1}{2} \dot{x}^T \underline{m} \dot{x} + \frac{1}{2} x^T \underline{k} x \tag{11}$$

Since $x = \underline{\Phi} q$ and $\underline{M} = \underline{\Phi}^T \underline{m} \underline{\Phi}$, $\underline{K} = \underline{\Phi}^T \underline{k} \underline{\Phi}$, (11) becomes,

$$E = \frac{1}{2} \dot{q}^T \underline{M} \dot{q} + \frac{1}{2} q^T \underline{K} q \tag{12}$$

Recall that $\underline{M}$ and $\underline{K}$ are diagonal. E may be written in terms of its modal components,

$$E_k = \frac{1}{2} M_k \dot{q}_k^2 \qquad K = 1,\ldots,6 \tag{13a}$$

$$E_k = \frac{1}{2} M_k (\dot{q}_k + \omega_k^2 q_k^2), \qquad K = 7,\ldots,20 \tag{13b}$$

Let E_R and E_F be the rigid body energy and the flexible body energy, respectively, then

$$E_R = \frac{1}{2} \sum_{k=1}^{6} M_k \dot{q}_k^2 , \tag{14a}$$

$$E_F = \frac{1}{2} \sum_{k=7}^{20} M_k (\dot{q}_k^2 + \omega_k^2 q_k^2) \tag{14b}$$

and

$$E = E_R + E_F \tag{14c}$$

Since q_k and $\dot{q}_k$ are computed in each step, the energy E_k, E_R, E_F, and E can be readily evaluated. It will be illustrated later that the modal energy is indeed a good measure for determining the relative dominance of the modal activity. Further, it may be used as a measure for signal shaping and thrust on-off timing.

2.2 LOCAL SLOPES OF THE SECONDARY STRUCTURE

The basic architecture of the MPTS antenna consists of two parts, the primary structure and the secondary structure (Fig. 1). The

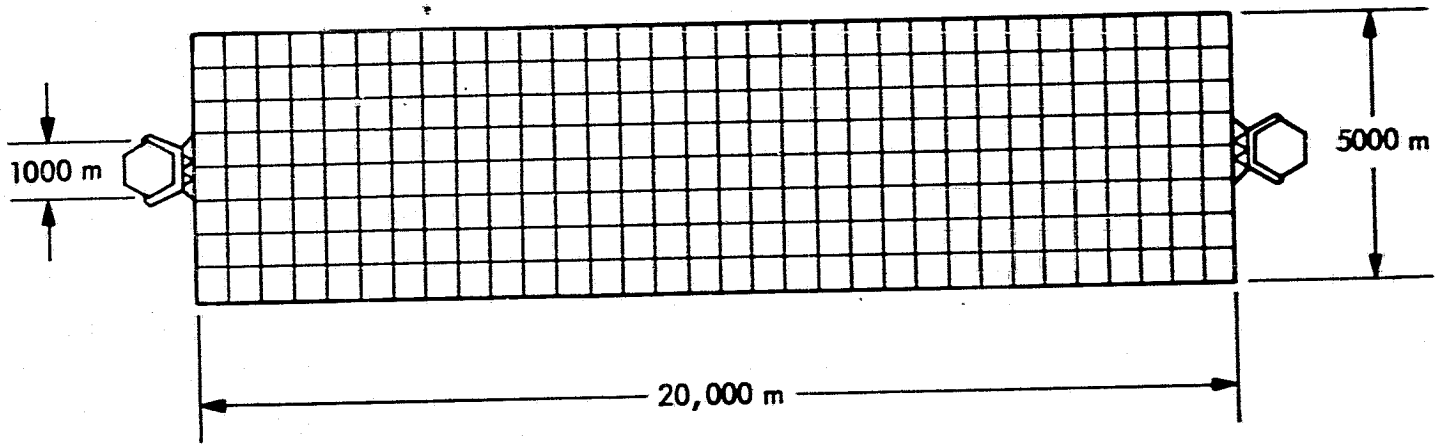

(a) THE "FULL" SPS CONFIGURATION (DIMENSIONS NOMINAL)

Figure 1. The MPTS/SPS System Configuration

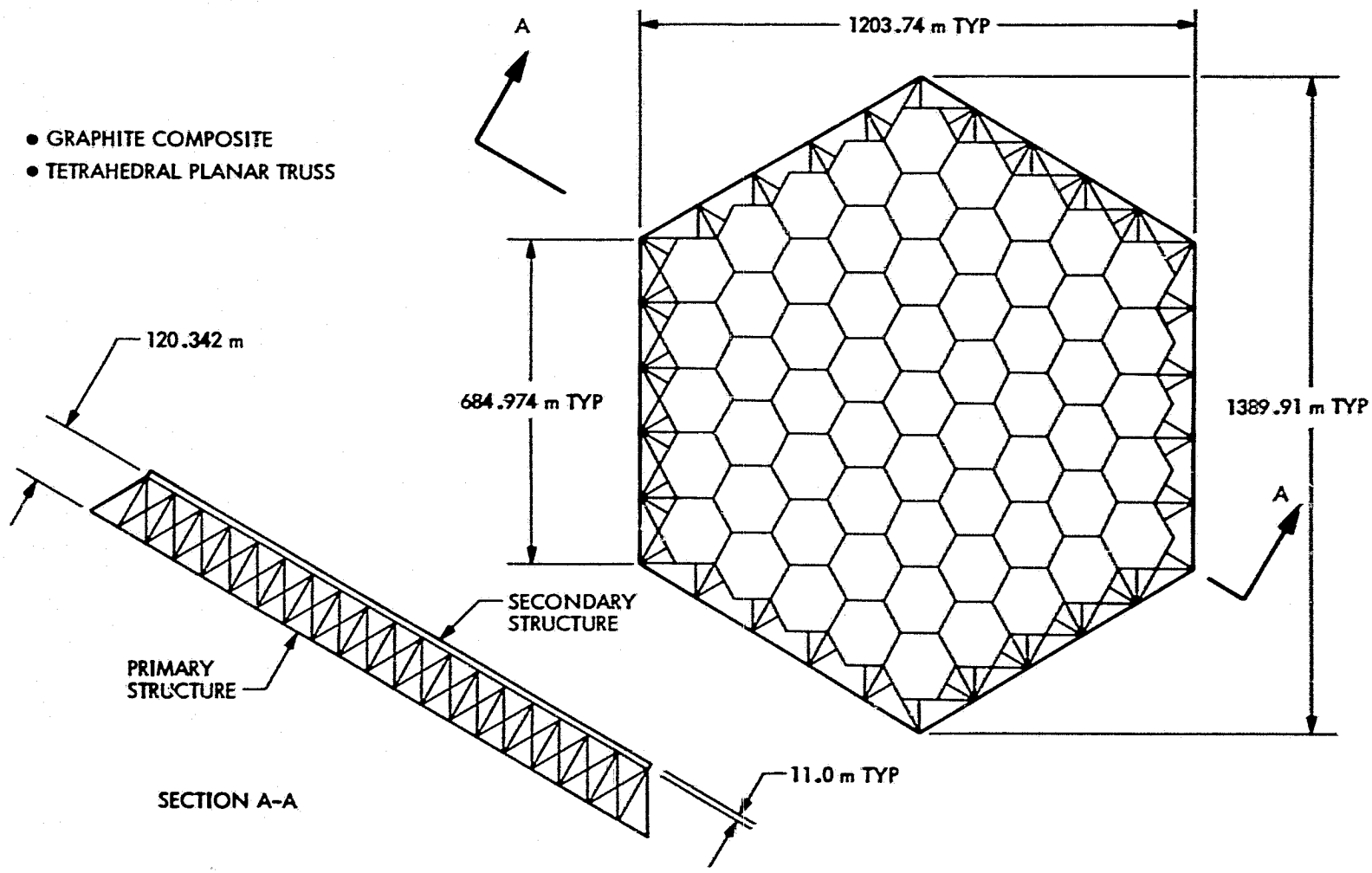

(b) THE MPTS ANTENNA STRUCTURE (REF. 2)

Figure 1. The MPTS/SPS System Configuration (Cont.)

primary structure is a tetrahedral planar truss structure which serves as the base support to the system and provides the required structural stiffness. The secondary structure is a "finer" structure which is mounted on top of the primary and it provides a base for the installation of subarrays of the antenna. Due to the huge size (1000 m dia. x 130 m depth - nominal) and the weight penalty of a satellite to be built and transported to a synchronous orbit, the stiffness of such an antenna cannot be made arbitrarily high. A series of questions may be asked, such as, (1) how stiff the structure will have to be in order to meet the operational requirement?; (2) is the configuration under study stiff enough?; (3) is there any trade off between structural stiffness and active shape control? Before these questions can be addressed, the relationship between the structural deformation and the antenna transmission loss must be established. This is the subject of the next subsection. In this subsection, the local slopes of the antenna radiation surface is derived.

For structures of finite stiffness, surface deformation will occur if disturbances or forces are applied to the structure. Accompanied with the local displacement is the change of the direction of the normal to the local surface, or the local slope. Since the antenna is retrodirective phase conjugate, the transmission efficiency is not sensitive to the variation of path length or the surface dispositions but it is very sensitive to the local slope changes. Therefore, it is important to evaluate the local slope variations.

Since the finite element model being used does not provide the details at the subarray level, one can only compute the slopes of the secondary structure. In fact, the secondary structure is not modelled either; its slopes are computed by assuming that the local surfaces are flat and each one a part of one of the 61 plane surfaces. Referring to Fig. 1, the secondary structure consists of 61 hexagonal substructures referred to here as the hexagonal planes. Each hexagon plane is supported at the three symmetrical vertices by the supporting pins on the primary structure such that there is no direct contact between the primary and the secondary structures and that there is no contact between the secondary

substructures themselves. This is done to reduce the interactions between structural components. It may also be important to point out that the grid points assigned in the model coincide with the supporting pins (actually each grid point represents the three closest pins and is positioned at the geometrical center of the three pins (refer to Figs. 2 and 3)).

With this background in mind, the local slope angles can be readily derived. There are at least two ways for computing the slope angles, (1) using the equation of a plane, and (2) using vector product.

Let $(\bar{x}_1, \bar{y}_1, \bar{z}_1)$, $(\bar{x}_2, \bar{y}_2, \bar{z}_2)$, and $(\bar{x}_3, \bar{y}_3, \bar{z}_3)$ be the coordinates of the three grid points associated with a typical hexagon plane i (the index i and the grid point index j were dropped). In the following the bar in "$\bar{\ }$" that signifies the grid point position with the rigid body motion suppressed is also dropped.

Method 1 - Plane Equation Approach:

Let a, b, and c be the constant coefficients, and the equation of a typical plane may be written as,

$$ax + by + cz = 1 \tag{15}$$

The coefficients may be determined by substituting the three points into (15) and solving the three linear simultaneous equations, or

$$\begin{bmatrix} a \\ b \\ c \end{bmatrix} = \begin{bmatrix} x_1 & y_1 & z_1 \\ x_2 & y_2 & z_2 \\ x_3 & y_3 & z_3 \end{bmatrix}^{-1} \begin{bmatrix} 1 \\ 1 \\ 1 \end{bmatrix} \tag{16}$$

To avoid numerical iterations, compact expressions for the matrix inversion may be used. Since the coordinates of the three points are computed at each step, the values of a, b, and c can be evaluated accordingly and the slope angle error, θ, is readily obtained,

$$\theta = \cos^{-1} \frac{|c|}{\sqrt{a^2 + b^2 + c^2}} \tag{17}$$

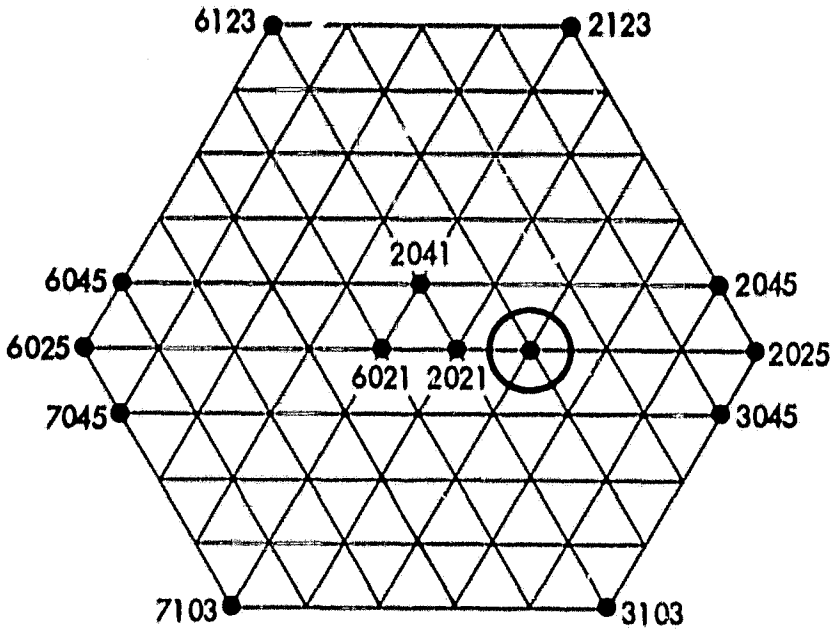

(a) 75 Grid Points on Array Side of Primary Structure (Only 13 with ID shown).

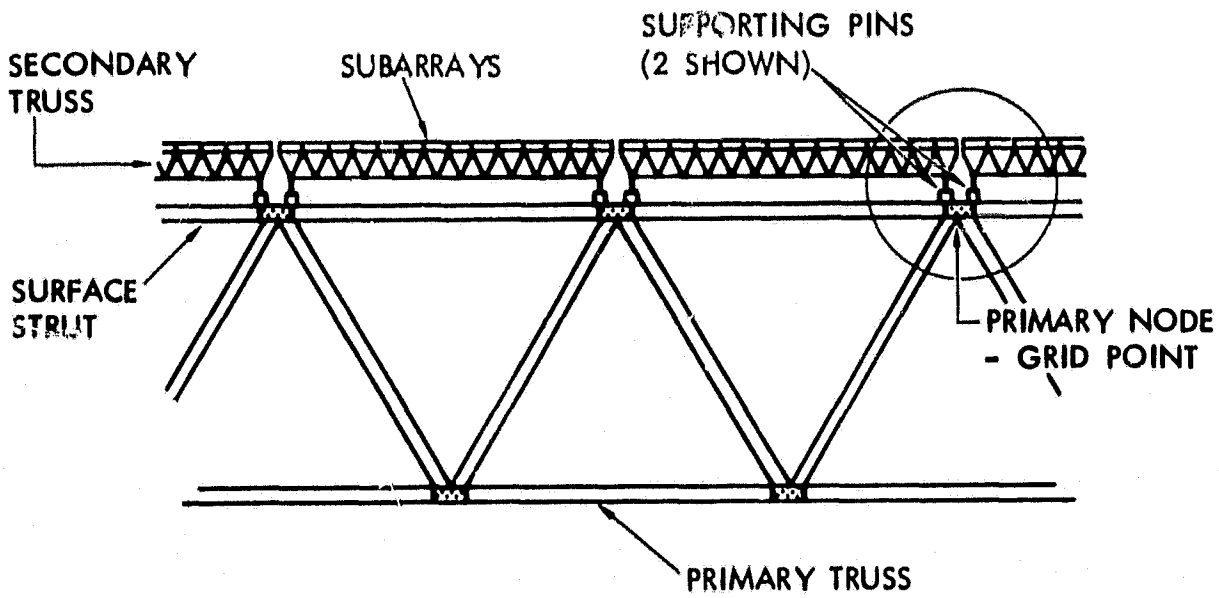

(b) Secondary Structure Supporting Pins.

Figure 2. Grid Points of the Finite Element Model and the Secondary Structure Supporting Pins

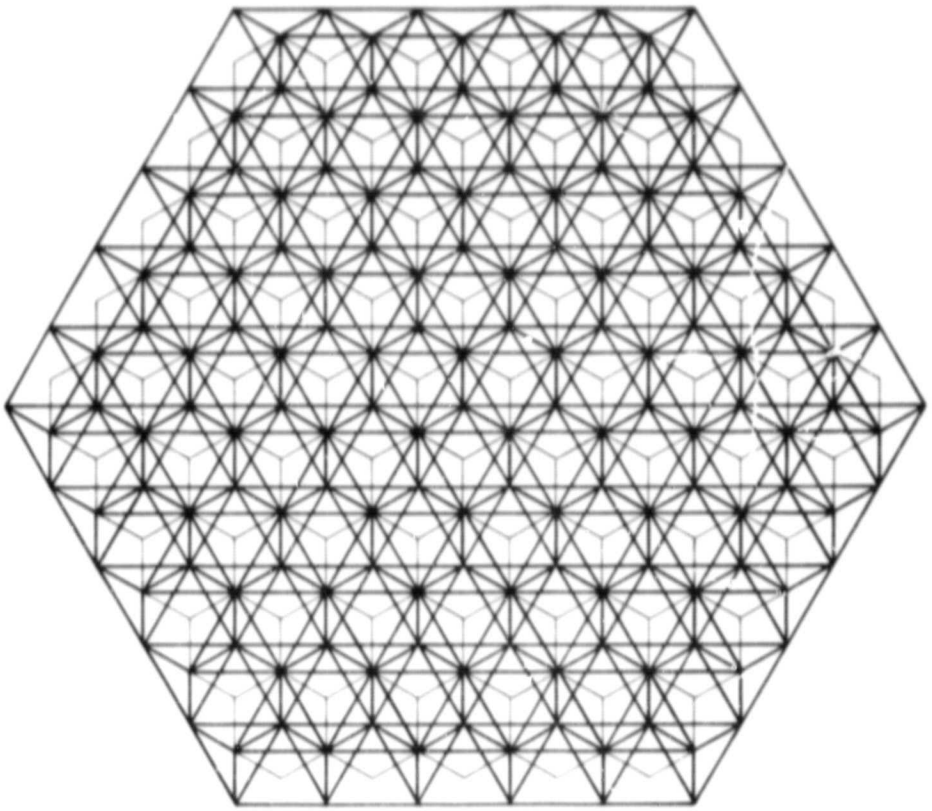

Figure 3. The Grid Points and the 61 Hexagonal Planes

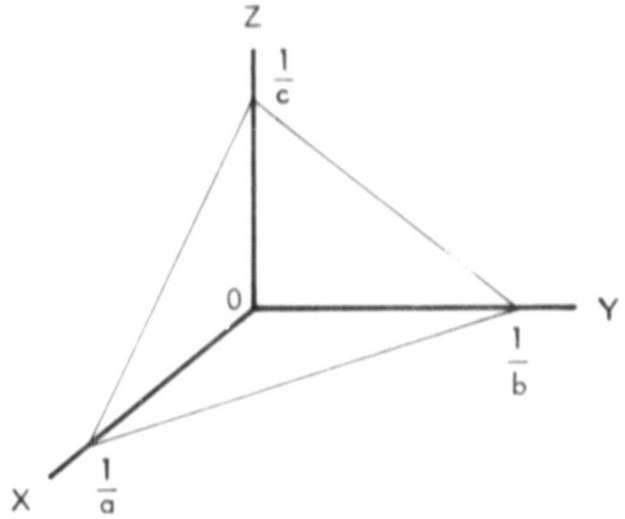

Figure 4. Plane Intercepts

Note that the matrix inverse in (16) does exist, since, in our application the three points are always non-colinear. However, this method could lead to computational difficulties. Referring to Fig. 4, 1/a, 1/b, and 1/c are the three intercepts of the plane on the X-, Y-, and Z-axis, respectively, hence, as the plane becoming parallel to the XY-plane, $a \to 0$, $b \to 0$ and $c \to \infty$. Since θ is a very small angle (and time varying), double precision computation will be required for the evaluation of (17).

Method 2 - Vector Product Approach:

This appraoch is simpler than the first method and it requires fewer computation steps. Let Δ_1 and Δ_2 be defined as follows,

$$\Delta_1 = \begin{bmatrix} x_2 - x_1 \\ y_2 - y_1 \\ z_2 - z_1 \end{bmatrix} \tag{18a}$$

$$\Delta_2 = \begin{bmatrix} x_3 - x_1 \\ y_3 - y_1 \\ z_3 - z_1 \end{bmatrix} \tag{18b}$$

Let their vector product be $(A\ B\ C)^T$, then

$$\begin{bmatrix} A \\ B \\ C \end{bmatrix} = \Delta_1 \times \Delta_2 = \tilde{\Delta}_1 \Delta_2 \tag{19}$$

where

$$\tilde{x} \triangleq \begin{bmatrix} 0 & -x_3 & x_2 \\ x_3 & 0 & -x_1 \\ -x_2 & x_1 & 0 \end{bmatrix}$$

the slope angle is

$$\theta = \cos^{-1} \frac{|c|}{\sqrt{A^2 + B^2 + C^2}} \tag{20}$$

For the same reason discussed in Method 1, double precision computation will also be required in evaluating (20). Method 2 was used in our computation.

The slope angle, $\theta_i(n)$, is a function, and its value varies with time (n) and space (i). The individual values of the slope angle will not mean much for the antenna as a whole. Other performance measurements must be defined. Three measurements are used here.

The Maximum Slope Error

$$\theta_M(n) = \max_{i\in\{1,\ldots,61\}} \theta_i(n) \tag{21}$$

$\theta_M(n)$ is the greatest slope angle of the 61 hexagonal substructures, at time t = nT; therefore, it represents the worst case.

The RMS Spatial Average

$$\theta_{RMS}(n) = \sqrt{\frac{1}{61}\sum_{i=1}^{61}(\theta_i(n))^2} \tag{22}$$

$\theta_{RMS}(n)$ fluctuates with time which is a good measurement of the antenna at a typical time t = nT.

The RMS Time Average

$$\bar{\theta}_{RMS}(n) = \sqrt{\frac{1}{n}\sum_{m=1}^{n}(\theta_{RMS}(m))^2} = \sqrt{\frac{1}{61n}\sum_{m=1}^{n}\sum_{i=1}^{61}(\theta_i(m))^2} \tag{23}$$

$\bar{\theta}_{RMS}(n)$ is a smoother measurement especially when n becomes large. This measurement is useful when one asks how is the antenna doing so far. $\bar{\theta}_{RMS}(n)$ becomes less and less sensitive to the current sample as n increases, which is a common defect of the averages of this kind. This problem may be solved by applying a window to the samples, i.e., one only uses the N most recent samples in the average. Another way to increase the sensitivity is to assign a heavier weight to the most current sample, for instance, assign 10% weight to the most current sample and 90% to the rest as a whole when $n \geq 10$. This latter approach does not require additional storage space.

2.3 THE MICROWAVE TRANSMISSION SYSTEM SCAN LOSSES

Since the design of the MPTS antenna is still in the evolving stage, the data and assumptions made in this section are far from final. Nevertheless, the results of this and the subsequent sections will still be valuable information for the purpose of developing performance requirements.

The MPTS antenna is a phase array antenna which consists of a large number (say, on the order of 10,000) of array elements. Array elements are installed on the 61 secondary substructures. Each element has an aperture area of about 108 m^2, or for a rectangular aperture the aperture size is about 10.39 m.

The array is active retrodirective so that it is made insensitive to the path length variations but it is quite sensitive to angular deviations from the line-of-sight. The latter requires accurate pointing. Pointing will be achieved by two control systems, the mechanical pointing control which is required to stay within a few arc minutes of the target--the rectanna, and the fine pointing control-electronic beam steering which is required to steer the beam to within several arc seconds.

Let D be the aperture, θ be the slope angle (or angular pointing error), and λ be the wavelength of the microwave power. Since the frequency is 2.45 GHz, the corresponding λ is .1224 m. For uniformly illuminated antenna with rectangular aperture, the radiation pattern is

$$\frac{\sin\left(\frac{\pi D}{\lambda}\sin\theta\right)}{\frac{\pi D}{\lambda}\sin\theta} \simeq \frac{\sin\left(\frac{\pi D}{\lambda}\theta\right)}{\frac{\pi D}{\lambda}\theta} \qquad (24)$$

the approximation is valid for small θ. Equation (24) prescribes the patterns for both the array and the elements; for the array, one substitutes $D_a = 1000$ for D and for the elements, use $D_e = 10.39$ for D. From this one can see immediately that the array pattern is much narrower than that of the element. More precisely, the half-power-width (the beam width at the half power points) of the array is about 100 times narrower than that of

the element. At the half-power-point $\pi D\theta/\lambda = 1.3916$ rad and the corresponding θ_a and θ_e are .0031° and .299°, respectively. Figure 5 shows the antenna and element patterns.

In the following it is assumed that the electronic beam steering system points the beam at the rectenna perfectly and the discussion is concentrated on the effects due to surface deformation of the structure, i.e., the effects of scan angle variations on the antenna efficiency.

Scan Loss

The amplitude of the array pattern varies with the scan angle. The field strength decreases rapidly as the scan angle increasingly deviates from the normal of the array surface. The governing relationship is that the array beam amplitude is prescribed by an envelope which is determined by the contributing element patterns. In the case that the scan angles are the same for all the subarray elements, the envelope becomes the element pattern itself. This is illustrated in Fig. 6. The loss of power due to scan is called the scan loss.

Let P_T be the total power, P_i the maximum power of element i, and $\sin x_e/x_e$ the corresponding element pattern, where the argument $x_e = \pi D_e \theta_i/\lambda$, then

$$P_T = \sum_i P_i \left(\frac{\sin x_i}{x_i}\right)^2 \tag{25}$$

a. Rigid array surface

In this case all $x_i = x$ or $\theta_i = 0$,

$$P_T = \left(\frac{\sin x}{x}\right)^2 \sum_i P_i = \left(\frac{\sin x}{x}\right)^2 P_{TM}$$

where P_{TM} is the maximum power of the array. The scan loss P_L and the percent loss are,

$$P_L = P_{TM}\left[1 - \left(\frac{\sin x}{x}\right)^2\right],$$

$$P_L\% = \left[1 - \left(\frac{\sin x}{x}\right)^2\right] \times 100 \tag{26}$$

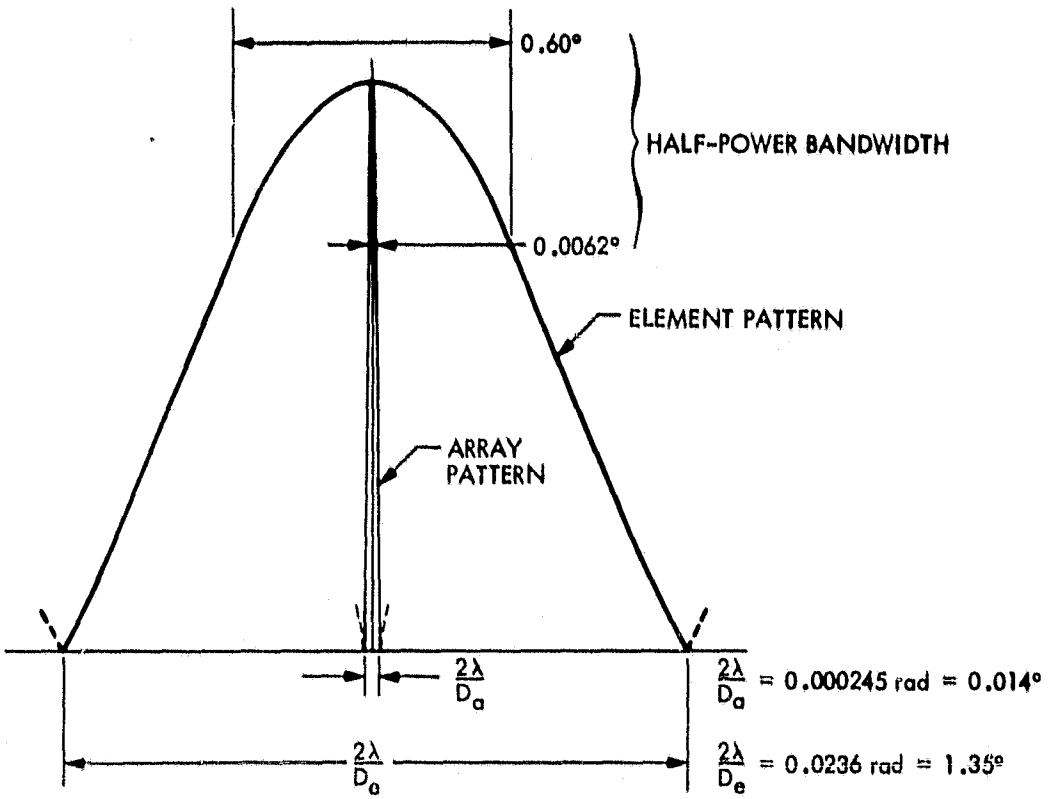

Figure 5. Array Pattern and Element Pattern for Rectangular Aperture Array with Uniform Illumination

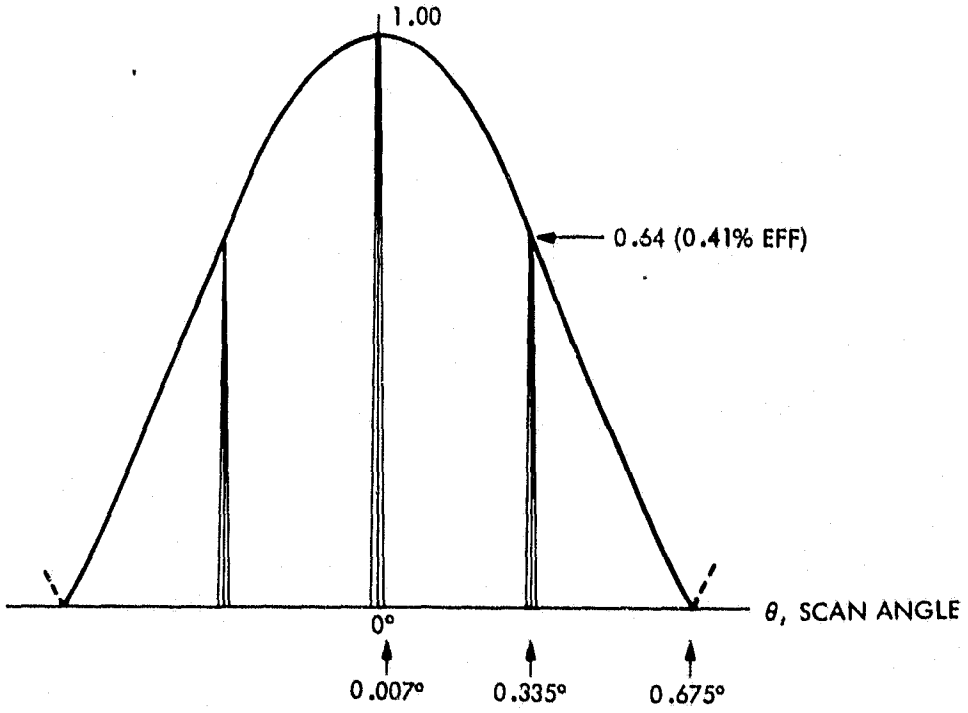

Figure 6. Beam Amplitude vs Scan Angle

The percent scan loss is plotted in Fig. 7 which illustrates how critical the scan angle is to the power output.

b. Uniform illumination

For uniformly illuminated array, $P_i = P$,

$$P_T = P \sum_i \left(\frac{\sin x_i}{x_i}\right)^2 = \left(\frac{P_{Tm}}{N}\right) \sum_{i=1}^{N} \left(\frac{\sin x_i}{x_i}\right)^2$$

where N is the total number of elements and

$$P_L\% = \left[1 - \frac{1}{N} \sum_{k=1}^{N} \left(\frac{\sin x_i}{x_i}\right)^2\right] \times 100 \qquad (27)$$

c. The RMS approximation

Assume that the root-mean-square value of the scan angle, θ_{RMS}, is known, where

$$\theta_{RMS} = \sqrt{\frac{1}{N} \sum_{i=1}^{N} \theta_i^2}$$

The corresponding x_{RMS} can be easily evaluated:

$$x_{RMS} = \sqrt{\frac{1}{N} \sum_{i=1}^{N} \left(\frac{\pi D_e}{\lambda} \theta_i\right)^2} = \left(\frac{\pi D_e}{\lambda}\right) \theta_{RMS} \qquad (28)$$

then

$$P_{TRMS} = \sum_{i=1}^{N} P_i \left[\frac{\sin\left(\frac{\pi D_e}{\lambda} \theta_{RMS}\right)}{\frac{\pi D_e}{\lambda} \theta_{RMS}}\right]^2$$

$$= \left(\frac{\sin\left(\frac{\pi D_e}{\lambda} \theta_{RMS}\right)}{\frac{\pi D_e}{\lambda} \theta_{RMS}}\right)^2 P_{TM} \qquad (29)$$

and the percent scan loss is,

$$P_{LRMS}\% = \left[1 - \left(\frac{\sin\left(\frac{\pi D_e}{\lambda} \theta_{RMS}\right)}{\frac{\pi D_e}{\lambda} \theta_{RMS}}\right)^2\right] \times 100 \qquad (30)$$

Note that in general $P_{TRMS} \neq P_T$ and hence $P_{LRMS} \neq P_L$. However, our simulation shows that for many test cases

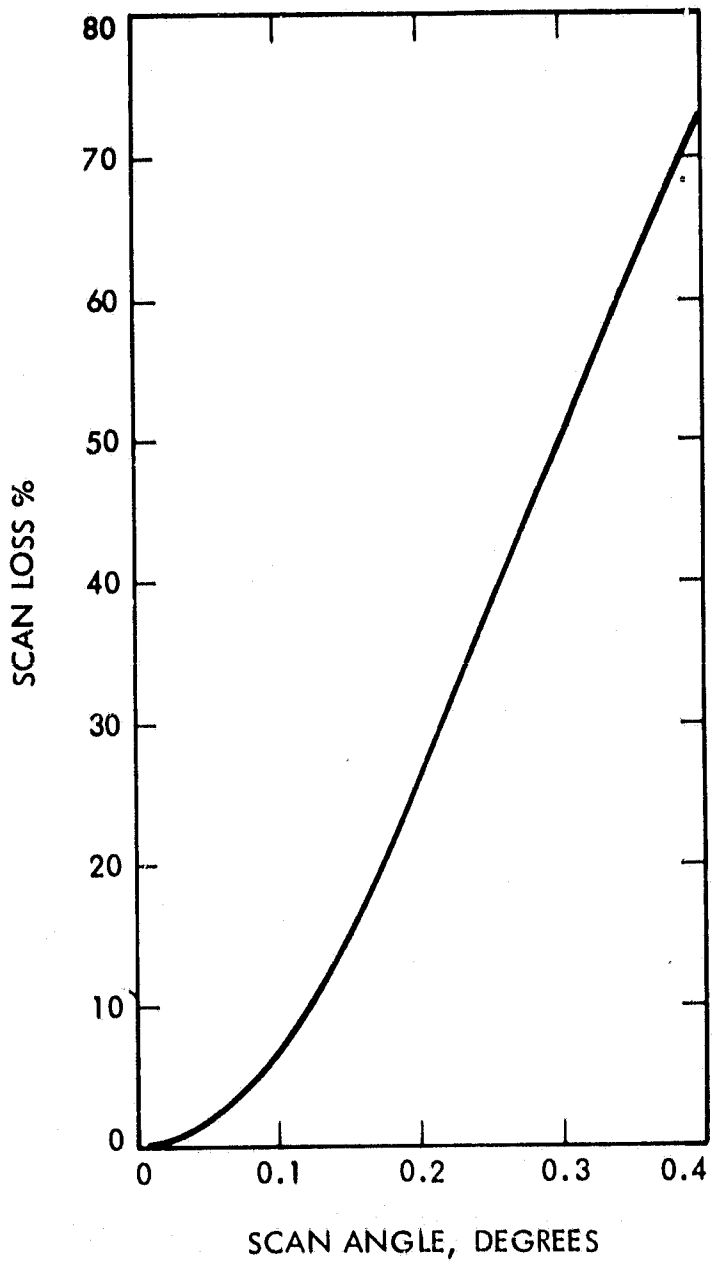

Figure 7. Scan Loss of a Rigid Array

they are quite close. Therefore, P_{LRMS}% may be used instead of P_L%. The former requires much fewer computation steps. Note that the θ_{RMS} here is the RMS spatial average.

d. Gaussian illumination

In order to reduce the side lobs of the array pattern, the elements may be illuminated non-uniformly. One way to accomplish this is to tailor the illumination of the element according to a Gaussian curve. In this case,

$$P = P_o \, e^{-(R/R_o)^2 \alpha} \tag{31}$$

The parameter α may be determined by the taper at the edge of the array. For a 10% taper, i.e., $P/P_o = 0.1$ when $R = R_o$, $\alpha = 2.3$. A 10-step taper that approximates a Gaussian curve was proposed in an earlier study [2].

From (25), P_T becomes,

$$P_T = \sum_i P_o \, e^{-(R_i/R_o)^2 \alpha} \, (\frac{\sin x_i}{x_i})^2 \tag{32}$$

$$= P_o \sum_i (\frac{\sin x_i}{x_i})^2 \, e^{-(\frac{R_i}{R_o})^2 \alpha}$$

where R_i is the diatance from the center of the array to the element, and R_o the radius of the array aperture.

Of the last three cases, only the first two were implemented (refer to Appendix A).

SECTION 3

SURFACE DEFORMATION AND ITS EFFECTS ON THE ANTENNA EFFICIENCY DUE TO DISTURBANCES AND DYNAMIC INTERACTIONS

This section addresses the problem of surface deformation and its effect on the microwave power transmission efficiency in quantitative terms. Specifically, the question of how significantly the disturbances will impact on the antenna's flatness and how much disturbance the antenna can stand without incurring excessive power loss will be answered. The results were obtained through extensive computer simulation.

Before the main results are discussed, the modal characteristics of the antenna and how these affect the overall system modes is briefly described and then the magnitude of disturbance and dynamic interaction forces are estimated which form the basis for the magnitude of simulation input.

3.1 THE MODAL CHARACTERISTICS OF THE ANTENNA AND THEIR EFFECTS ON THE OVERALL STRUCTURE OF SPS

The fundamental properties of a large space structure such as the MPTS antenna that have significant effects on the control system design are the structural vibrational properties which are governed by the fundamental frequencies and the mode shapes. The former affects the controller bandwidth design and the latter affects the sensor/actuator location selections.

The first 20 natural frequencies of the structure are summarized in Table 1. Of the 20 modes, the first 6 are the rigid body or zero frequency modes and the rest are flexible modes. Figure 8 shows the mode shapes of the first 14 flexible modes. The first two modes in Fig. 8 exhibit astigmatism bending, the third one is a defocus mode, and the fourth mode (mode 10) exhibits trefoil bending characteristics. The rest of the flexible modes have either the similar modal characteristics of the first four but with higher frequency patterns or a combination of them.

Table 1. The First 20 Modal Frequencies of the Antenna Structure (Data obtained from Ref. 4).

Mode No.	Frequency, Hz	Remark
1	0	Rigid Body Mode
2	0	"
3	0	"
4	0	"
5	0	"
6	0	"
7	.0189	Flexible Modes
8	.0190	"
9	.0196	"
10	.0343	"
11	.0345	"
12	.0348	"
13	.0430	"
14	.0457	"
15	.0463	"
16	.0471	"
17	.0499	"
18	.0505	"
19	.0515	"
20	.0517	"

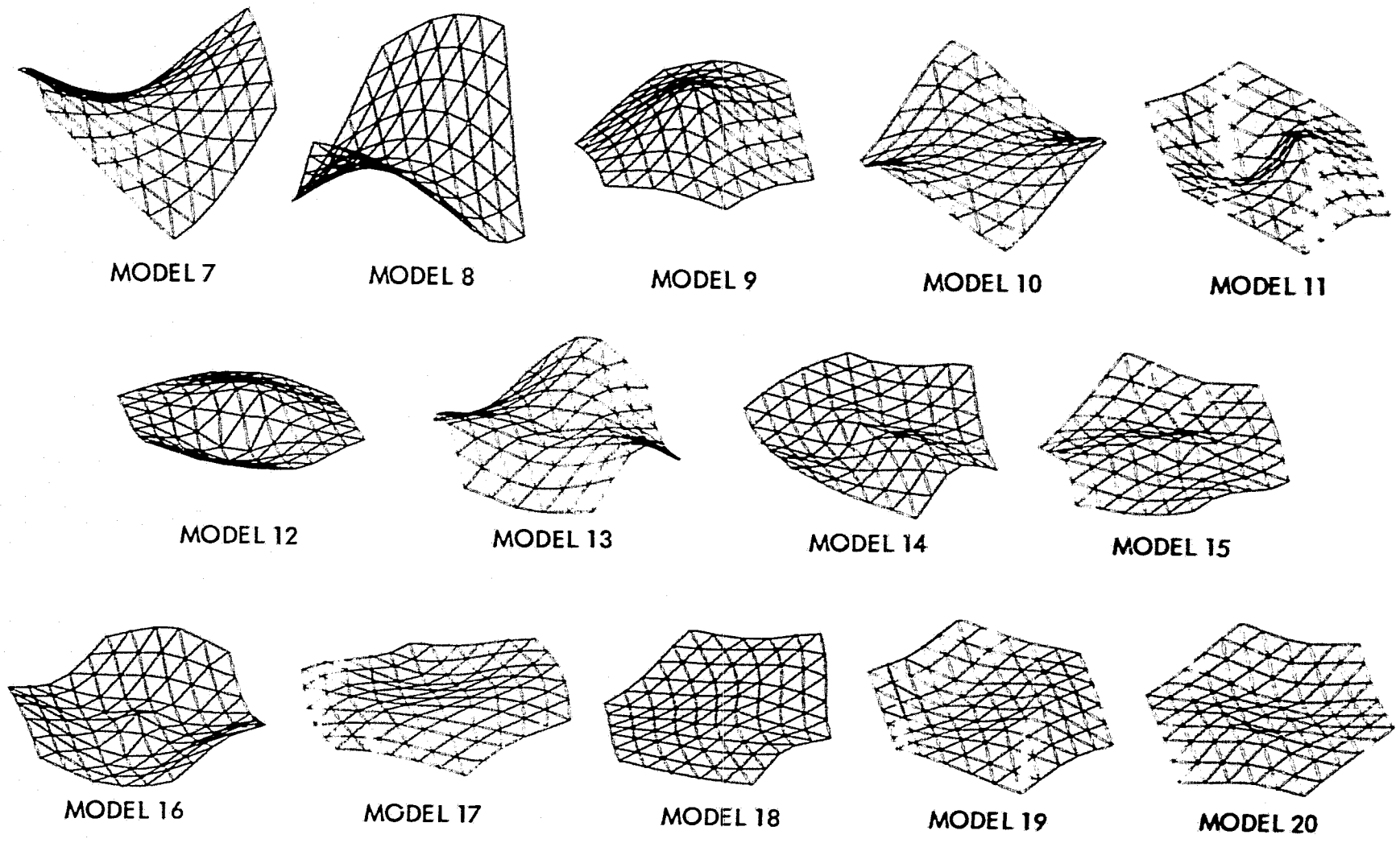

Figure 8. Mode Shapes of the First 14 Flexible Modes of the MPTS Antenna

The mode shapes of the first four flexible modes are in general agreement with that discussed in Ref. 3 where only the first four flexible modes were illustrated. However, the modal frequencies are about 4 to 7 times greater in Ref. 3 than those listed in Table 1. It is also noted that the nominal mass used for the antenna in our model is 15×10^6 kg whereas it was 8.58×10^6 kg in Ref. 3, a factor of 1.75. Since the generalized stiffness is proportional to the mass times frequency squared ($m\omega^2$), the stiffness is about 11 times greater for modes 7, 8, and 10, and greater for mode 9 in Ref. 3 than these in our model.

Figure 9 shows a comparison of the natural frequencies of the MPTS antenna, solar collector, and the first five frequencies of the flexible modes of the SPS. The following conclusions may be drawn.

1. The fundamental frequencies of the SPS and the antenna are 2 to 3 orders of magnitude greater than the orbital frequency. This means that the couplings between the SPS flexible modes and the orbit will not be significant.
2. The fundamental frequency of the antenna is about one order of magnitude greater than that of the collector. However, the frequencies of the first three flexible modes overlap with that of the 8th mode of the collector which indicates possible couplings between these modes. Due to the fact that higher frequency modes are less likely to be excited, the likelihood of their exciting the lower modes of the antenna are also reduced. Nevertheless, caution must be exercised in the controller/actuator design so that mode 8 of the collector will not acquire excessive energy at any time.
3. The antenna does not decrease the SPS frequencies significantly nor does the coupling stiffness [5]. This is because of the superior size and mass of the collector over that of the antenna. The implications of this

observation is that the design alterations of the antenna and the coupling will not significantly impact on the vibrational properties of the overall system.

4. The most significant factors that affect the modal properties are the geometrical properties of the structure for both the antenna and the collector, i.e., the size and the relative size (e.g., aspect ratio) of the dimensions of the structure.

The 3-D plots of the mode shapes was done by the program listed in Appendix B and the required dynamic responses were computed by the program listed in Appendix A.

3.2 ESTIMATES OF DISTURBANCES AND DYNAMIC INTERACTIONS

Disturbances may be categorized as external and onboard. External disturbances include gravity gradient torques, solar pressure, magnetic torques (due to the interaction between the Earth's magnetic field at the synchronous orbit and the onboard current loops), etc. The onboard disturbances include, for instance, the microwave recoil, dynamic unbalance torque, current interaction torque, thruster firing, etc. Qualified as both external and onboard is the thermal bending disturbance due to temperature gradient of the structure. Excluded from either category is the dynamic interaction between the array and the collector such as the forced motion of the antenna due to collector bending.

The effects of some of the disturbances can be reduced by careful design. For instance, the current interaction torque may be reduced by careful arrangement of the conductors so that the conductor pairs are coplanar or by using coaxial cables. Thruster impingement may be reduced by using gimballed pairs and by careful selection of their locations, etc. Solar pressure and microwave recoil forces (and torques) are rather small to cause any flatness problems of the antenna. They may create station keeping problems more than anything else. Therefore, it is sufficient only to look into the effects of gravity gradient torques and the forces due to collector bending.

Gravity Gradient Torques

The gravity gradient torque about the x-axis (refer to Fig. 10) is,

$$\tau_x = -\frac{3}{2}\omega_o^2 (I_z - I_y) \sin 2\left(\frac{\pi}{2} - \theta_x\right)$$

$$= -\frac{3}{2}\omega_o^2 (I_z - I_y) \sin 2\theta_x \qquad (33)$$

where x-, y-, and z-axes are the body axes of the antenna, x and y are the inplane axes and z-axis is normal to the array surface. I_y and I_z are moments of inertia and their values are,

$$I_y = I_x = 7.24 \times 10^{11} \text{ Kg-m}^2$$

$$I_z = 1.45 \times 10^{12} \text{ Kg-m}^2$$

and the orbital rate ω_o is 7.272×10^{-5} rad/sec.

Assuming that the orbit is inclined at 7.5°, the satellite will oscillate of $\pm$ 7.5° about the equatorial plane once a day (refer to Fig. 10). For a rectenna located near the equator, the attitude of the array will have to vary $\pm$ 1.34° about the local vertical once a day. For a rectenna located at 45°N the angular deviation will vary between 6.04° and 7.53° from the local vertical. For an equatorial orbit, the angular deviation will be a fixed bias of 6.83° for the 45°N rectenna. Of all these cases, the maximum deviation angle from the local vertical is 7.53°, the maximum bias angle is 6.83°, and the maximum cyclic angular amplitude is 1.34°, and the corresponding gravity gradient torques are, respectively, from (33), -1496 N-m, -1360 N-m, and -269 N-m. These torques are instabilitizing disturbances, i.e., $\theta_x = 0$ is not a stable equilibrium. In all of these cases, control effort will be required to offset gravity gradient effects in addition to tracking (attitude correction to compensate latitudinal motion due to nonzero inclination and to compensate longitudinal motion due to nonzero eccentricity).

The control problems will be discussed in Volume II. The problem of array flatness is the main concern here. It will be clear

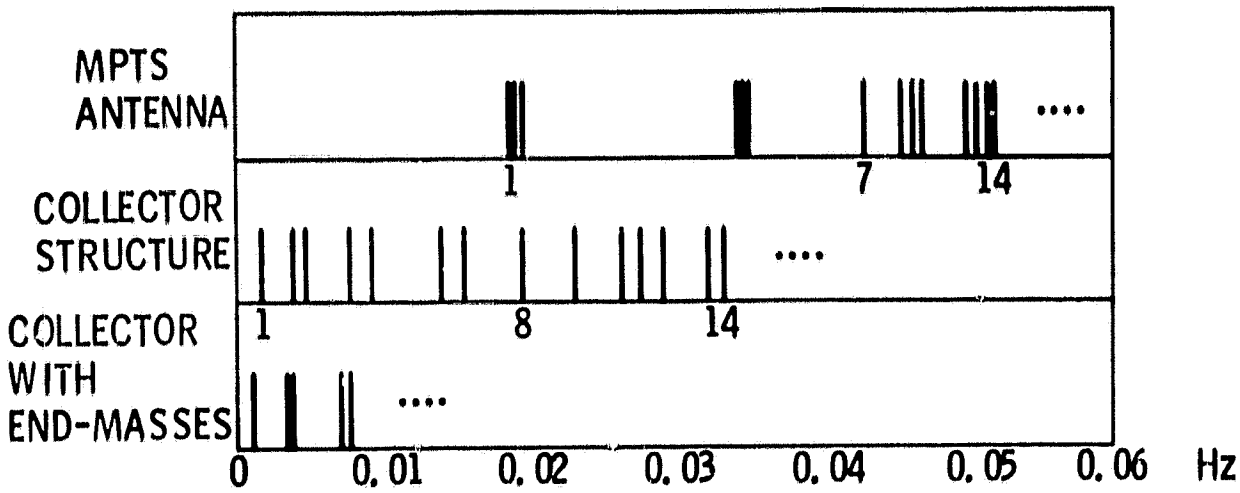

Figure 9, Modal Frequencies of the MPTS and SPS

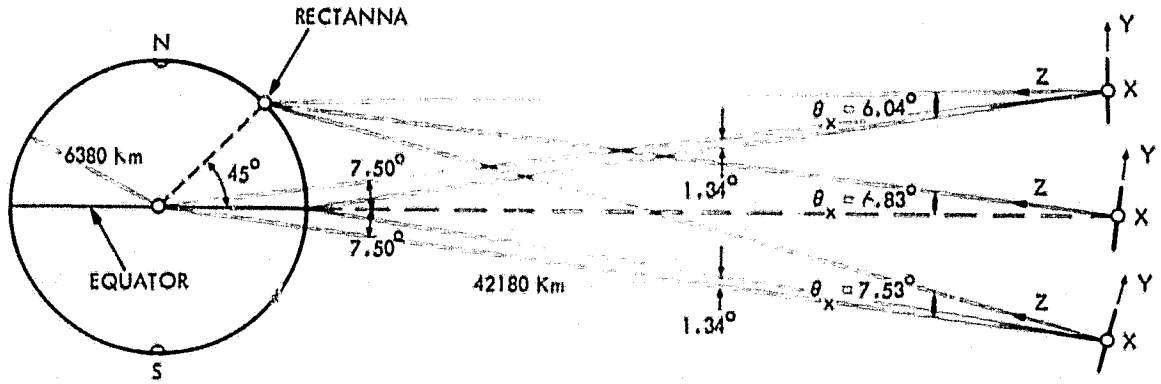

Figure 10. Gravity Gradient at Three Orbit Positions of the MPTS/SPS Oscillating with a 24-hour Period.

later that the warping of the array surface due to gravity gradient is relatively small and insignificant due to the relatively low disturbance level and the low frequency nature of this torque.

Collector Bending Forces

Collector bending motion may be caused by many reasons, for instance, thermal effect, thruster firing for station keeping, maneuvering, attitude acquisition and control, etc. Unless the translational and angular motions of the collector at the interface boundaries are controlled or minimized, they may be the most significant causes of the antenna warping and power loss.

a. Collector bending due to thermal effect

In order to estimate the magnitude of the thermal bending distortion, a collector configuration must be assumed. To be consistent with the work of Johnson Space Center [5] and for the purpose of comparison, the following analysis employs a full configuration identified as 20D4 in Ref. 5. Let ℓ and d be the length and depth of the collector structure, respectively, and their values are, ℓ = 20,000 m, d = 400 m. Assume that the temperature is uniform on each section parallel to the collector surface and the temperature gradient is uniform along the depth. Let ΔT be the temperature difference between the front (solar blanket side) and the back surfaces of the structure. Let α be the coefficient of thermal expansion and ℓ' be the displacement of the antenna interface from the boundary of the collector structure. Under these simplified conditions, the bending displacement, H, is, referring to Fig. 11,

$$H = \frac{d}{\alpha\Delta T}\left(1 + \frac{\alpha\Delta T}{2}\right)\left[1 - \cos\left(\frac{\ell\alpha\Delta T}{2d}\right)\right] + \ell' \sin\left(\frac{\ell\alpha\Delta T}{2d}\right) \qquad (34)$$

The displacement with respect to the center of mass, H_c, is

$$H_c = .444\ H \qquad (35)$$

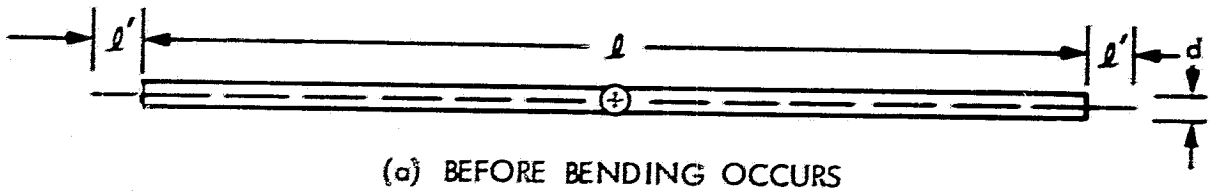

(a) BEFORE BENDING OCCURS

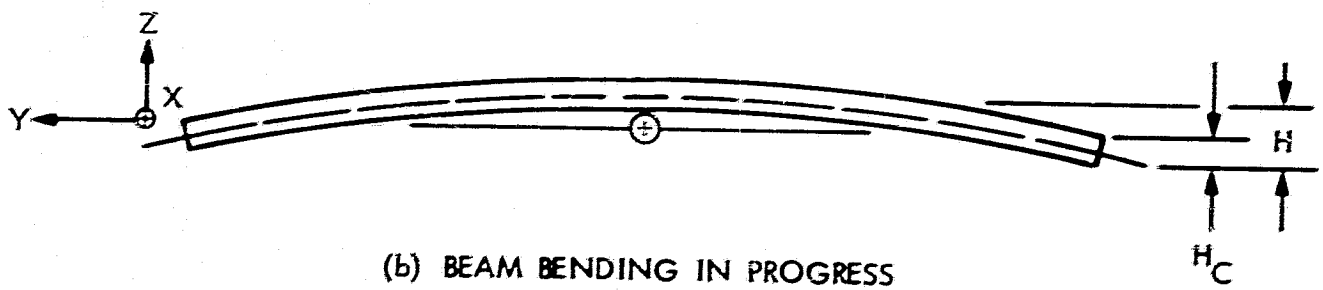

(b) BEAM BENDING IN PROGRESS

Figure 11. Collector Bending due to Thermal Expansion

For a temperature difference $\Delta T = 100°C$, the corresponding values of H and H_c for three values of α are shown in Table 2.

The coefficient of 10^{-5} m/m/°C is in the lower range of metal. For instance, pure aluminum has a thermal expansion coefficient of 2.36×10^{-6}/°C at the temperature range of 293 K to 393 K and slightly less for aluminum wrought alloys. The values of 10^{-6} and 10^{-7} are in the range of graphite composite material.

The thermal disturbance on the solar collector is the worst at the vernal equinox and the autumnal equinox where the SPS will stay in the full shadow the longest period of time. The thermal transient occurs when the collector moves into the shadow and again when it moves into the sun light from the shadow. Since the transit time during the penumbra is about 1.63 seconds, which is about 1/570 of the period of the first bending mode of the SPS structure, the effect due to the penumbra is ignored. For a similar argument, the thermal lag time is also ignored since the lag time is rather small due to the sparsely distributed structural mass. As a result of these idealized assumptions, one may construct this scenario. The tips of the structure are bent away from the sun while the structure is heated by the full sun, and the equilibrium condition is reached. Suddenly the collector enters the shadow and the temperature gradient is reduced to an insignificant value, and the distorted structure is released from its retension force and starts to bounce back. This causes an oscillatory motion at the tips about the new equilibrium state. This motion applies a sinusoidal cosine translational acceleration or forces at the antenna interface.

Table 2. Bending Displacement

α, m/m/°C	H, m	H_c, m
10^{-5}	150.0	66.66
10^{-6}	15.0	6.67
10^{-7}	1.5	.67

Table 3. Thermal Disturbance Estimates

α, m/m/°C	Z_m, m	A_m, m/s^2	A_m, g	F_m, N
10^{-5}	66.66	3.037×10^{-3}	$.31 \times 10^{-3}$	45558
10^{-6}	6.67	3.039×10^{-4}	$.31 \times 10^{-4}$	4558.5
10^{-7}	0.67	3.039×10^{-5}	$.31 \times 10^{-5}$	455.9

The above scenario is drawn to help in the determination of the proper forcing function. The real interest here is not in the period when the SPS is in the occultation, but is in the period after the occultation. With the above discussion, one can construct a similar but reversed scenario; that is, the structure starts a bending motion after it enters full sunlight. The only difference is that this time the equilibrium surface is a bent surface whereas in the shadow it is a plane.

Let Z be the displacement of the antenna interface, then

$$Z = -Z_m \cos \omega_s t \tag{36}$$

and

$$\ddot{Z} = \omega_s^2 Z_m \cos \omega_s t \tag{37}$$
$$= A_m \cos \omega_s t$$

and the equivalent force applied at the antenna interface will be,

$$F = m_a \omega_s^2 Z_m \cos \omega_s t \tag{38}$$

where $Z_m = H_c$, $\omega_s = 2\pi$, and $f_s = .00675$ rad/sec and is the first bending frequency of the SPS. $m_a = 15 \times 10^6$ kg is the nominal mass of the antenna. Table 3 shows the values of Z_m, A_m, and F_m for the three values of α.

The effects of the thermal disturbance on the antenna's surface deformation are examined in the next subsection.

b. Collector bending due to other disturbances

The collector structure bending caused by disturbances other than thermal effect may be significant. Since an accurate estimate requires the details of specific designs, therefore, instead of being specific about the disturbances, a more generic approach is taken here. Since it is not inconceivable to anticipate a Z_m of 1/2000 of the length of the collector structure, forces corresponding to a

range about this Z_m were considered in the simulation. Both sinusoidal and step functions were applied.

Torsional Motion of the Collector at the Interface

The first torsional mode (see Fig. 12) of the SPS is the third flexible mode which has a natural frequency of .00359 Hz or .0226 rad/sec [5]. For a 1° torsional oscillation at the collector's tip, the corresponding torque applied at the antenna interface will be,

$$\tau_m = I\,\omega^2\,\theta_m = 6.4528 \times 10^6 \text{ N-m}$$

The corresponding force exerted at the antenna interface will be $F_m = 6452.8$N. Sinusoidal and step forcing functions were used in the simulation. Note that a 1° torsional oscillation at the tip of the collector corresponds to a translational oscillation of 43.6 m at the extreme boundary (point a in Fig. 12) and 8.7 m at the antenna interface, which is intolerable during the normal operation of the antenna although it may occur during maneuvering operation.

3.3 SIMULATION, RESULTS, AND DISCUSSION

3.3.1 Types of Forcing Functions

The performance of the array structure was tested (via computer simulation) for a number of signal types that approximate the disturbances or maneuvers it may encounter during operation.

The forces and torques applied are step functions, rectangular pulses, and sinusoidal functions. The first two kinds are for maneuvers and the sinusoidal forces are for simulating dynamic interactions induced by collector boundary oscillations. In this later case, both sine and cosine functions were applied; the former represents a gradually applied cyclic acceleration whereas the latter, a cyclic shock load.

In all the cases, the forces were applied at six positions on the primary structure as shown in Fig. 13. At each of the grid points

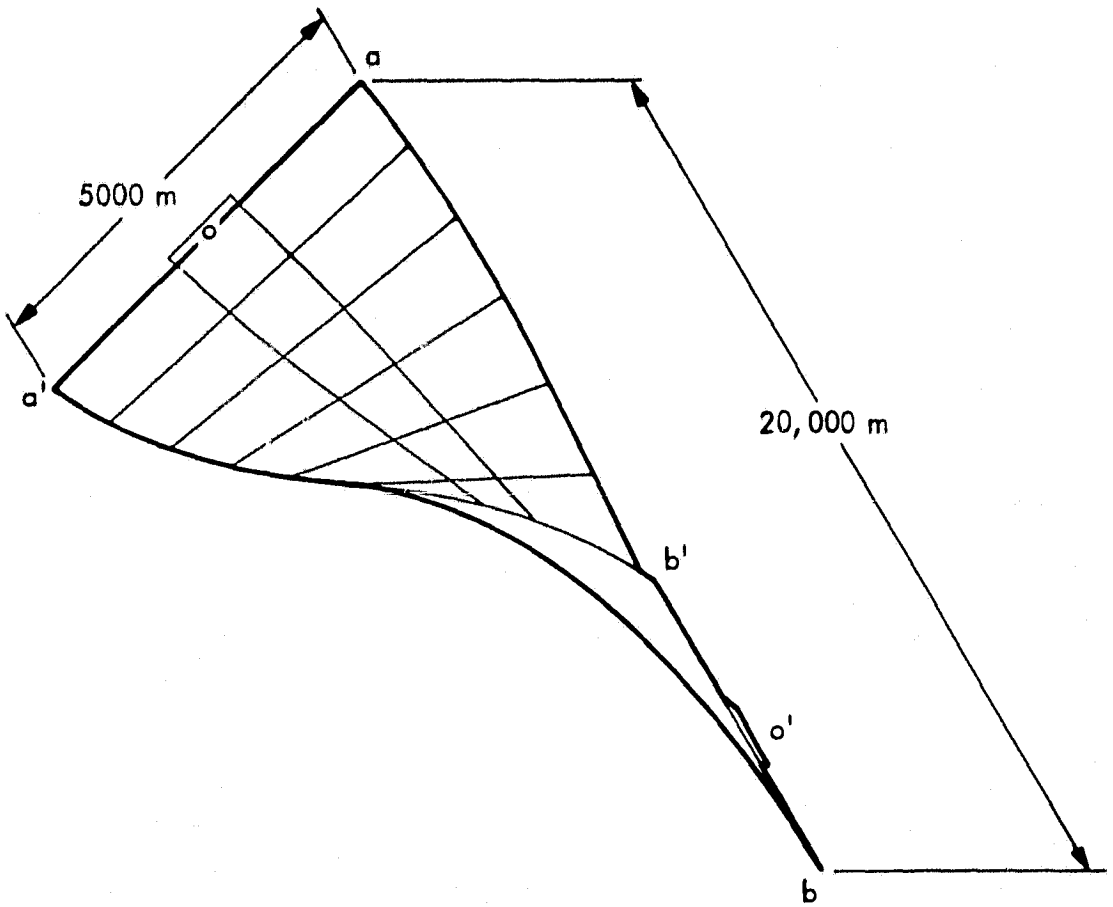

Figure 12. The First Torsional Mode of the Collector

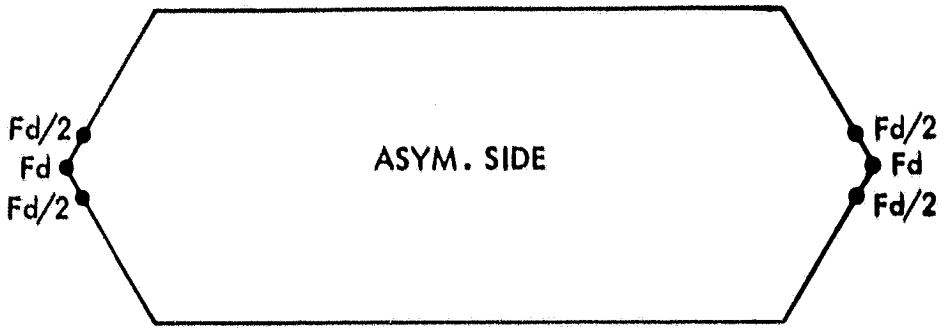

(a) FORCE

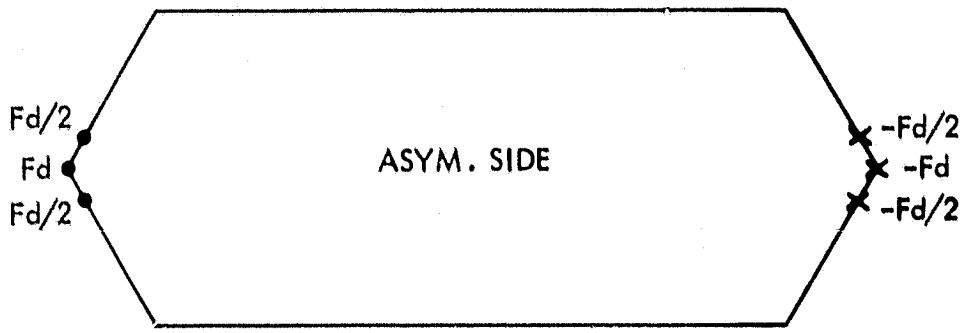

(b) MOMENT

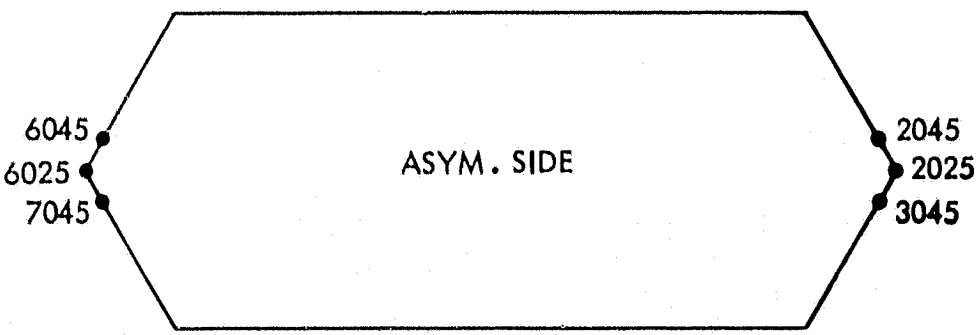

(c) GRID POINTS

Figure 13. Positions of the Applied Forces

6025 and 2025 the force F_d was applied and at each of 6045, 7045, 2045 and 3045 the force $F_d/2$ was applied. Although the 6-point distributed case is more realistically representative of the antenna and collector interface, the results show no significant difference from 2 points (6025 and 2025). Torques were simulated as couples. All the forces considered are normal to the antenna surface; therefore, the results represent the worst case. Note that the antenna/collector interaction will have the greatest effect on the antenna surface when the normal of the two surfaces are in parallel.

3.3.2 Simulation Time Considerations

In most of the cases the simulation time of 1000 seconds was used. This time covers at least one complete cycle of the lowest bending mode of the system (the longest modal period is 930.8 sec.). For the torsional acceleration, 600 seconds were simulated which covers more than two complete cycles of the excitation torque (the first torsional period is 278 sec.)

The computation step sizes of 2.5 seconds and 5 seconds were used which represent about 1/20 and 1/10 of the dominant bending modal period, respectively, and about 1/12 and 1/6 of the dominant torsional modal period (refer to Table 1). Step sizes greater than 5 seconds will be undesirable due to the increased modulation effect on the output. The improvement of 2.5 seconds over 5 seconds has not been significant. Note that the solution algorithm can tolerate much greater step sizes than the numerical integration algorithm. For step functions, exact solutions will be obtained regardless of the step size used.

3.3.3 The Simulation Outputs

The outputs of a simulation run are plotted as time histories of all the interested quantities. The plot consists of the modal amplitude of all the flexible modes, the kinetic and potential energy of the individual flexible modes, the sum of the flexible modes, the rigid body, and

the sum of all the modes; (the energy plots are particularly useful for identifying dominant modes); the maximum out of plane displacement; the three kinds of local slope angles, i.e., the root-mean-square spatial average (RMSL), the root-mean-square running average (RMST), and the maximum slope (SLOP). The antenna scan losses due to slope deviations from the line-of-sight were computed and plotted in two ways, the first, labeled as SLOSS, the scan loss of each of the 61 surfaces computed individually, and their effect summed; the second, SLRMS, computed by using the RMS average of the entire array. Although these are distinct terms, their values are practically the same.

In addition to the information plotted, in the output listings the surface of the maximum slope and the grid point of maximum displacement are listed at each time step.

3.3.4 The Surface Deformation and the Scan Loss

A. Surface Flatness Subject to Collector Bending Oscillation

The effects of collector oscillation of an amplitude of 1/2000 of its length, or 10 m, are discussed here. From Eq. (38), with Z_m = 10 m, m_a = 15 x 10^6 kg, ω_s = .00675 rad/sec, the amplitude of the acceleration force, F_m will be 6832.8 N, or the forced acceleration is .0465 x 10^{-3} g. Figure 14 shows the responses of the structure. By examining the modal energy (Fig. 14 (e)-(h)), it is quite clear that the first three flexible modes (7,8,9) are dominating. The oscillatory property of Fig. 14(a)-(d) shows basically the vibrations of the dominant modes whose frequencies range from .0189 to .0196 Hz.

The surface deformation under this disturbance has exceeded the allowed limit as the RMS spatial average slope angle has exceeded 0.09° (or 5.4 arc. min.) shortly after the force has been applied and it still reached about .07° after 930 seconds as shown in Fig. 14(a). Figure 14(b) shows that the corresponding scan losses of 5.76% and 3.52% respectively. Based on the DOE document [2, p. 27], the antenna/subarray

mechanical alignment of ± 3 arc minutes was specified; and in Ref. 3, pp. xiv and 1.3 the mechanical pointing and slope accuracy of 2 arc minutes and 3 arc minutes (during all phases of operation) were stated, respectively. The scan loss corresponding to a slope error of 3 arc minutes (or .05°) is 1.79%. Hence the 10 m oscillation is too severe for the antenna structure.

From Fig. 14(a), the maximum local slope is much greater than the RMS average; for instance, it is greater than .13° at t = 10 sec. The maximum out-of-plane displacement is about ± 1 m as shown in Fig. 14(c).

It is interesting to note that the energy (envelope) of the flexible modes leads the energy of the rigid body modes by 1/4 cycle of the excitation period as indicated in Fig. 14(d).

For the purpose of comparison; two other forcing functions of the same amplitude were applied at the antenna interface. These functions are 6832.8 sin (.00675 t) and 6832.8U(t).

The responses of cosine and sine excitations are drastically different. Figure 15 shows that the latter is extremely smooth compared with the former. This is also clear from the energy plot, Fig. 15(d), where the flexible modes contribute very little to the system energy. In contrast, Fig. 14(d) shows a much higher proportion. Again, the dominant modes are 7, 8, and 9. Figure 15(c) shows that the out-of-plane displacement has reduced to about half as much and, from Fig. 15(a) and (b), the local slopes and the scan loss are both staying within the requirement.

A step function of the same magnitude, has excited the flexible modes in much the same manner as the cosine function has excited them. By comparing Fig. 14(b) and Fig. 16(b), for instance, the two responses share approximately the same envelope which is slowly decaying with the time constant of the dominant modes, i.e., approximately 1675 seconds.

The results of these three cases are summarized in Table 4.

It is important to point out that in the contest of controlled motion, signal shaping is extremely important and so is the thrust cut-off time (refer to Section 3.3.4D).

B. Surface Response to Collector Bending Disturbance due to Thermal Distortion

In A, the main purposes are to explore the effects of signal types on the flatness of the antenna surface. Here, two more cases are discussed relative to the orbital thermal effect. It is discussed in Section 3.2 that the temperature gradient in the collector can build up almost immediately after the SPS moves out from a full shadow and it is estimated that for the material with the coefficient of thermal expansion (α) of 10^{-6} m/m/°C and a temperature gradient of 100°C front-to-back, the collector bending can reach the amplitude of 6.67 m. With the first collector bending mode dominant, the corresponding force will be

$$F = 4558.5 \cos (.00675\ t) \quad N$$

and the corresponding acceleration will have an amplitude of $.031 \times 10^{-3}$ g.

The simulated results indicate that this disturbance will cause more local surface warping than specified. From Fig. 17(a)-(d) the maximum RMS slope exceeds 0.06° and the scan loss is about 2.7%. Therefore, an α of 10^{-6} m/m/°C with 100°C gradient is not acceptable. However, an excitation force of

$$F = 3417.2 \cos (.00675\ t)$$

corresponding to Z_m = 5 m (or 1/4000 of the length of the collector structure) will be within the requirement as indicated in Fig. 18(a)-(d), where the RMS slope error is about .046° and the maximum scan loss is 1.45%. The maximum out-of-plan displacement is 0.5 m. From eq. (34) and eq. (35), the corresponding α for ΔT = 100°C is $.75 \times 10^{-6}$ m/m/°C.

Table 4. Comparative Performance Analysis, Z_m = 10 m.

Applied Force N	6832.8 cos(.00675t)	6832.8 sin(.00675t)	6832.8 U(t)
Acc. Amp., g	$.0465 \times 10^{-3}$	$.0465 \times 10^{-3}$	$.0465 \times 10^{-3}$
Sim. Period, sec.	1000	1000	1000
Dominant Modes	Modes 7,8,9	Modes 7,8,9	Modes 7,8,9
Local Slope (RMSL max)	.091°	.049°	.0905°
Scan Loss (SLOSS) %	5.76	1.73	5.72
Slope at t = 930 sec	.069°	-	.0705°
Scan Loss at t = 930 sec	3.52%	-	3.36%
Displacement $W_{z\ max}$, m	1.01	.56	1.02

Table 5. Analysis of Performance: Distortions Caused by Thermal Disturbance, $\alpha = 10^{-6}$ and $.75 \times 10^{-6}$ m/m/°C

Coefficient of Thermal Expansion m/m/°C	10^{-6}	$.75 \times 10^{-6}$
Front-to-Back Temp. Grad., °C	100°C	100°C
Thermal Bending Amplitude, Z_m	6.67	5.00
Acc. Amplitude, g	$.031 \times 10^{-3}$	$.023 \times 10^{-3}$
Acc. Force, N	4558.5 cos(.00675t)	3417.2 cos(.00675t)
Local Slope (RMSL max)	.06	.046°
Scan Loss (SLOSS max), %	2.7	1.45
Max. Displacement ($W_z$max), m	.7	.5

Therefore a value of α less than $.75 \times 10^{-6}$/°C will be acceptable provided that the temperature gradient will not exceed 100°C. It seems that an α of 10^{-7} m/m/°C will provide a good safety margin. These results are summarized in Table 5.

C. Surface Deformation Subject to Collector Torsional Oscillation

Torsional vibration at the collector boundary can produce large torque at the antenna interface if the amplitude is high. In section 3.2 it is estimated that, for 1° oscillation, the torque introduced to the antenna will be

$$\tau = 6.453 \times 10^{6} \cos(.0226t)$$

with a corresponding couple at 1000 m apart of

$$F = 6.453 \times 10^{3} \cos(.0226t).$$

Figure 19 shows that the resulting surface distortions are within the requirement. The maximum RMS slope is .05° and the scan loss is about 1.8%.

The dominant modes in this case are modes 10, 12, and 20 as indicated in Fig. 19.

For the purpose of comparison, another simulation was made with

$$\tau = 8.397 \times 10^{6} \sin(.0226t)$$

or the corresponding couple at 1000 m apart,

$$F = 8.397 \times 10^{3} \sin(.0226t)$$

which is equivalent to an oscillation amplitude of 1.3°. A much smoother response was obtained as shown in Fig. 20(a)-(d). The results are summarized in Table 6. These results again point out the importance of signal shaping.

Table 6. Analysis of Performance: Surface Deformation Caused by Collector Torsional Vibration

Collector Vibration Amp. at Boundary	1°	1.3°
Angular Acc. rad/sec/sec	$.51 \times 10^{-3}\cos(.0226t)$	$.66 \times 10^{-3}\sin(.0226t)$
Acc. Torque on Antenna, N-m	$6.453 \times 10^{6}\cos(.0226t)$	$8.397 \times 10^{6}\sin(.0226t)$
Force Couple at Interface, N	$6.453 \times 10^{3}\cos(.0226t)$	$8.397 \times 10^{3}\sin(.0226t)$
Local Slope (RMSL max)	.05°	.042°
Scan Loss (SLOSS max), %	1.8	1.2
Max Displacement ($W_z$max), m	.7	.44

Table 7. Comparative Performance Analysis of Antenna under Rectangular-Pulse-Forced Acceleration

Forcing Function	F = 4000[U(t)-U(t-500)]	$\tau = 2\times10^{6}$[U(t)-U(t-500)]
Distributed Force F_d,N	1000	1000
Local Slope RMSL max	.053°	.017°
Scan Loss SLOSS max, %	2.05	.21
Max Displacement $W_z$max, m	.6	.175

D. Comparative Performance Analysis of Antenna Under Rectangular-Pulse-Forced Acceleration

Two cases were simulated, in the first case a rectangular pulse force

$$F = 4000\ [U(t) - U(t-500)]$$

was applied at the antenna interface and in the second case a rectangular torque

$$\tau = 2 \times 10^6\ [U(t) - U(t-500)]$$

was applied to the antenna.

The objectives of this experiment are to make the following two points:

a. The antenna has greater rotational stiffness than translational stiffness. This observation may be verified by comparing the two cases as plotted in Fig. 21 and Fig. 22. The force of 4000 N was distributed over 6 points (refer to Fig. 13a) and the same force was used to produce the torque of 2×10^6 N-m by reversing one of the two 3-point sets of distributed force (refer to Fig. 13(b)). Note that the force F_d in Fig. 13 is .25 F. The translational acceleration has caused a RMS slope error of .053° and .6 m maximum displacement whereas the rotational acceleration has caused only an .017° maximum RMS slope error and .175 m maximum displacement. Table 7 shows the comparative results.

b. The cut-off time of the pulse is important. For instance, in the case of the translational acceleration, if the pulse were cut off at about 26 seconds sooner (or later), the antenna surface would have been flat after the cutoff. This is quite clear from Fig. 21(e) and (d), since at those times the flexible mode energy was at the minimum.

3.3.5 Further Discussion

In Section 3.3.4 the analysis is based on simulation results. However, no numerical information is by itself complete. In this section, we shall complement the numerical results with further analysis.

Let q be the modal amplitude of a dominant mode, and the corresponding differential equation with the excitation of cosine function may be written in the following form,

$$\ddot{q} + 2\zeta\omega\dot{q} + \omega^2 q = h \cos \omega_o t \qquad (39)$$

the solution of this equation with zero initial conditions is,

$$q(t) = \frac{(\omega^2-\omega_o^2)h\, e^{-\zeta\omega t}}{(\omega^2-\omega_o^2)+(2\zeta\omega\ \omega_o)^2}\left(-\cos\omega\sqrt{1-\zeta^2}t - \frac{\zeta(\omega^2+\omega_o^2)}{(\omega^2-\omega_o^2)\sqrt{1-\zeta^2}}\sin\omega\sqrt{1-\zeta^2}t\right)$$

$$+ \frac{(\omega^2-\omega_o^2)h}{(\omega^2-\omega_o^2)^2+(2\zeta\omega\ \omega_o)^2}\left(\cos\omega_o t + \frac{2\zeta\omega\ \omega_o}{\omega^2-\omega_o^2}\sin\omega_o t\right) \qquad (40)$$

In the context of this application, ζ is in the neighborhood of .005 and $\omega_o^2 \ll \omega^2$, (40) may be approximated by the following simplified equation

$$q(t) \tilde{=} \frac{h}{\omega^2-\omega_o^2}\left\{\cos\omega_o t - e^{-\zeta\omega t}\cos\omega t\right\} \qquad (41)$$

The first term inside the braces represents the steady state solution and the second term contributes only to the transient response.

The maximum value of y(t) is $1.983h/(\omega^2-\omega_o^2)$ which occurs at t = 26.36 sec. The transient to the steady state envelope ratio is about 2 to 1.

Since the modes are decoupled in our model, (41) may be extended to all the flexible modes; hence for mode k, k = 7, ..., 20,

$$y_k(t) \tilde{=} \frac{h_k}{\omega_k^2-\omega_o^2}\left\{\cos\omega_o t - e^{-\zeta\omega_k t}\cos\omega_k t\right\} \qquad (42)$$

From (42), we have the following observations:

1. The modal response is proportional to the constant h_k. Since h_k is the product of the inverse of the kth element of the generalized mass, the mode shape at the point where the force is applied, and the amplitude of the applied force, the modal response is proportional to these parameters.

2. For $\omega_k^2 >> \omega_o^2$, which is the case in this application, the modal response is inversely porportional to the square of the natural frequency.

3. Since the surface deformation at a given point is the sum of the products of the local mode shape and the corresponding modal response, the above properties apply directly to the surface deformation.

4. Owing to the fact that in this application the local slopes are so small that the slope angles are proportional to the local deformations:

   a. For a known system response to a specific disturbance level, the responses to other levels may be obtained by linearly extending the known results.
   b. For known responses to various types of excitations, new results may be obtained by taking the linear combination of the known results.

   By application of these linear system properties, repeated experiments may be avoided and hence a great deal of time and effort may be saved. Figures 23, 24, and 25 show the performance characteristics of the antenna over wide parameter ranges. These figures were obtained by applying the above linear properties.

Table 8. Key to Variable Names for Figures 14 to 22

EFLEX	The sum of energy for the first 14 flexible modes, Joules.
EL7-EL20	The modal energy for modes 7 to 20, Joules.
ERIGID	The sum of energy for the 6 rigid body modes, Joules.
ESUM	The sum of the flexible and the rigid body modal energy, Joules.
RMSL	The root-mean-square spatial average of local slope angles, degrees.
RMST	The root-mean-square time average of local slope angles, degrees.
SLOP	The maximum local slope angle at time T, degrees.
SLRMS	The RMS scan loss (computed from RMSL), percent.
SLOSS	The scan loss of the array, percent.
T	Simulated time, seconds
WZMAX	Maximum out-of-plane displacement of the array at time T, meters.
YL7-YL20	The modal amplitude for modes 7 to 20.

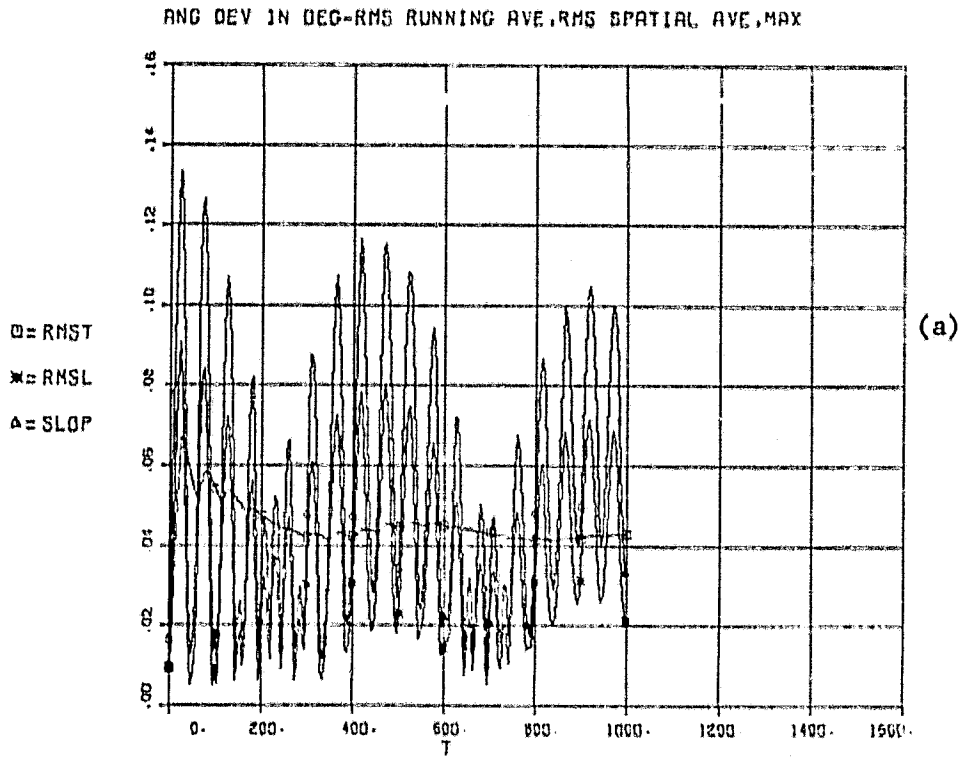

(a)

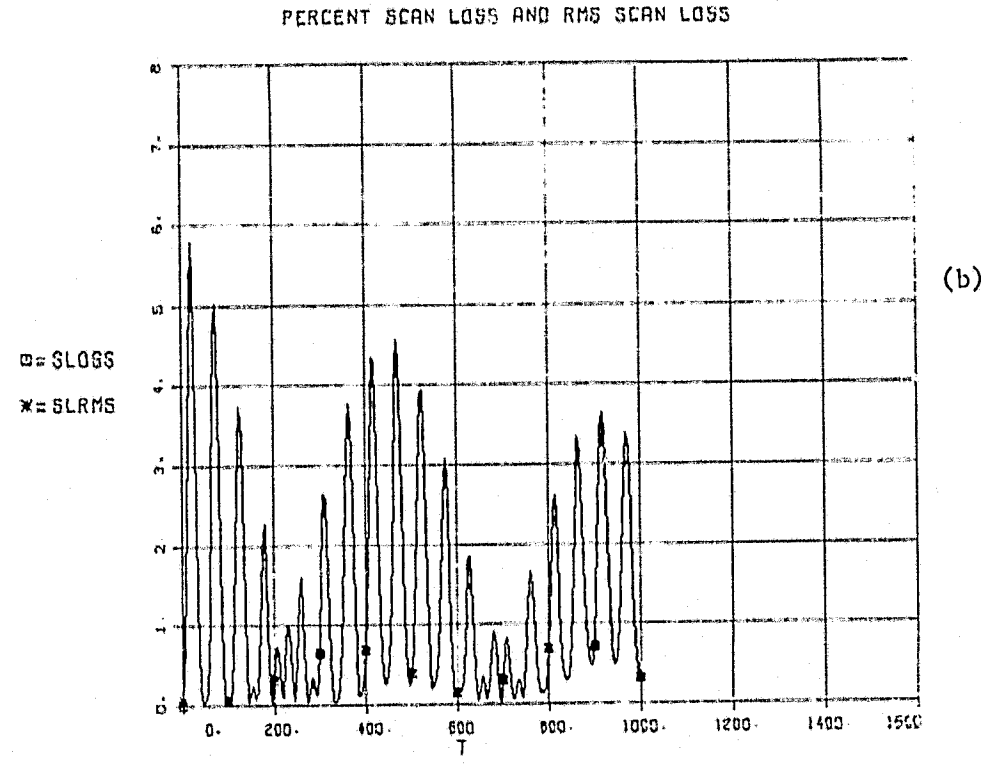

(b)

Figure 14. Surface Response to Collector Bending Oscillation: Z_m = 10m, F = 6832.8 cos (.00675t).

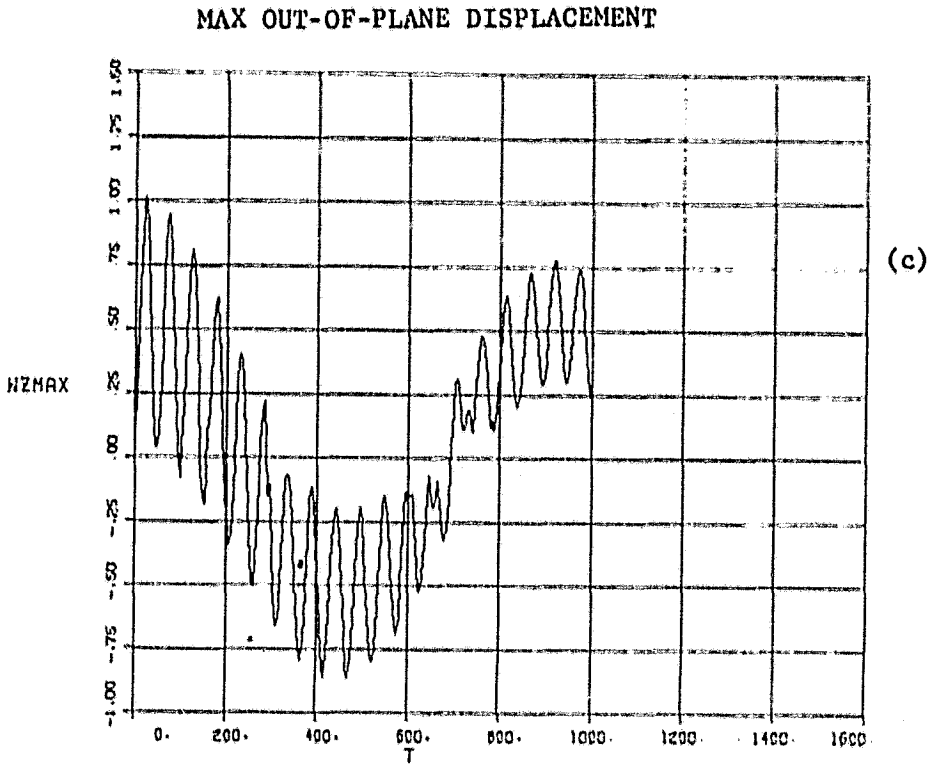

(c)

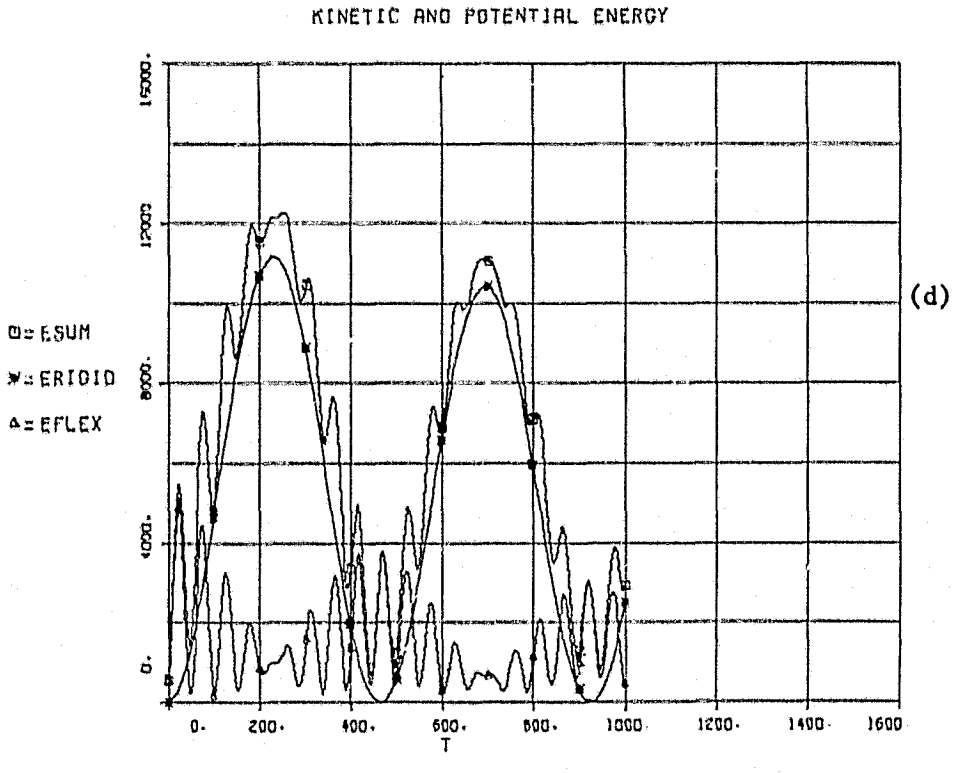

(d)

Figure 14. Surface Response to Collector Bending Oscillation: Z_m = 10m, F = 6832.8 cos (.00675t) (Cont.).

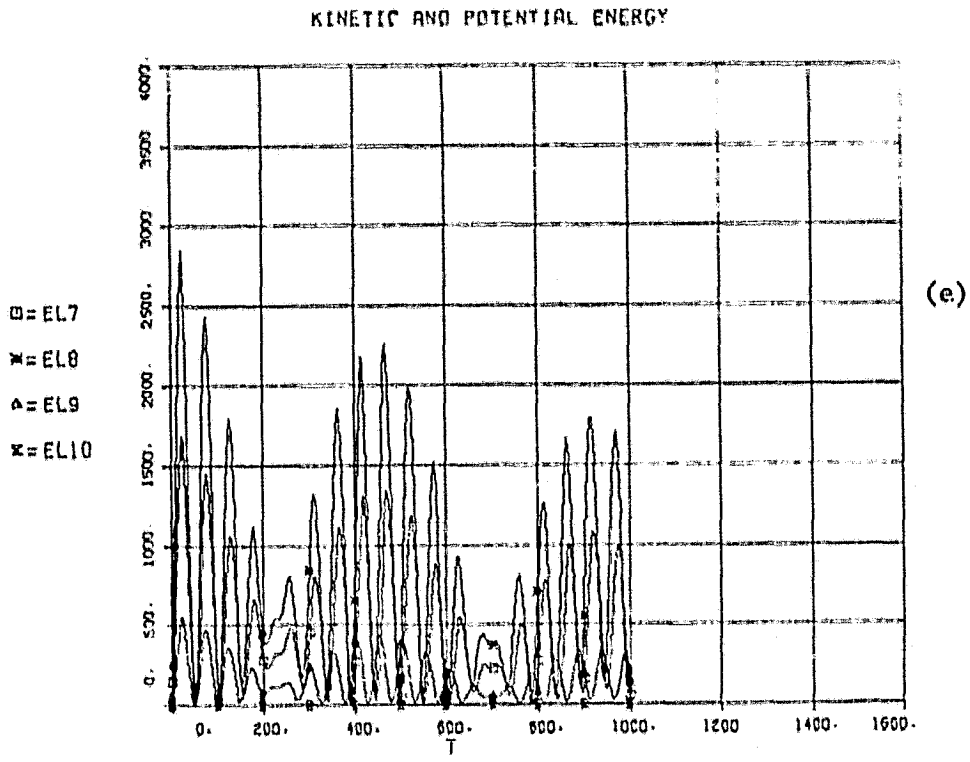

(e)

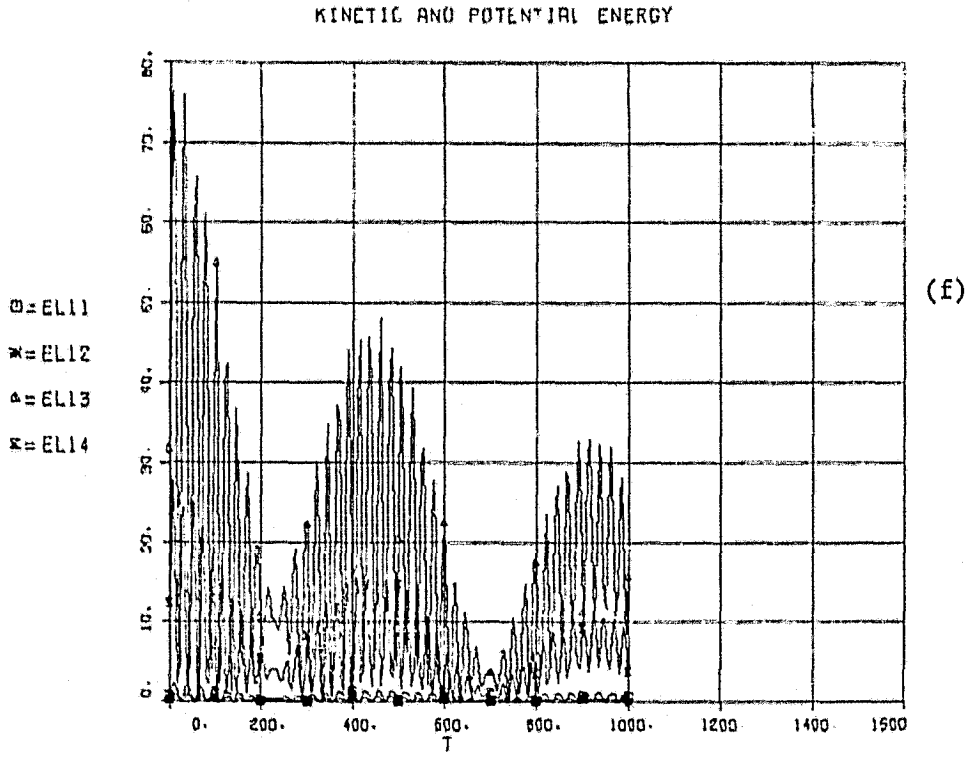

(f)

Figure 14. Surface Response to Collector Bending Oscillation: Z_m = 10m, F = 6832.8 cos (.00675t)(Cont.).

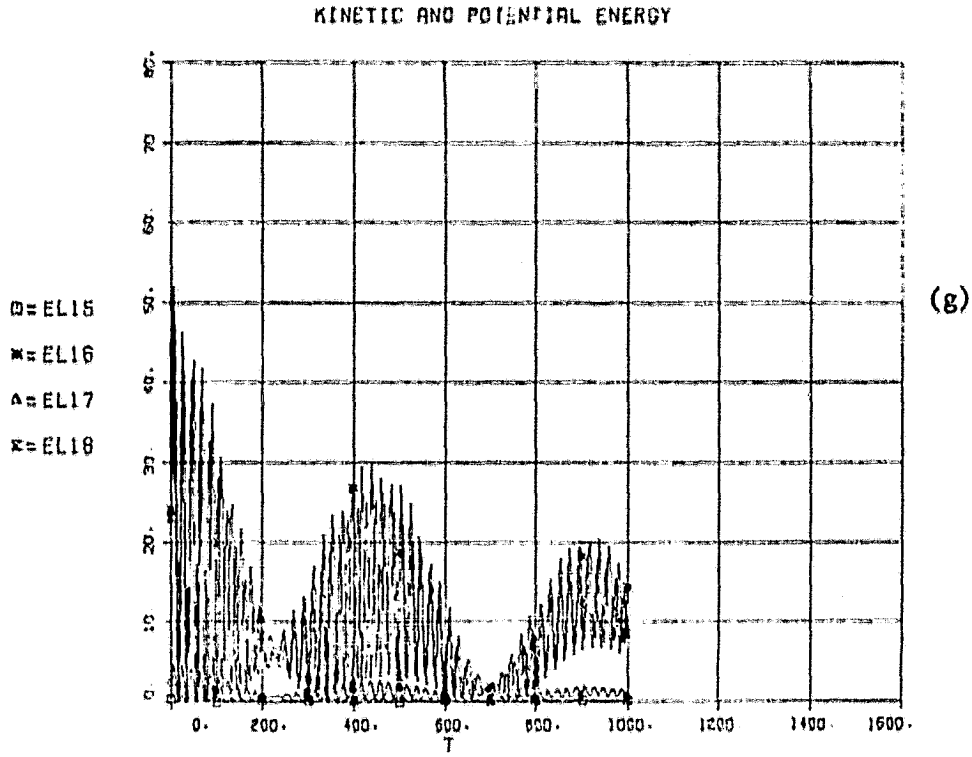

(g)

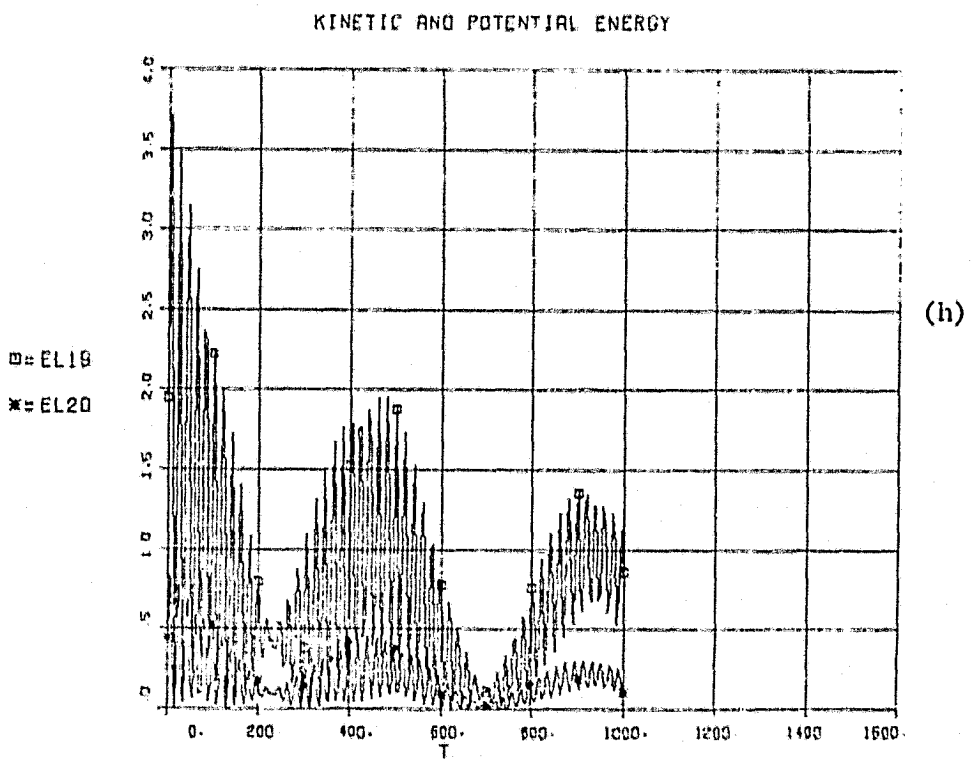

(h)

Figure 14. Surface Response to Collector Bending Oscillation: Z_m = 10m, F = 6832.8 cos (.00675t)(Cont.).

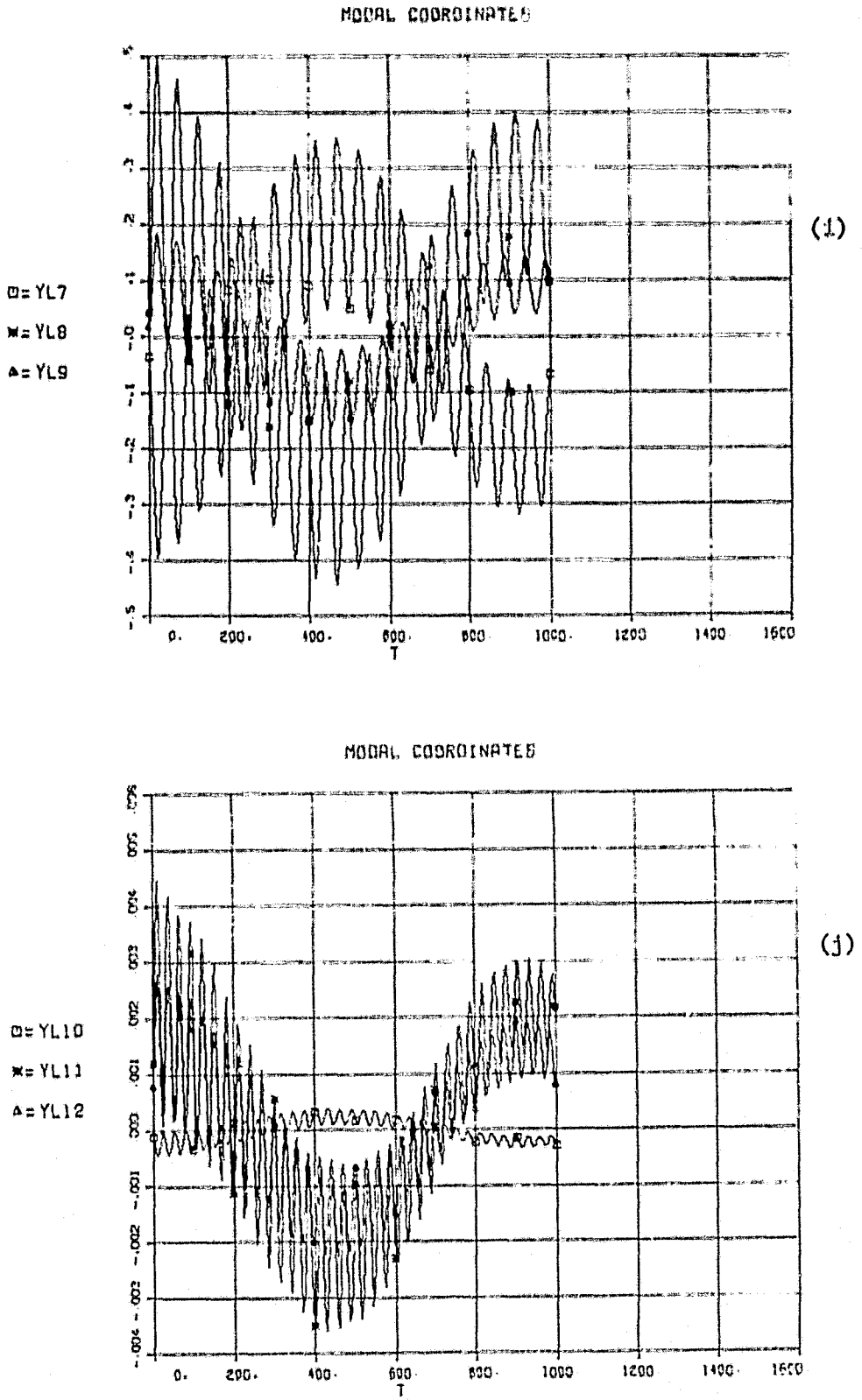

Figure 14. Surface Response to Collector Bending Oscillation: Z_m = 10m, F = 6832.8 cos (.00675t)(Cont.).

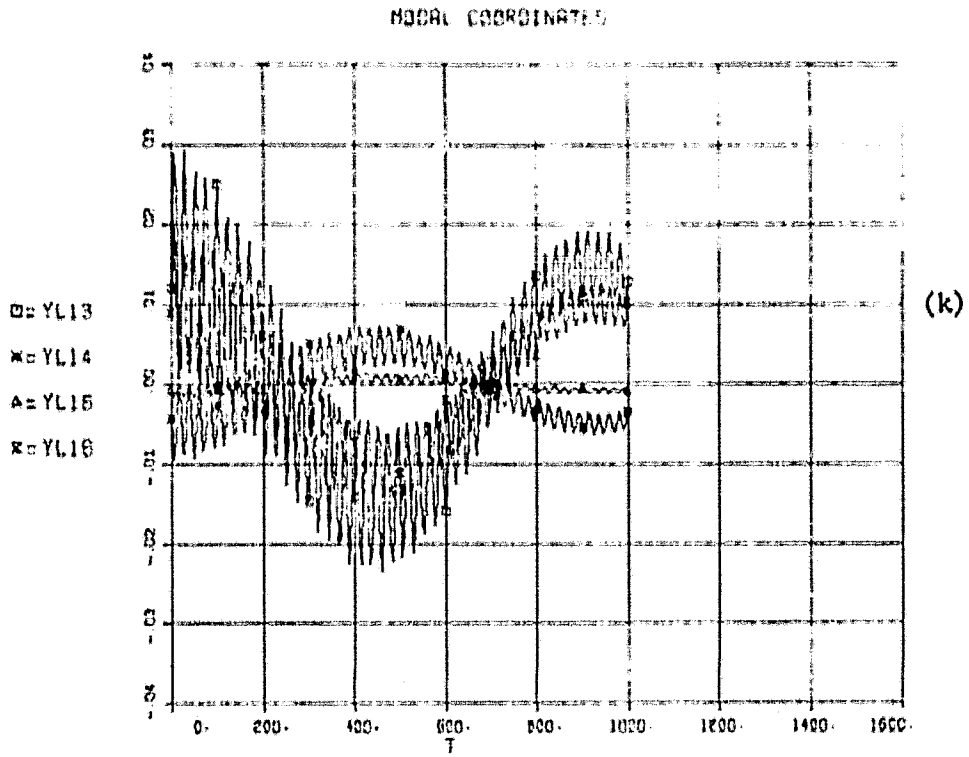

(k)

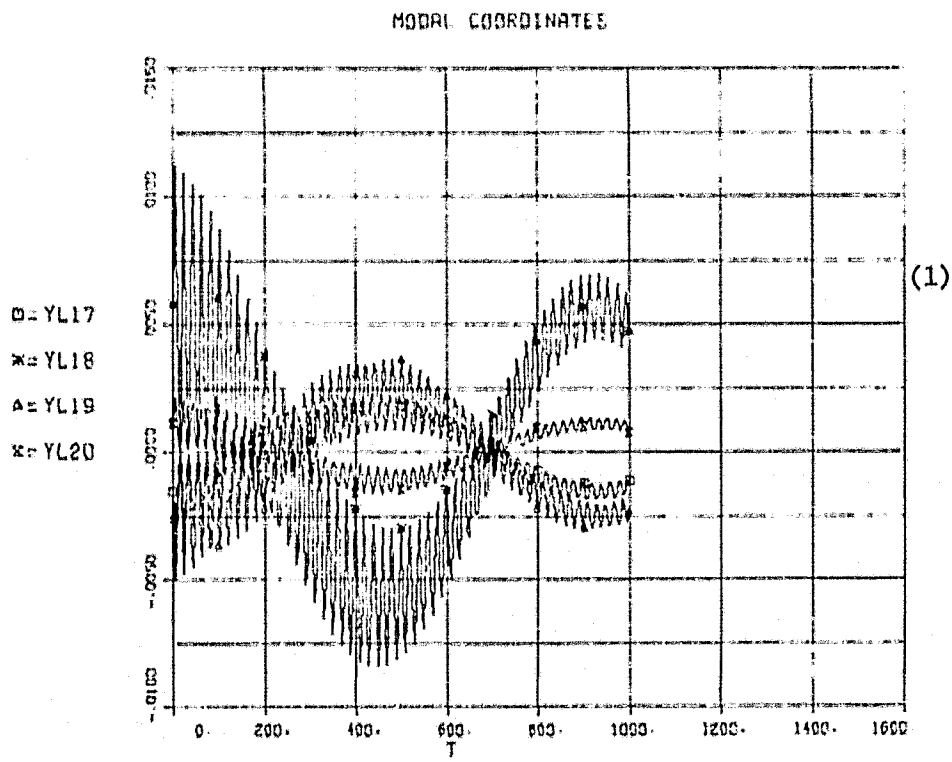

(1)

Figure 14. Surface Response to Collector Bending Oscillation: Z_m = 10m, F = 6832.8 cos (.00675t) (Cont.).

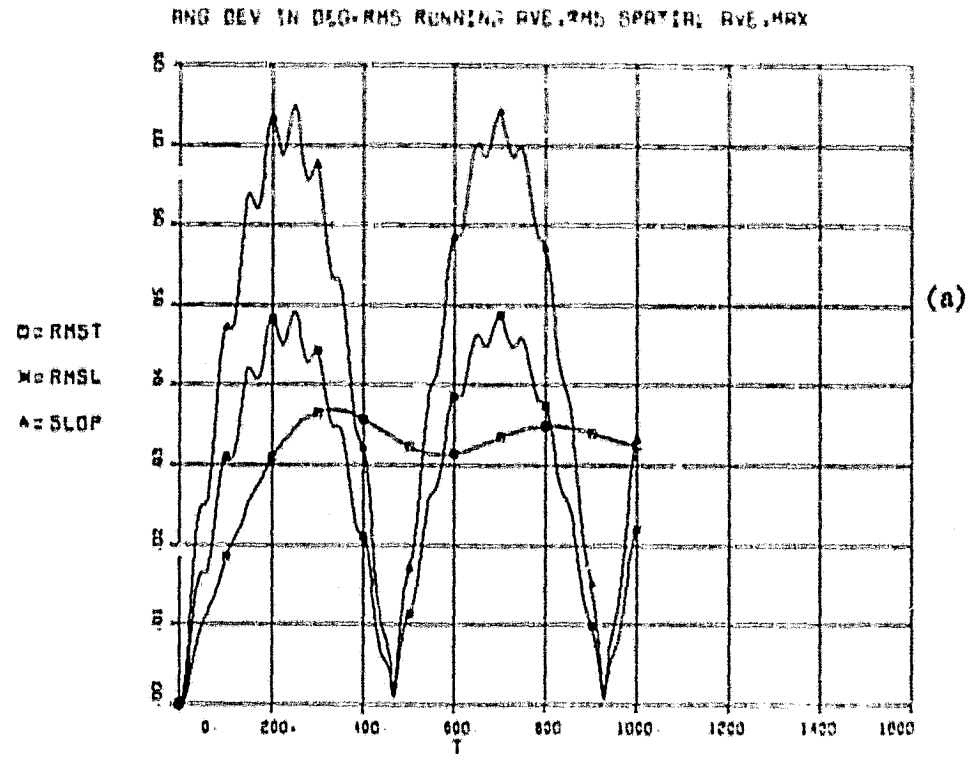

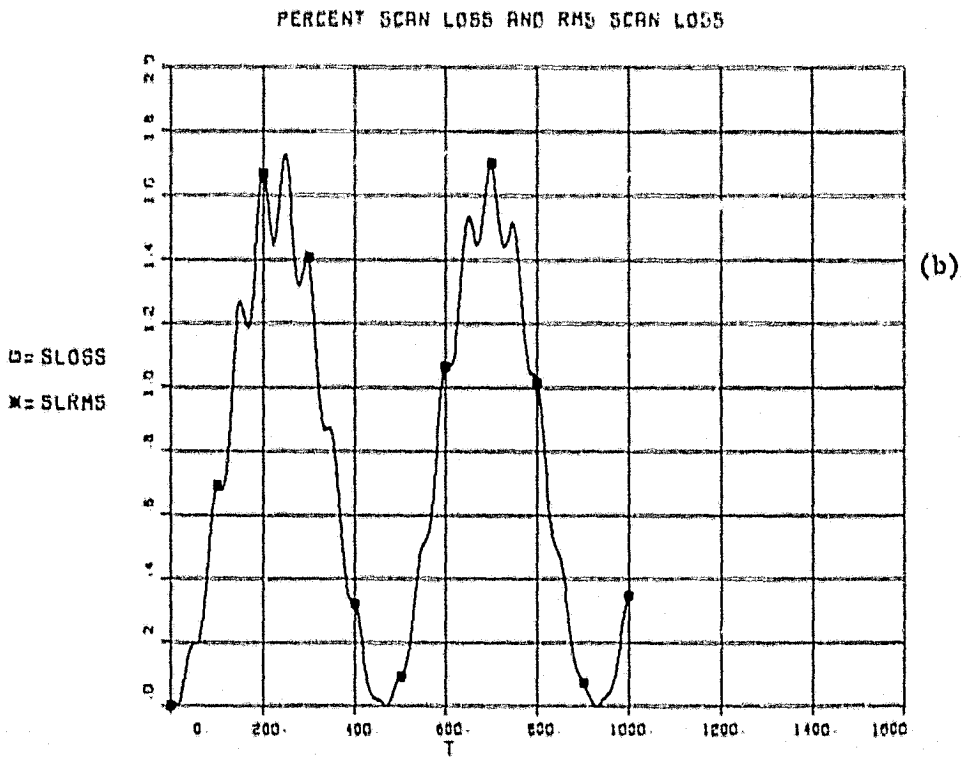

Figure 15. Surface Response to Collector Bending Oscillation: Z_m = 10m, F = 6832.8 sin (.00675t).

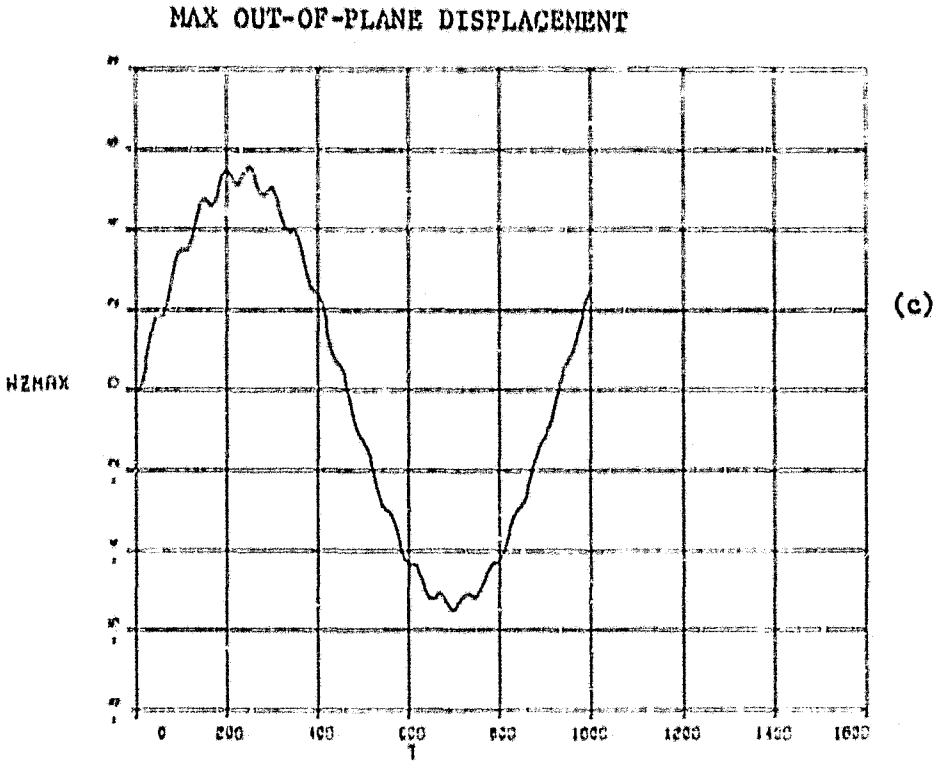

(c)

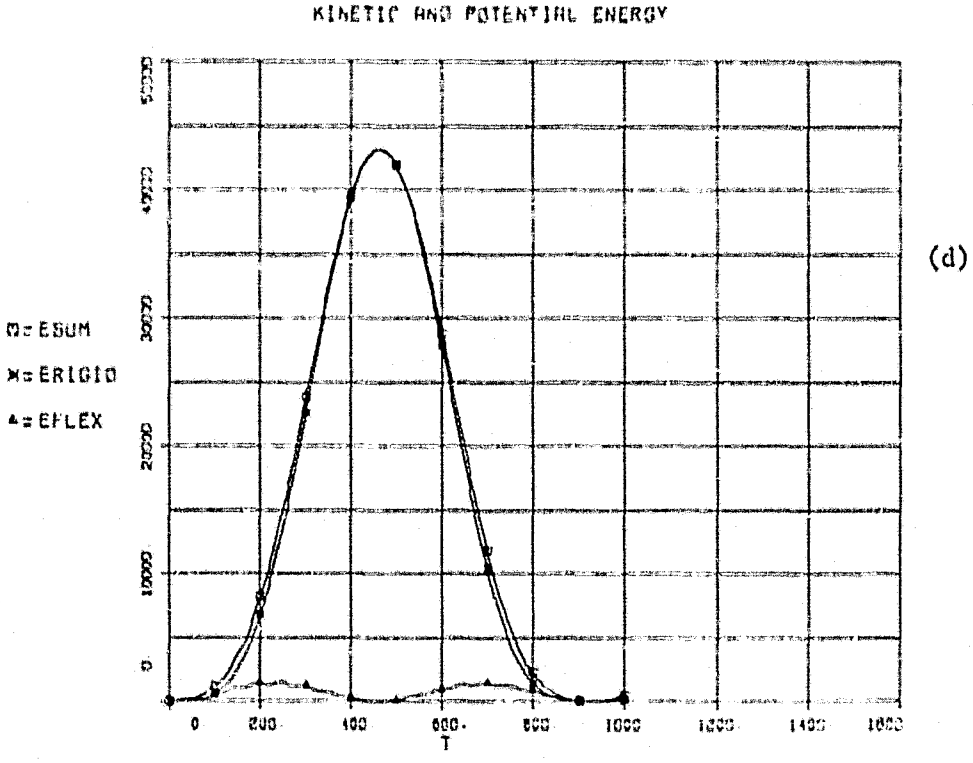

(d)

Figure 15. Surface Response to Collector Bending Oscillation: Z_m = 10m, F = 6832.8 sin (.00675t) (Cont.).

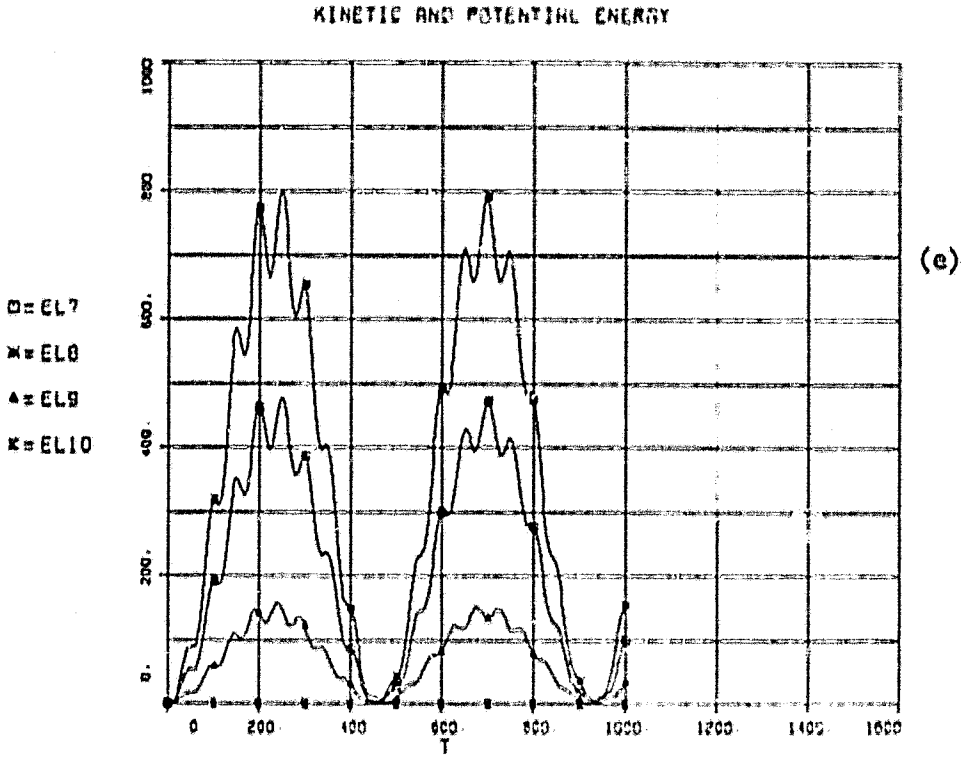

(e)

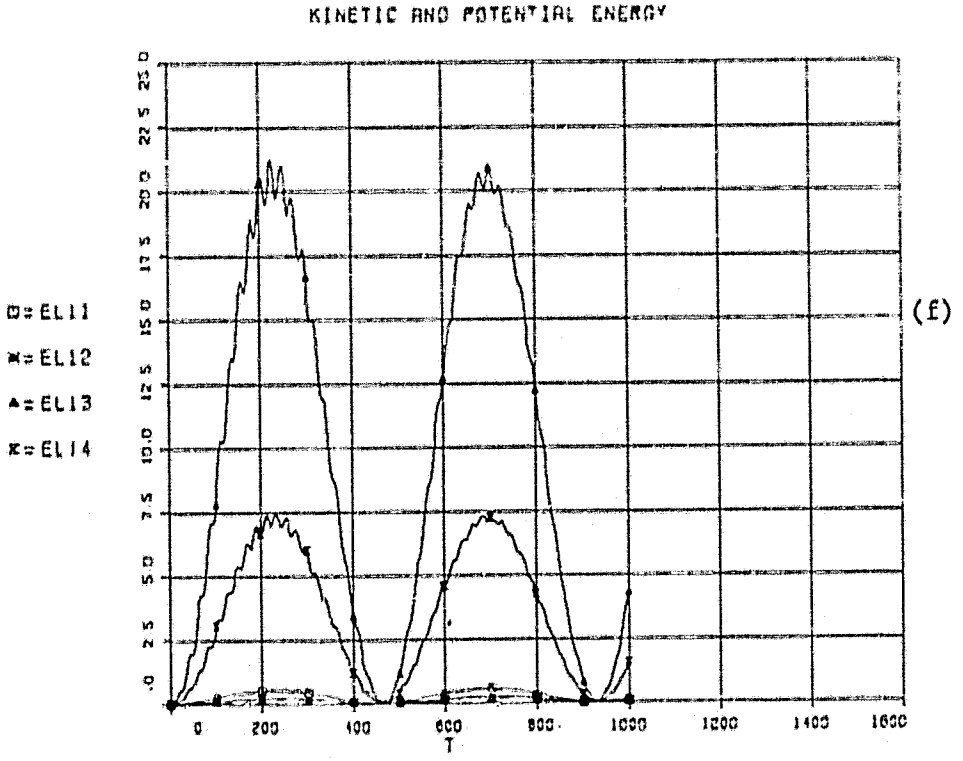

(f)

Figure 15. Surface Response to Collector Bending Oscillation: Z_m = 10m, F = 6832.8 sin (.00675t) (Cont.).

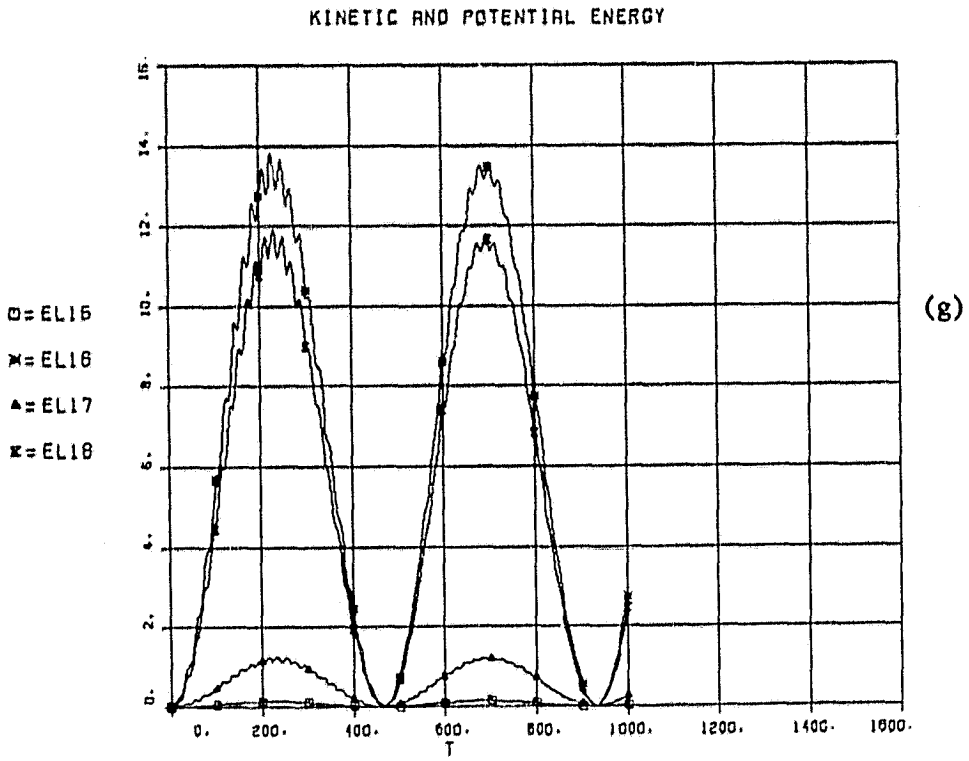

(g)

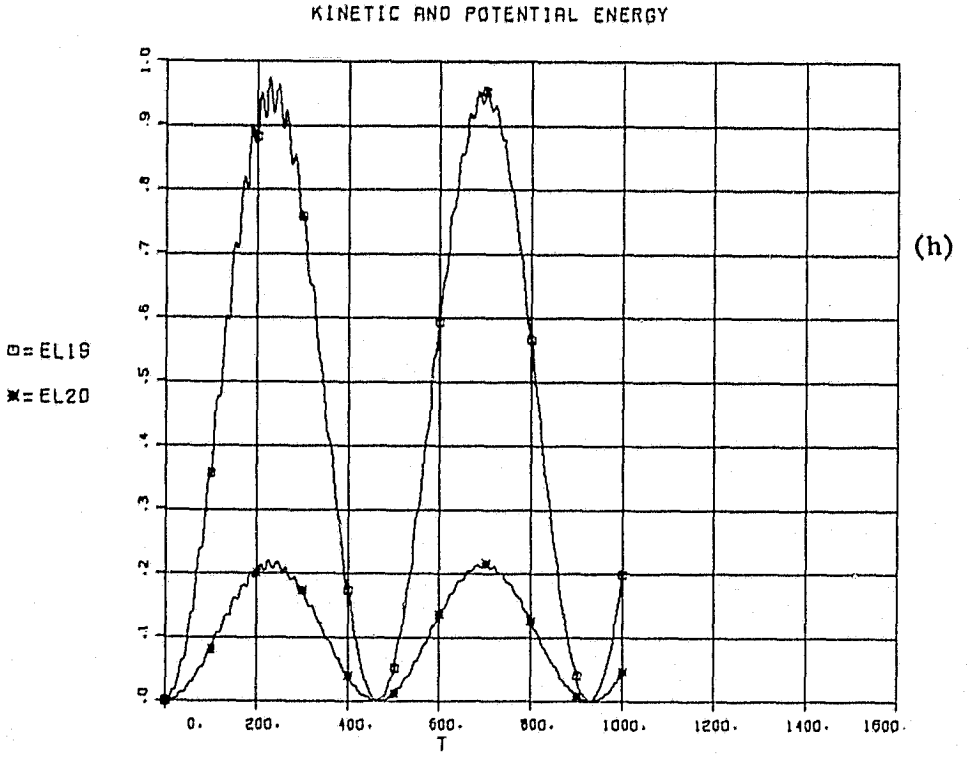

(h)

Figure 15. Surface Response to Collector Bending Oscillation: Z_m = 10m, F = 6832.8 sin (.00675t) (Cont.).

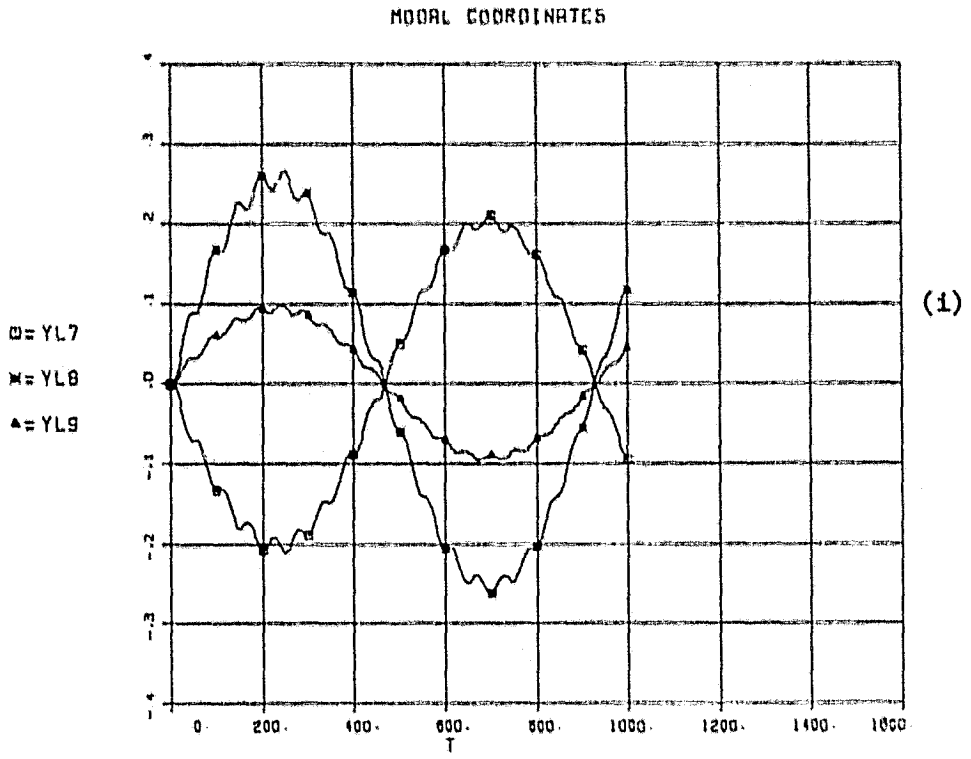

(i)

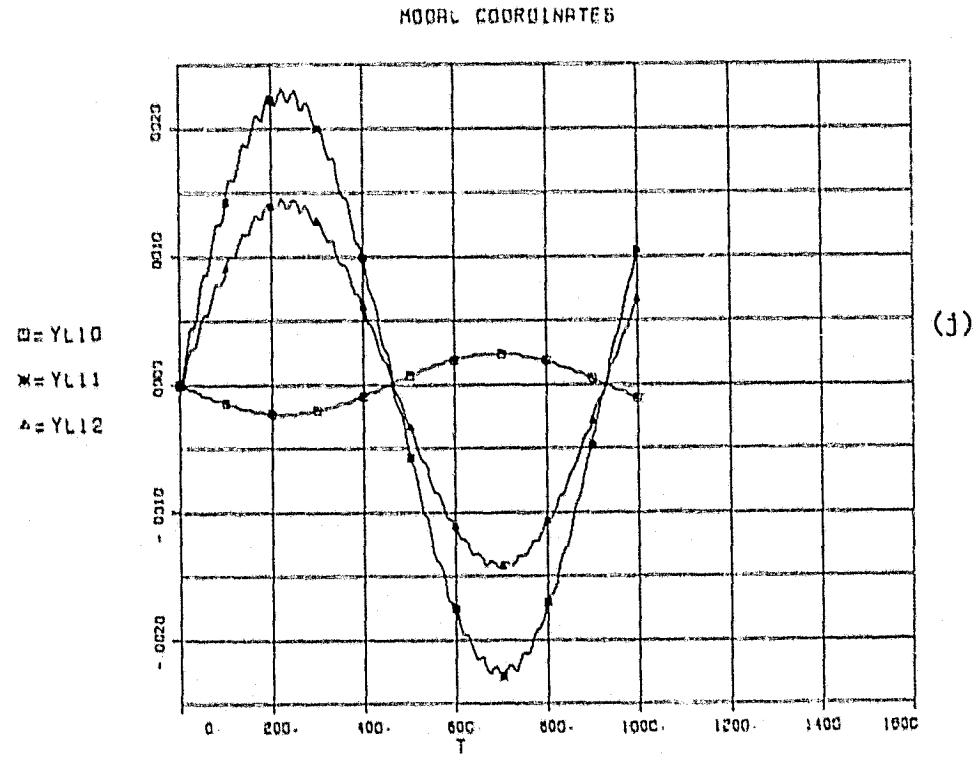

(j)

Figure 15. Surface Response to Collector Bending Oscillation: Z_m = 10m, F = 6832.8 sin (.00675t)(Cont.).

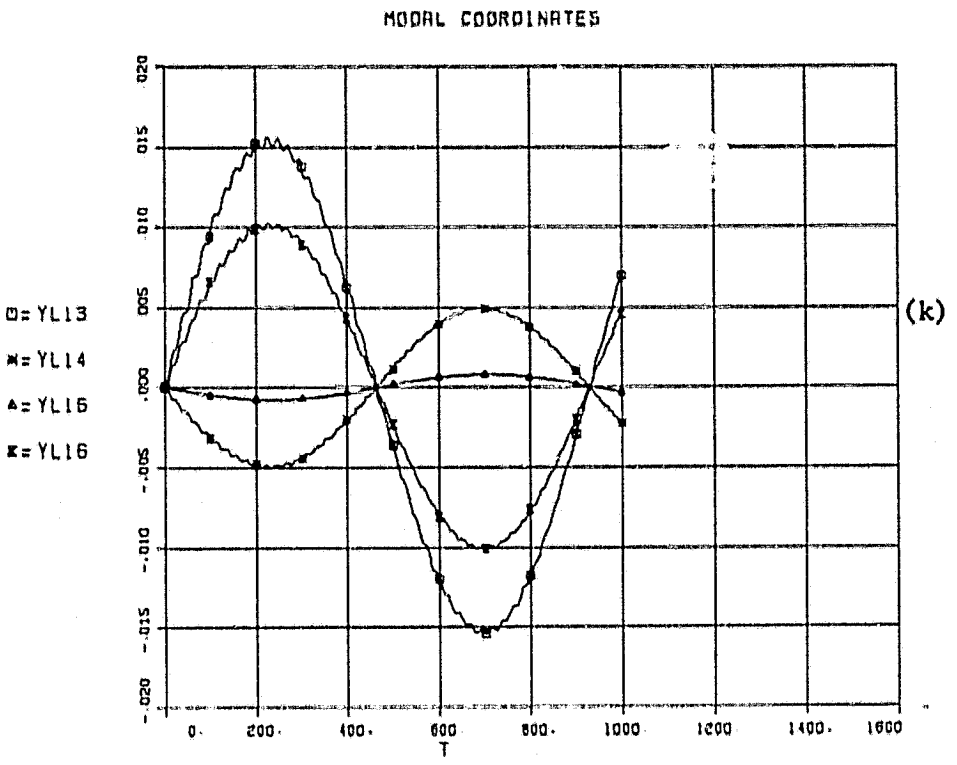

(k)

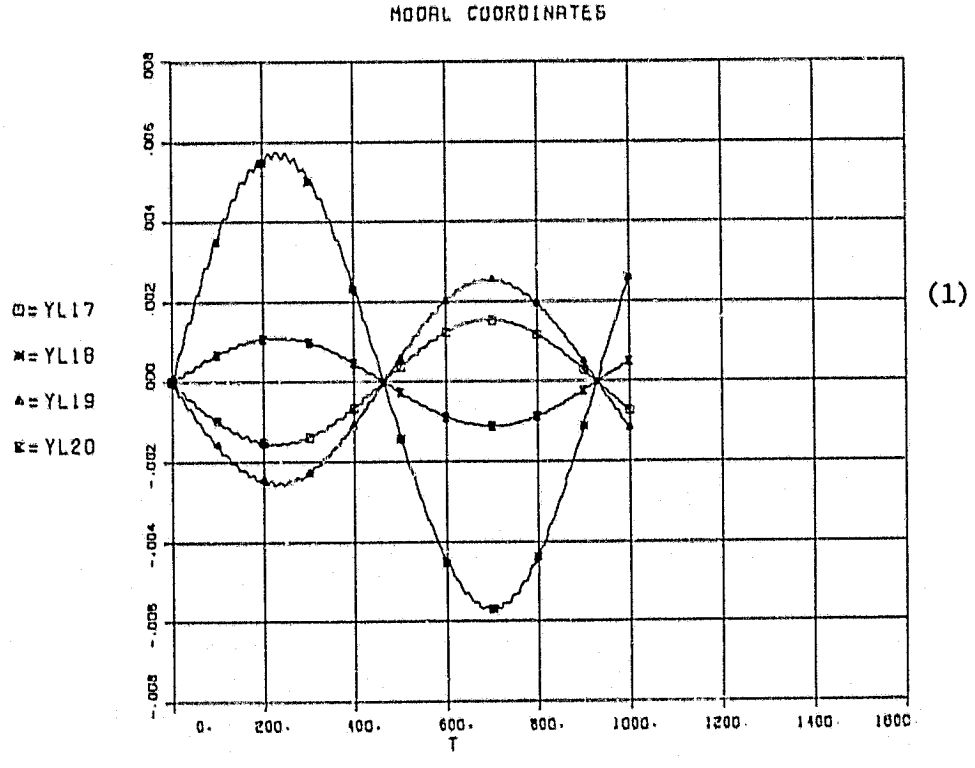

(l)

Figure 15. Surface Response to Collector Bending Oscillation: Z_m = 10m, F = 6832.8 sin (.00675t)(Cont.).

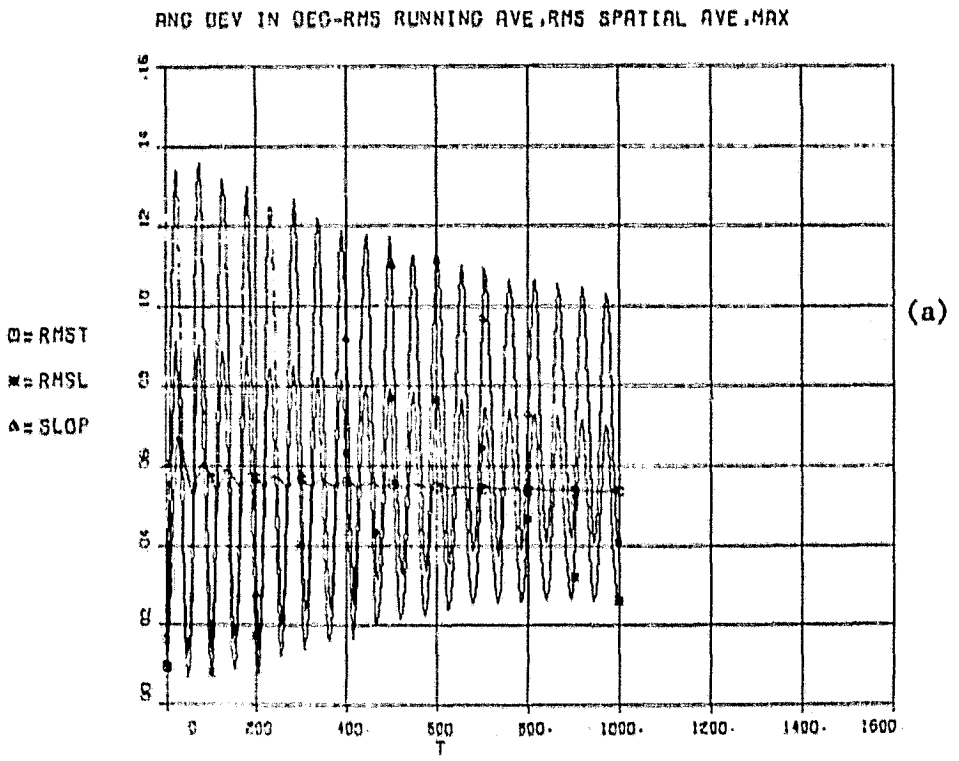

(a)

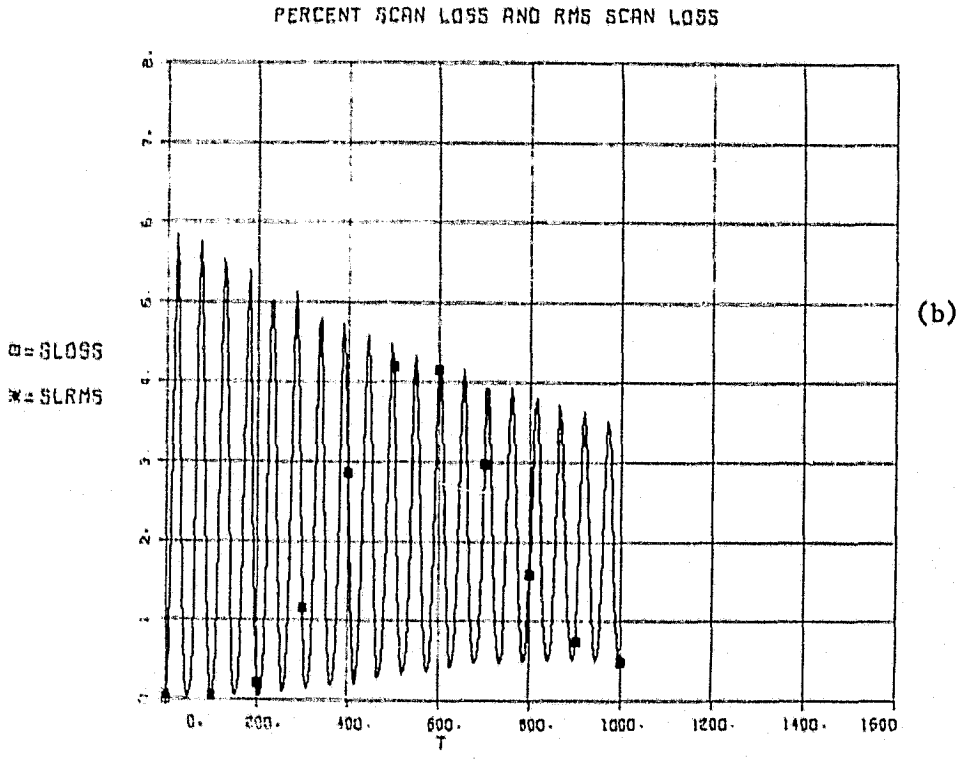

(b)

Figure 16. Surface Response to Step Acceleration, F = 6832.8 U(t).

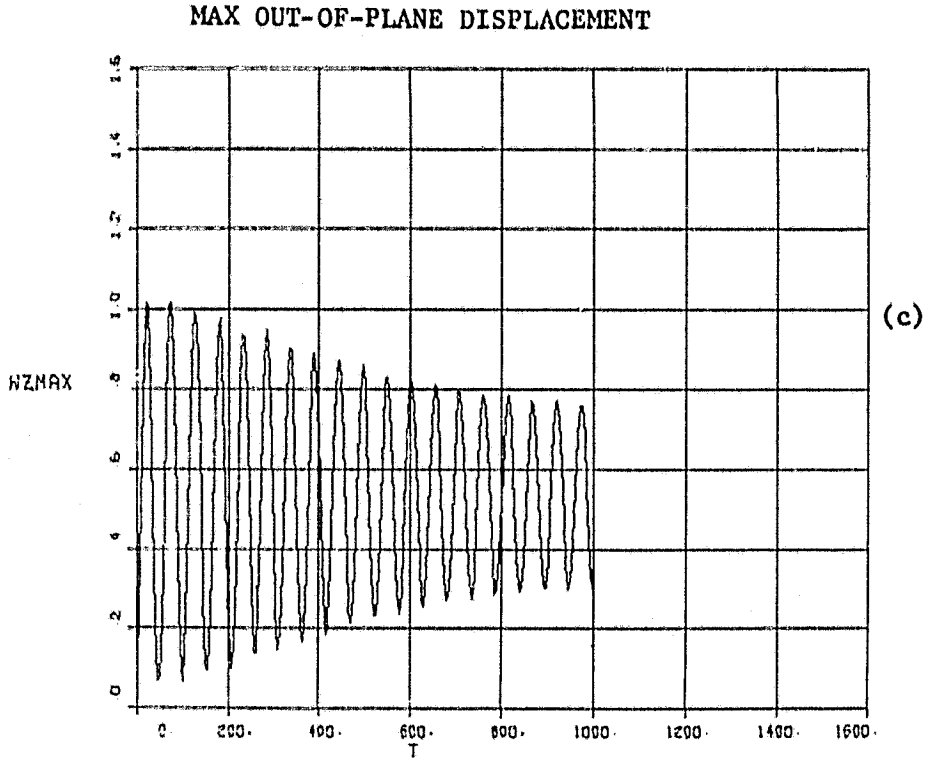

(c)

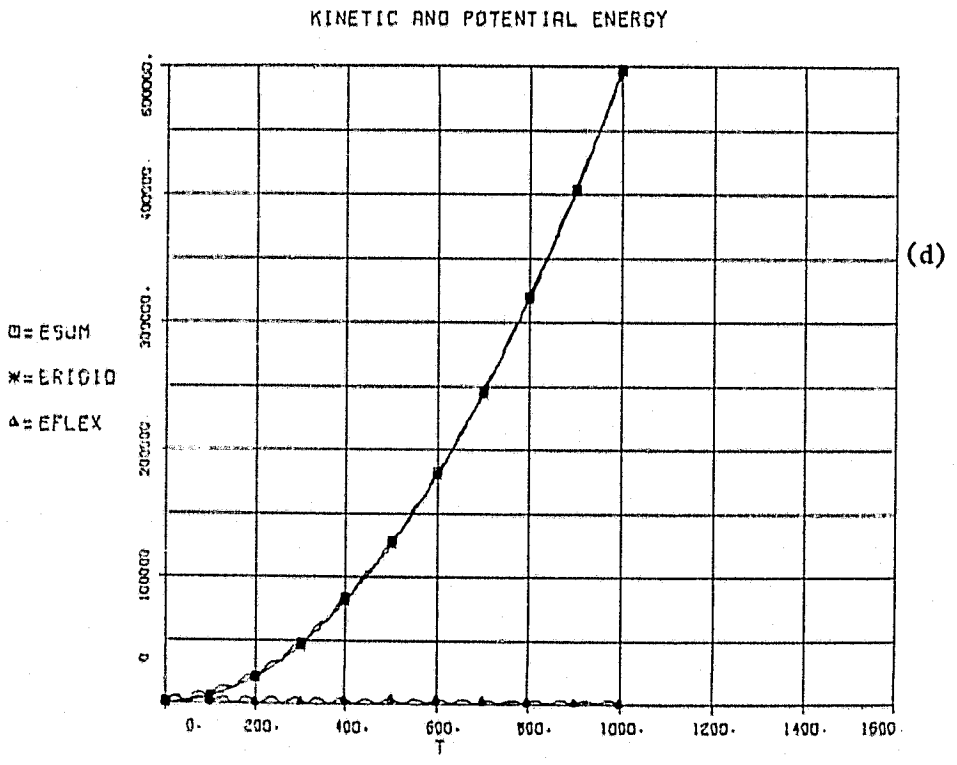

(d)

Figure 16. Surface Response to Step Acceleration, F = 6832.8 U(t) (Cont.).

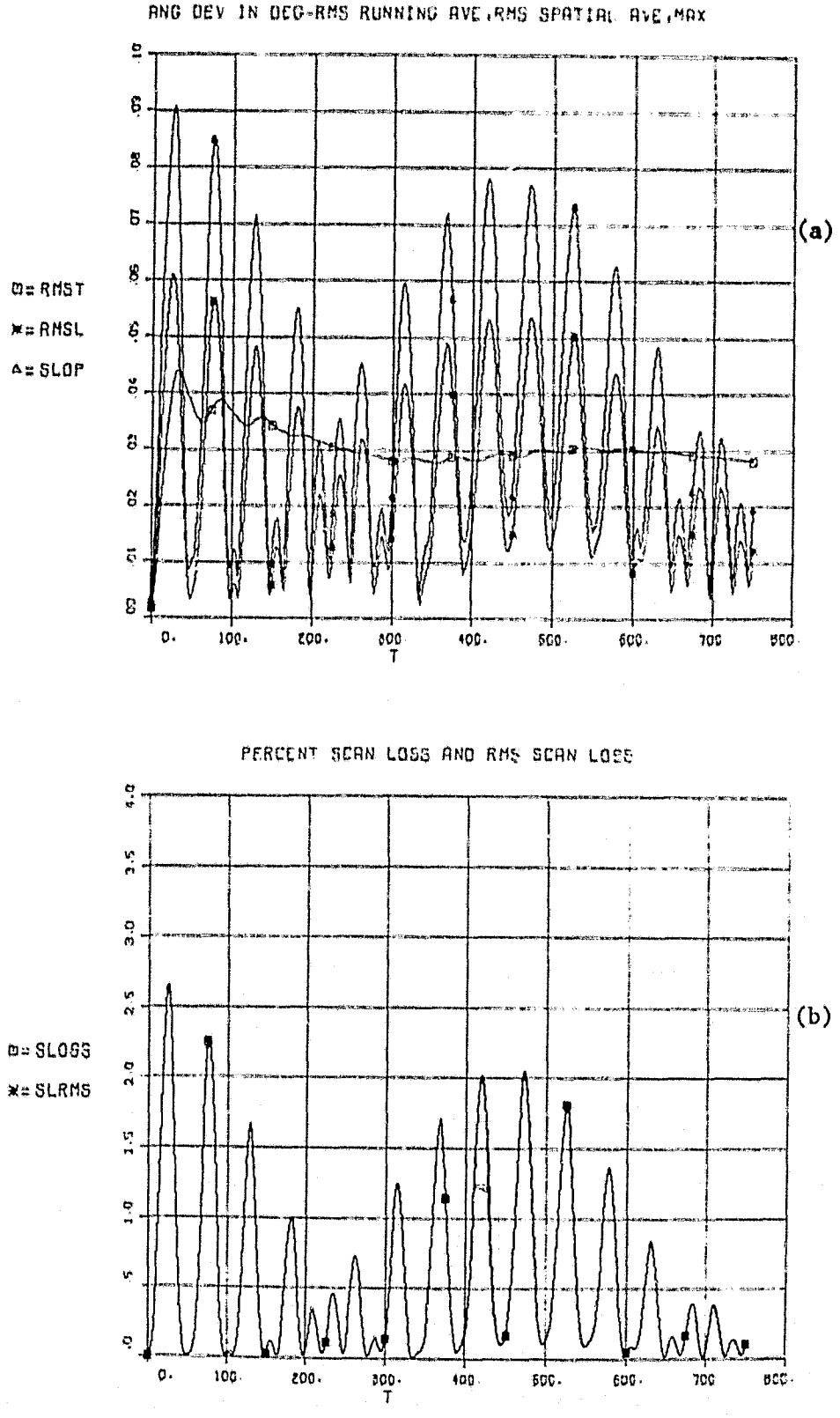

Figure 17. Surface Response to Collector Thermal Bending Disturbance, $\alpha = 10^{-6}$ m/m/°C, F = 4558.5 cos (.00675t).

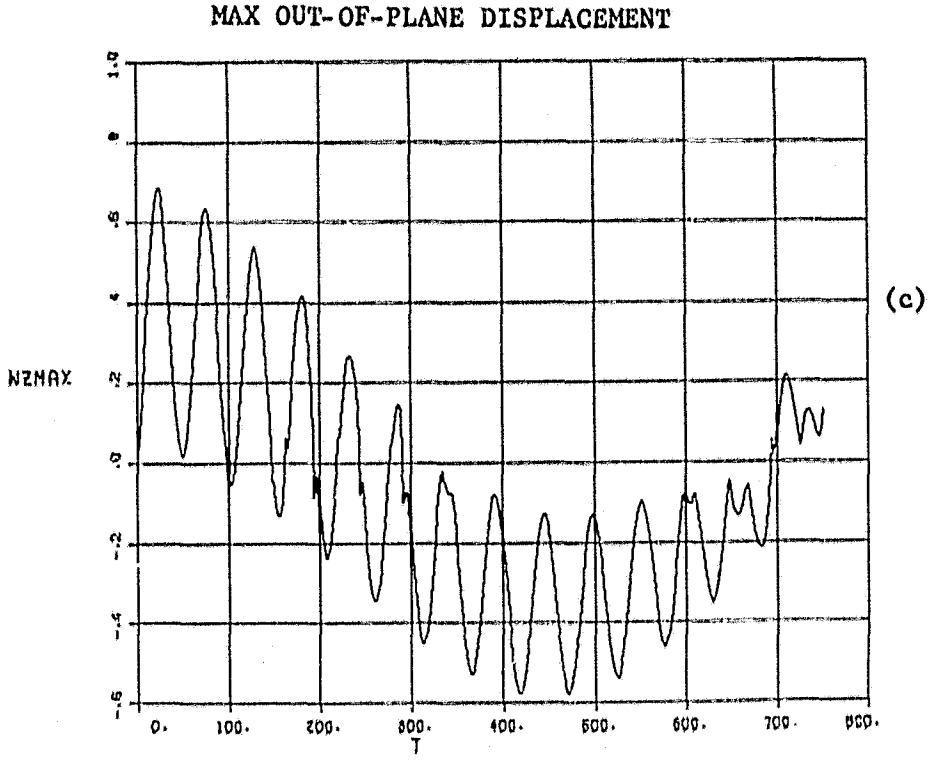

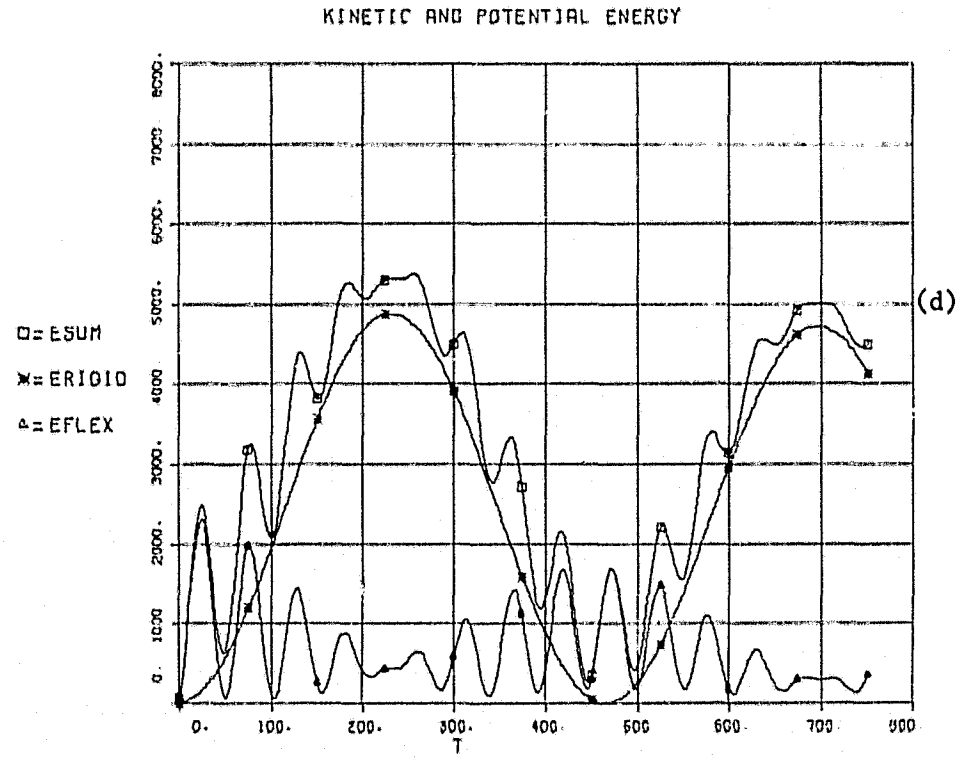

Figure 17. Surface Response to Collector Thermal Bending Disturbance, $\alpha = 10^{-6}$ m/m/°C, F = 4558.5 cos (.00675t) (Cont.).

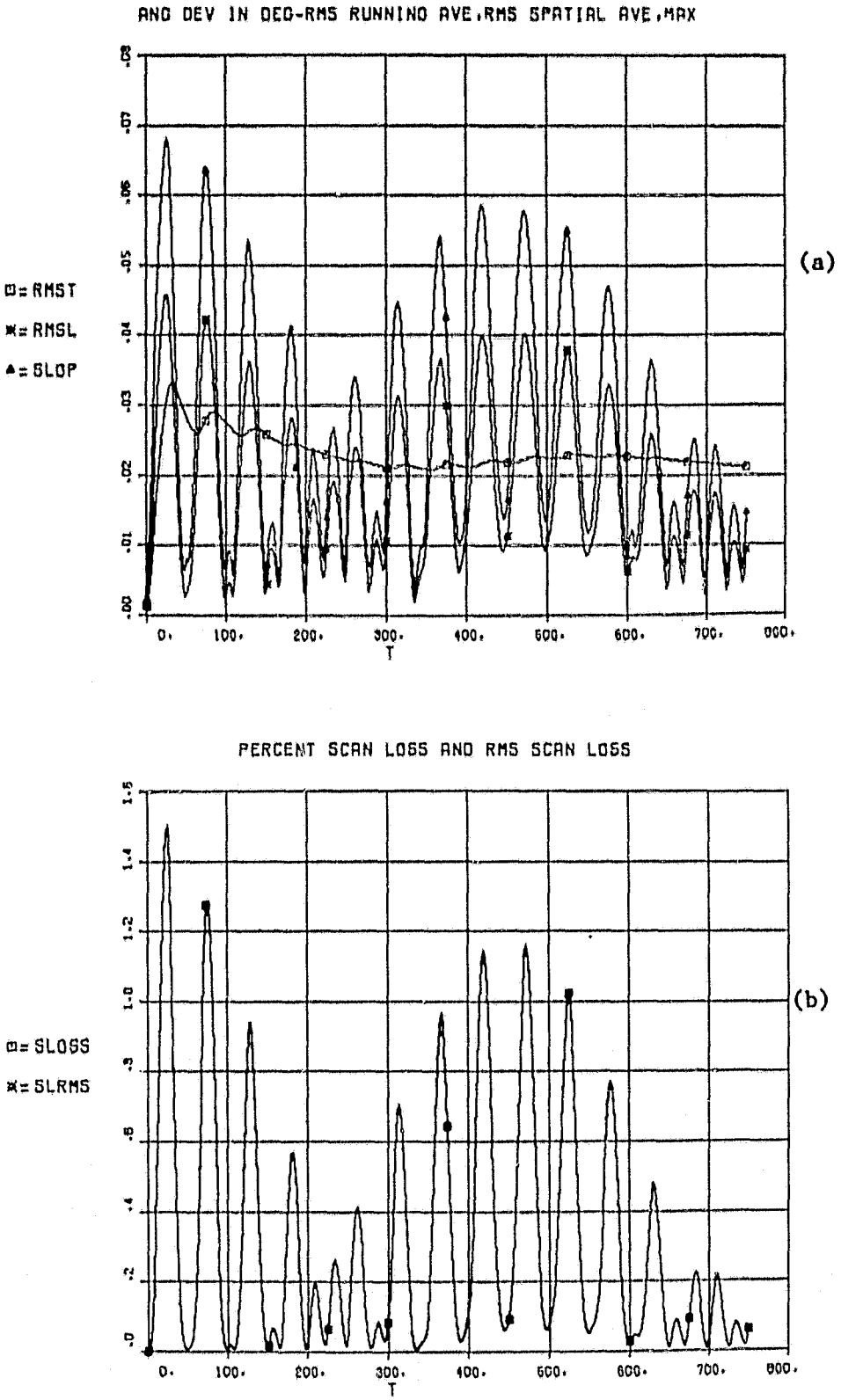

Figure 18. Surface Response to Collector Thermal Bending Disturbance, $\alpha = .75 \times 10^{-6}$ m/m/°C, F = 3417.2 cos (.00675t).

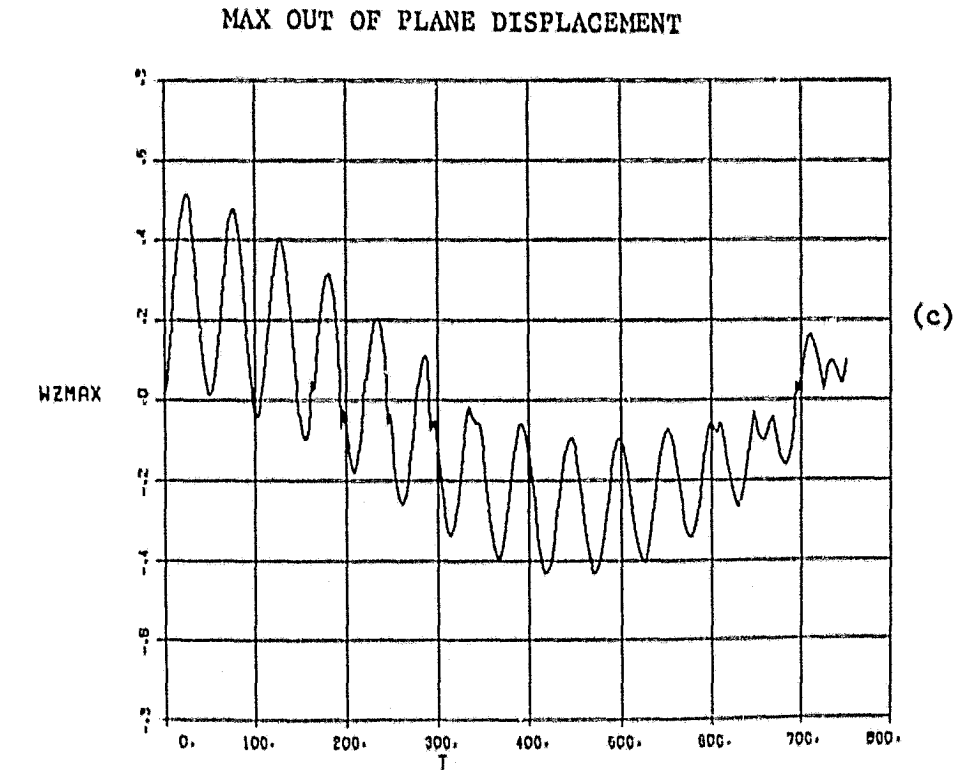

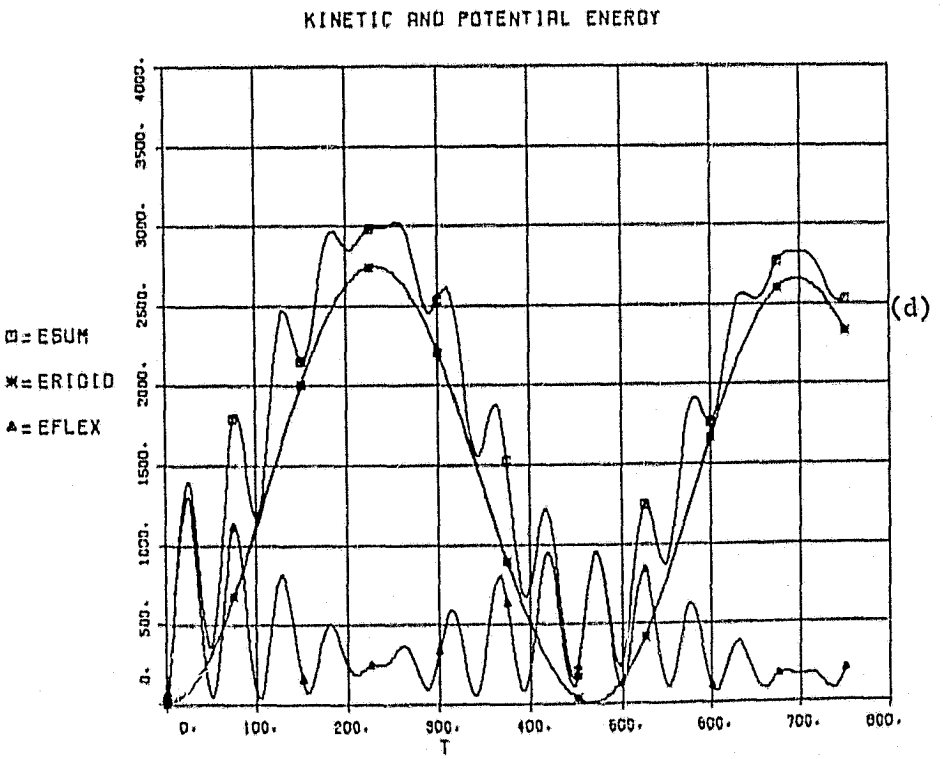

Figure 18. Surface Response to Collector Thermal Bending Disturbance, $\alpha = .75 \times 10^{-6}$ m/m/°C, F = 3417.2 cos (.00675t) (Cont.).

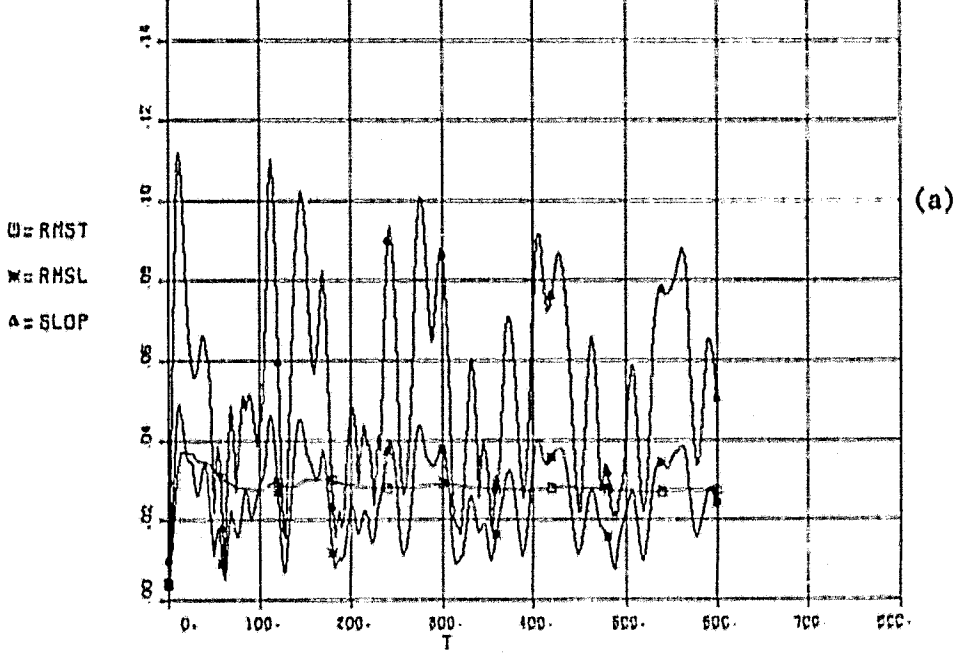

(a)

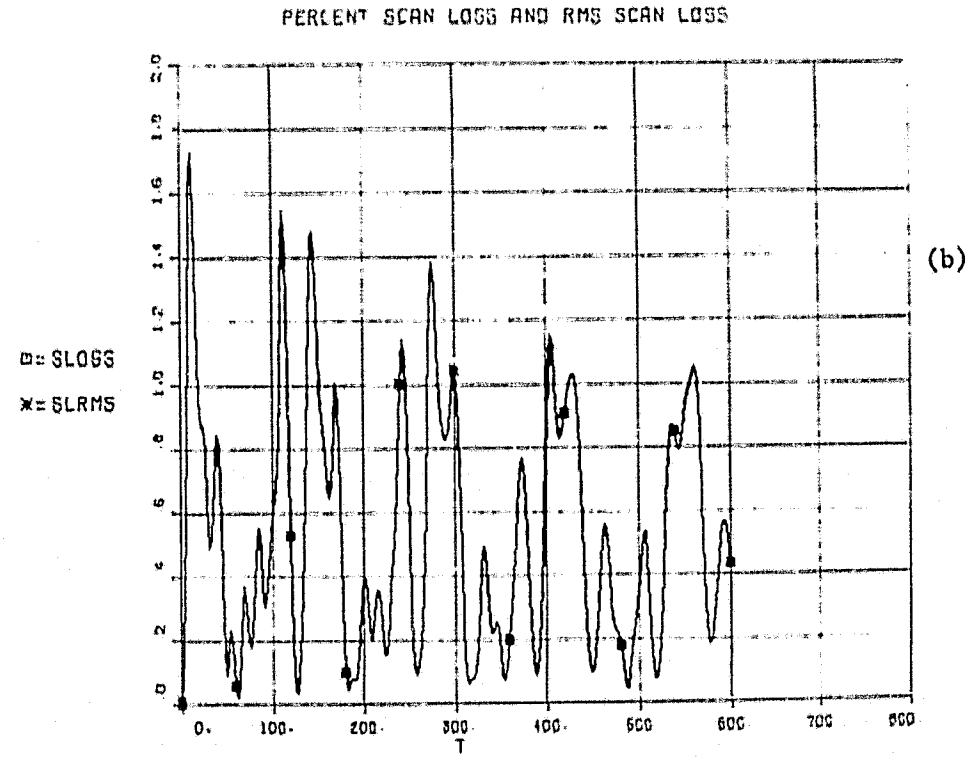

(b)

Figure 19. Surface Response to Collector Torsional Oscillation, $\theta = 1°$, $\tau = 6.453 \times 10^6 \cos(.0226t)$.

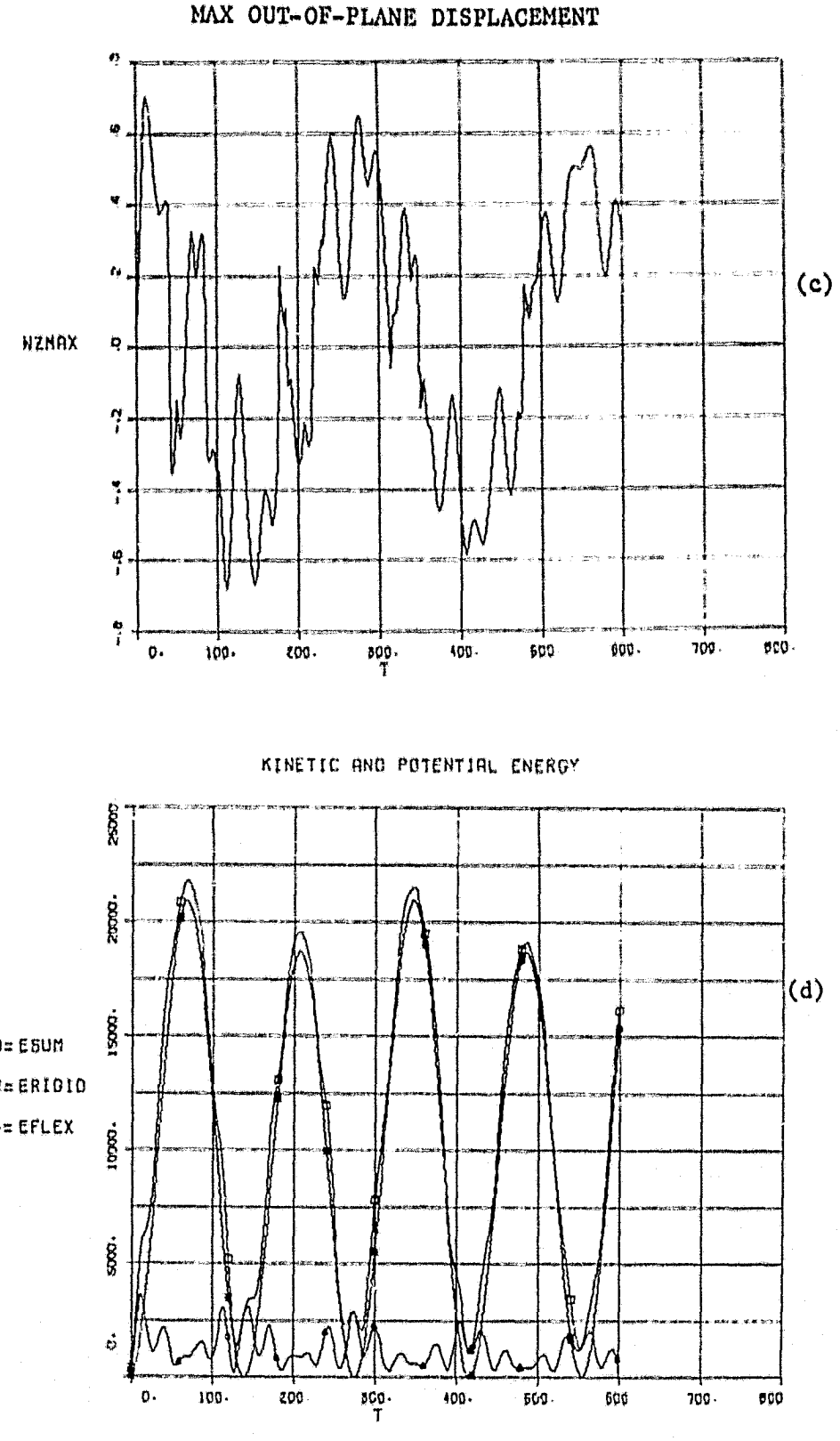

Figure 19. Surface Response to Collector Torsional Oscillation, $\theta = 1°$, $\tau = 6.453 \times 10^6 \cos(.0226t)$(Cont.).

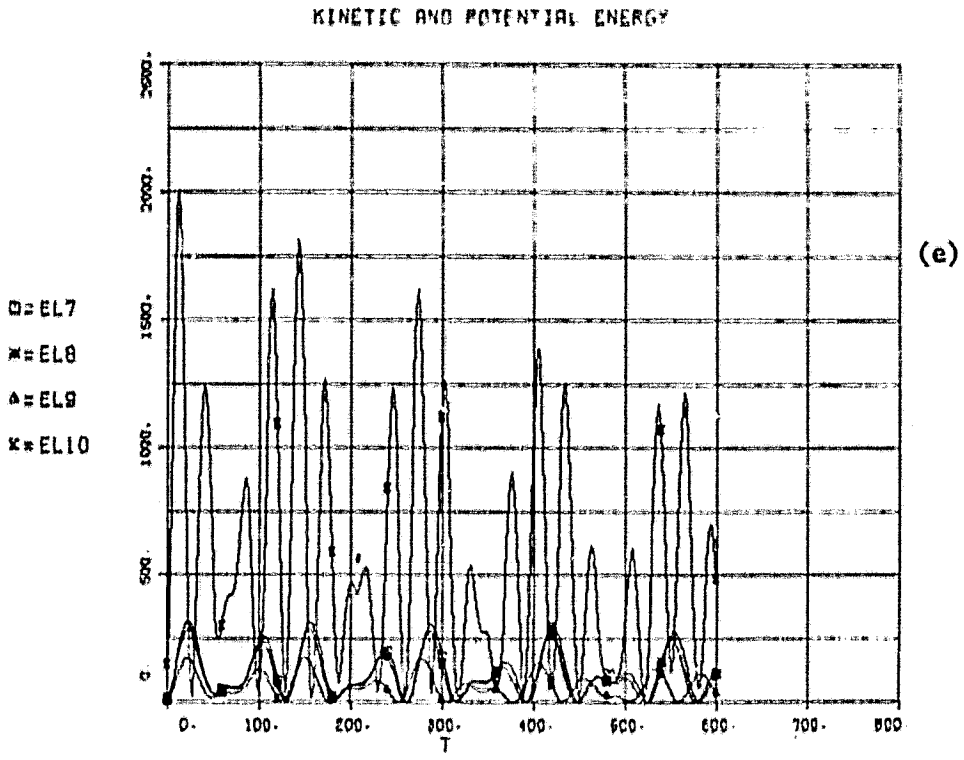

(e)

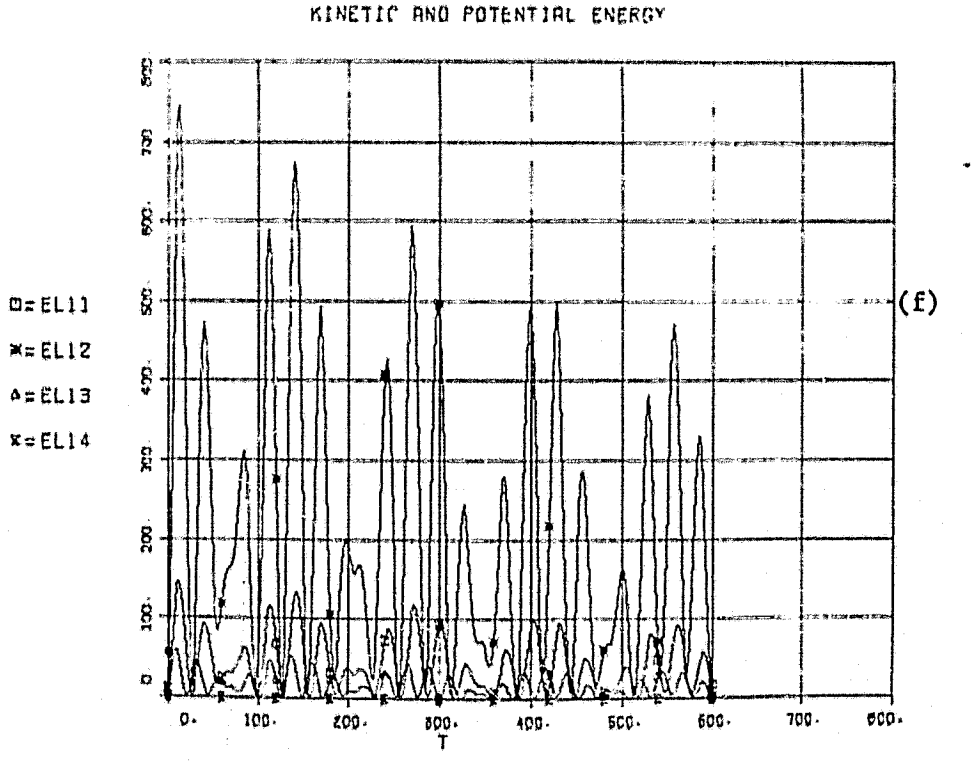

(f)

Figure 19. Surface Response to Collector Torsional Oscillation, $\theta = 1°$, $\tau = 6.453 \times 10^6 \cos(.0226t)$(Cont.).

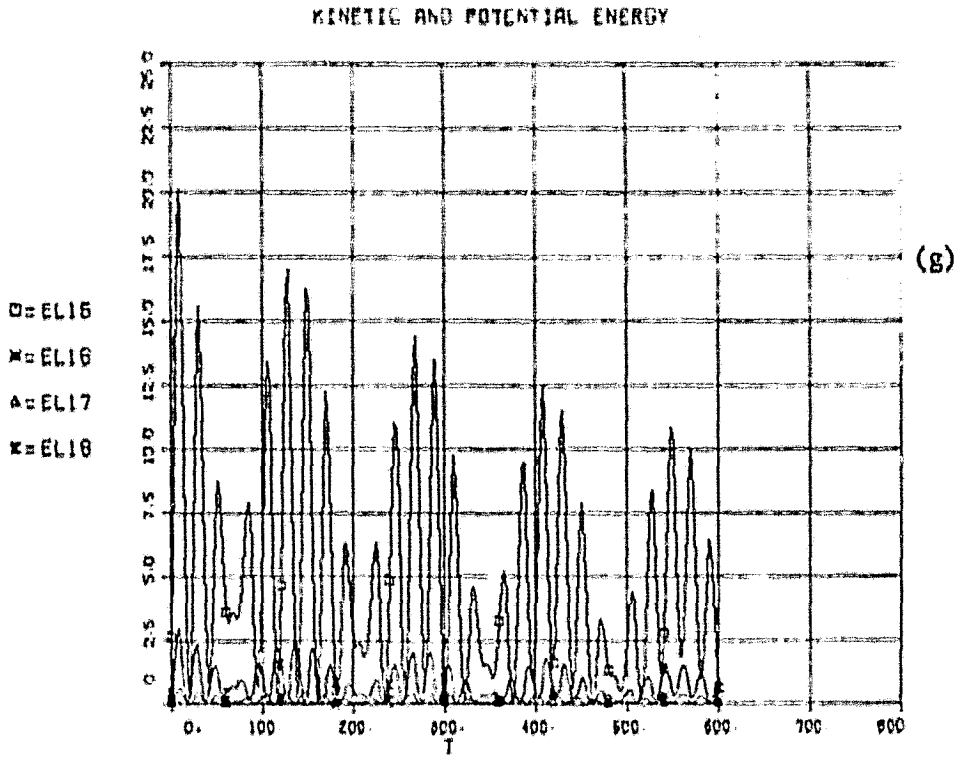

(g)

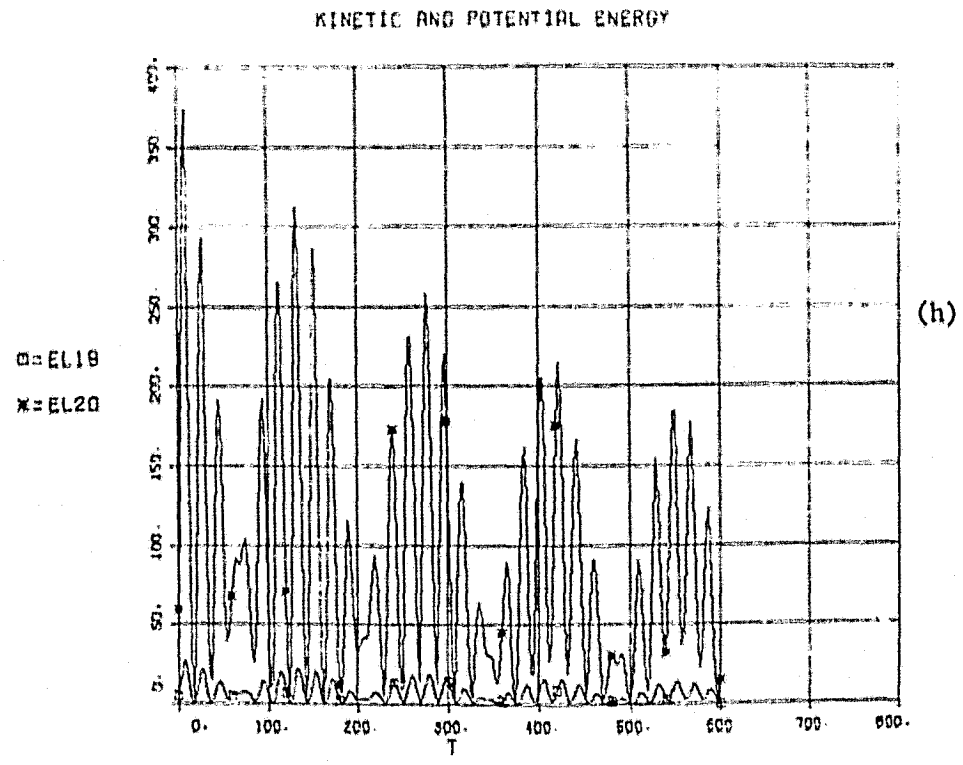

(h)

Figure 19. Surface Response to Collector Torsional Oscillation, $\theta = 1°$, $\tau = 6.453 \times 10^6 \cos(.0226t)$(Cont.).

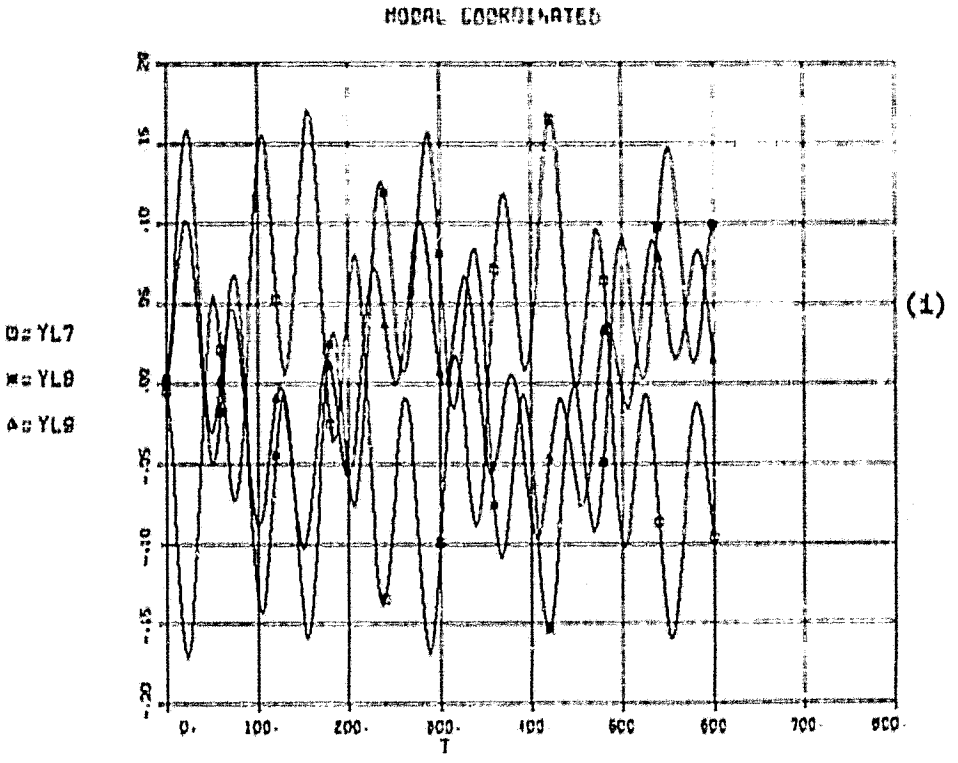

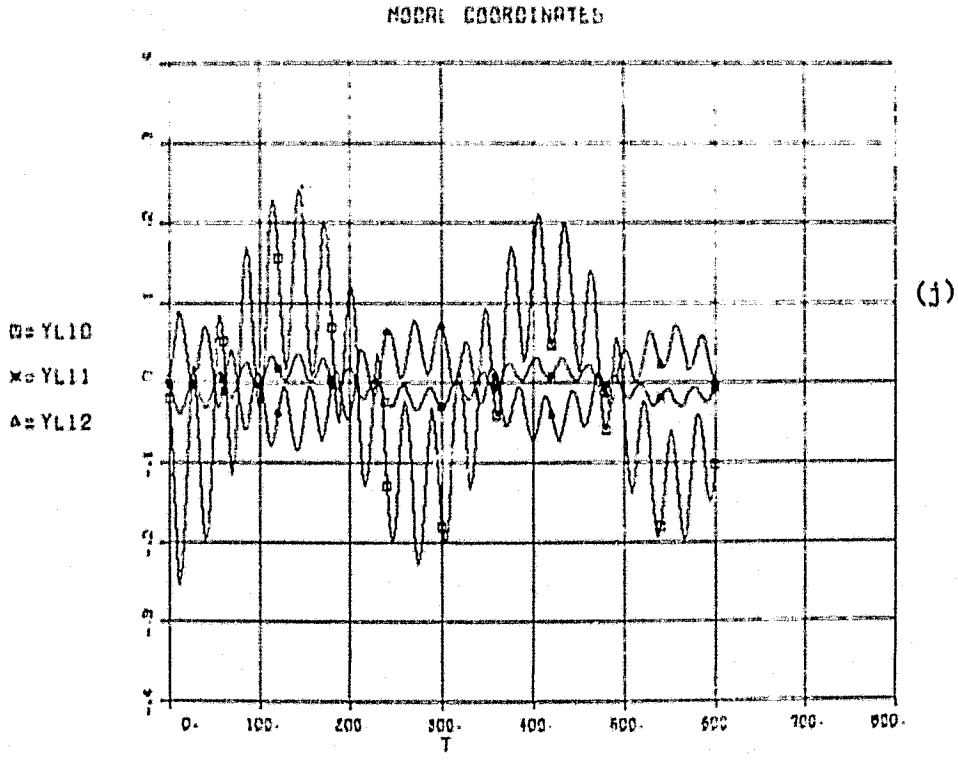

Figure 19. Surface Response to Collector Torsional Oscillation, $\theta = 1°$, $\tau = 6.453 \times 10^6 \cos(.0226t)$(Cont.).

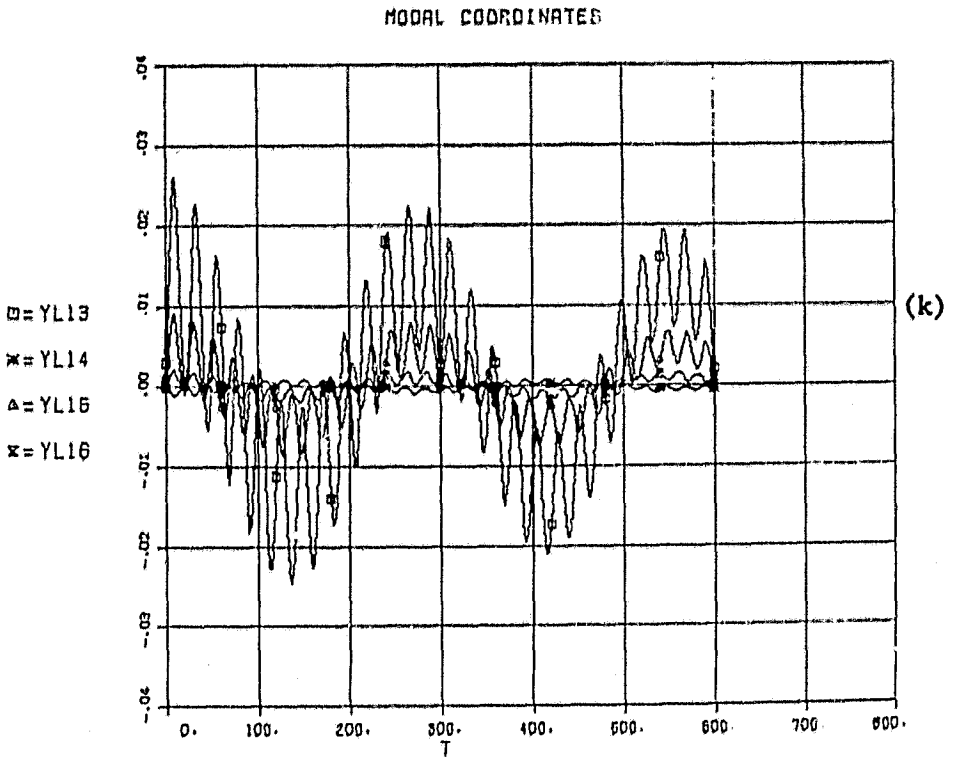

(k)

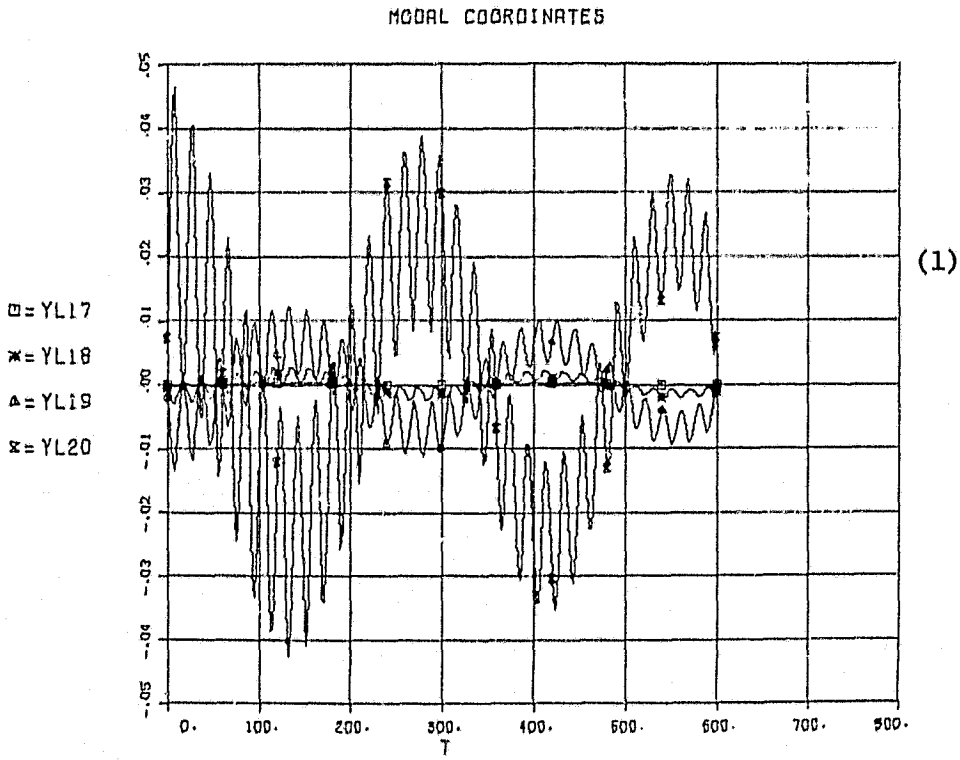

(l)

Figure 19. Surface Response to Collector Torsional Oscillation, $\theta = 1°$, $\tau = 6.453 \times 10^6 \cos(.0226t)$ (Cont.).

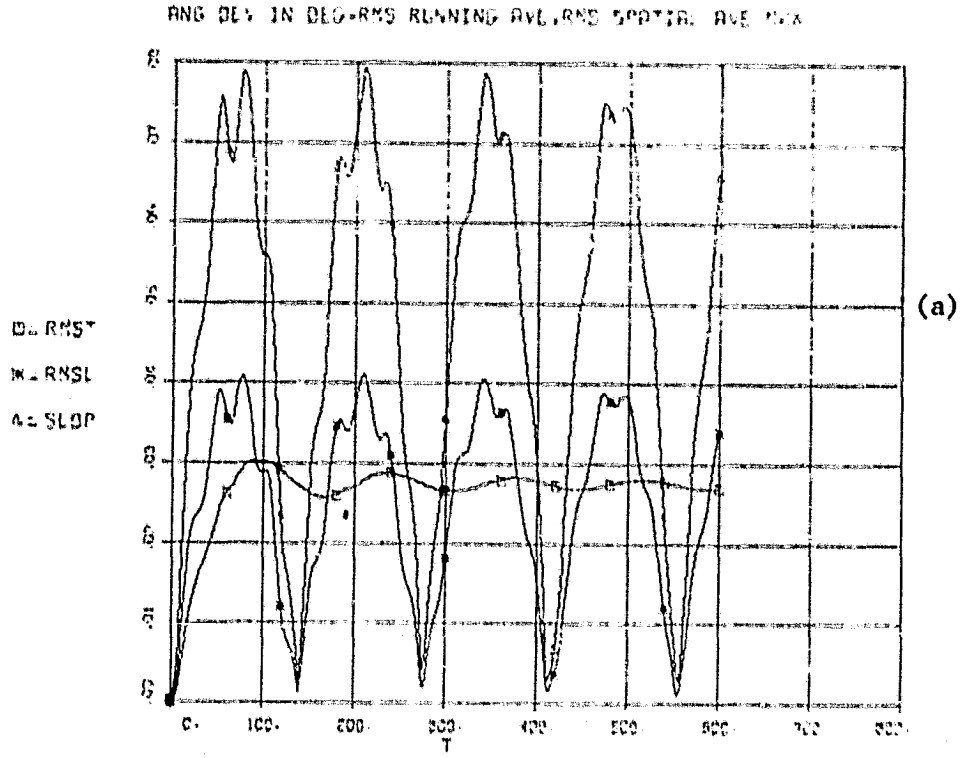

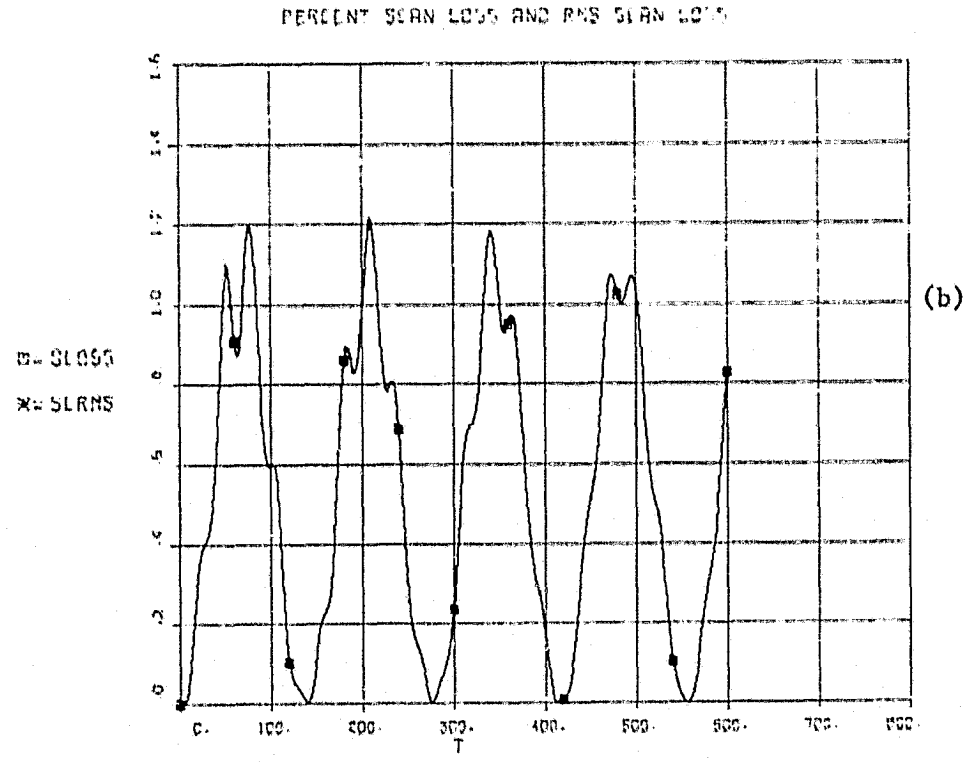

Figure 20. Surface Response to Collector Torsional Oscillation $\theta_m = 1.3°$, $\tau = 8.327 \times 10^6 \sin(.0226t)$.

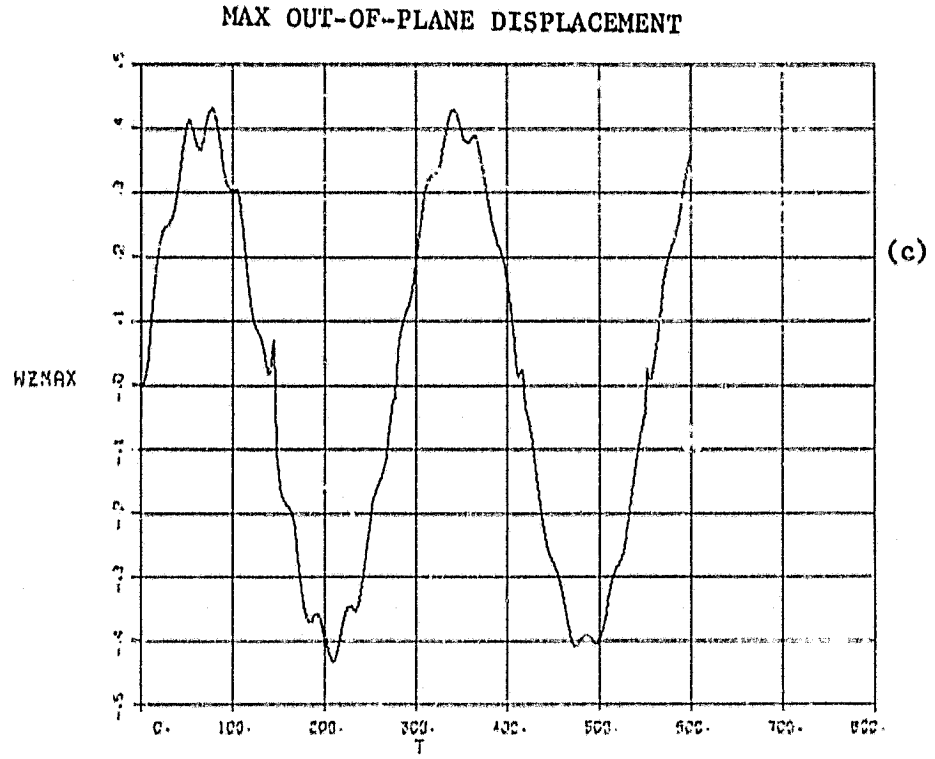

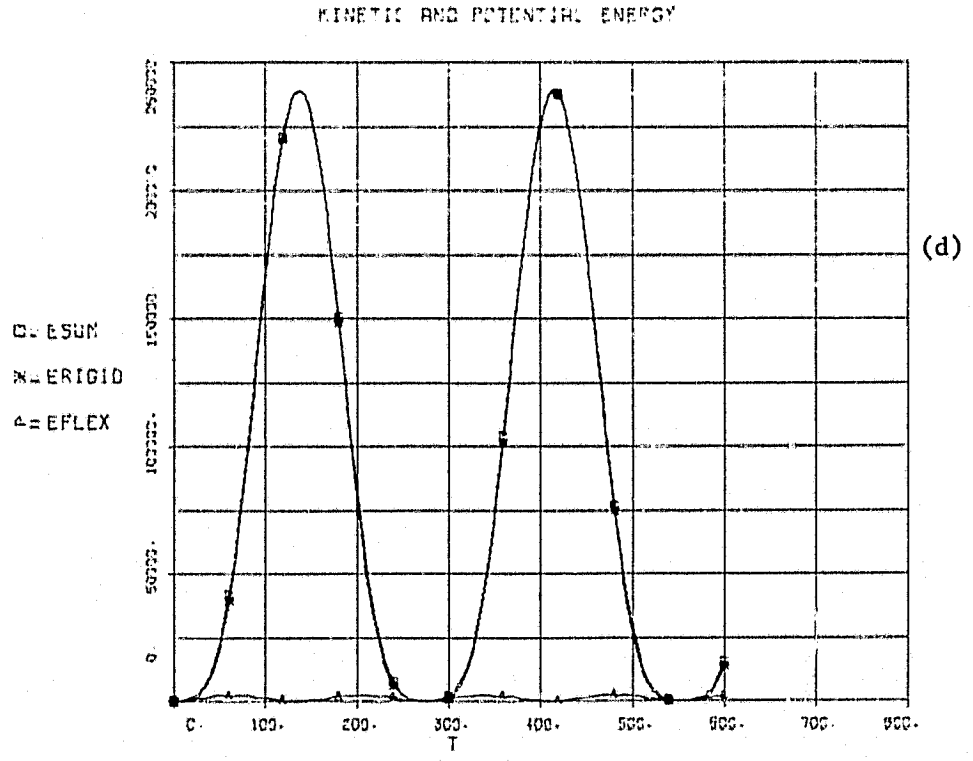

Figure 20. Surface Response to Collector Torsional Oscillation, $\theta_m = 1.3°$, $\tau = 8.327 \times 10^6 \sin(.0226t)$ (Cont.).

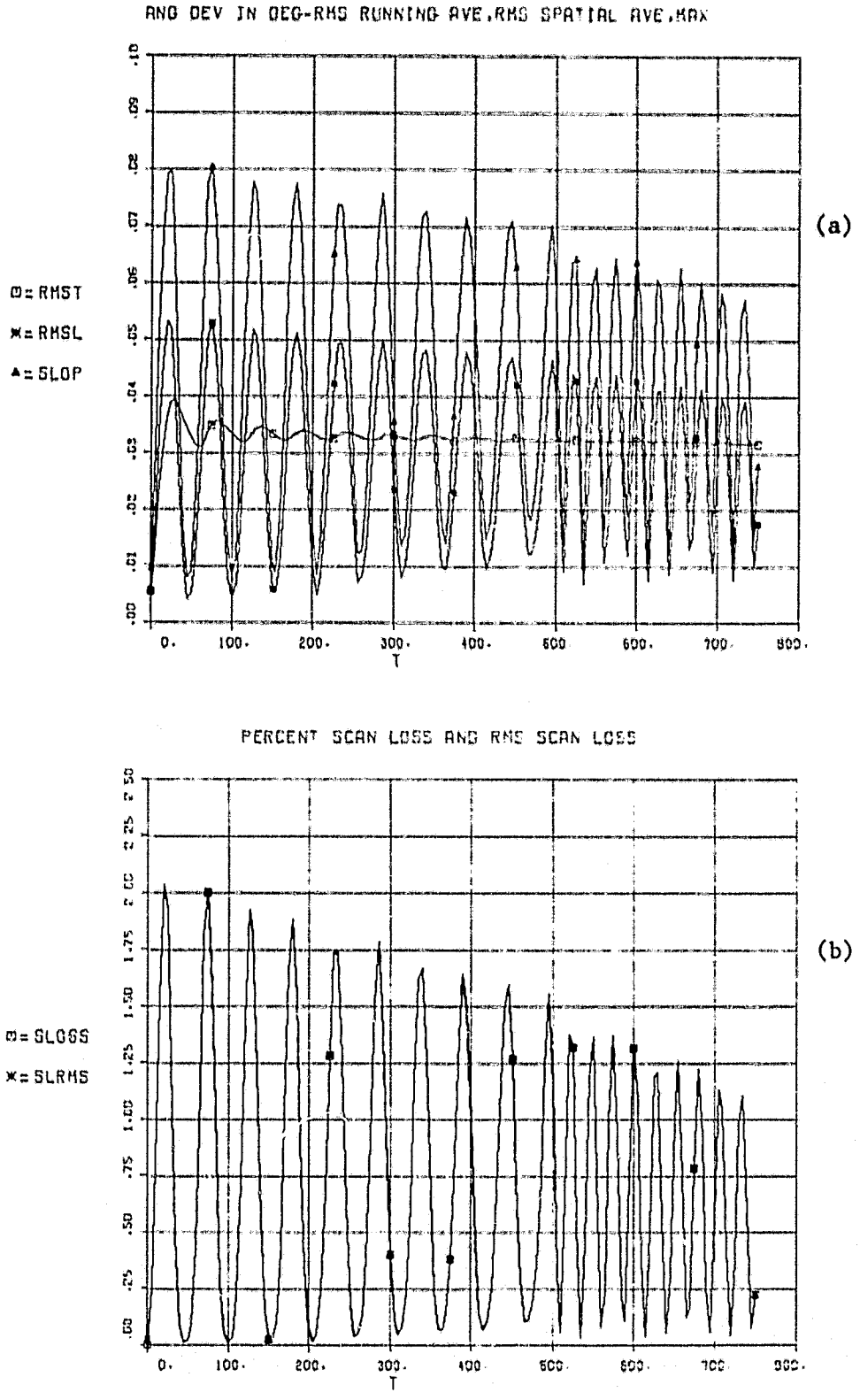

Figure 21. Surface Response to Rectangular Pulse Acceleration - Translation, F = 4000 {U(t)-U(t-500)}.

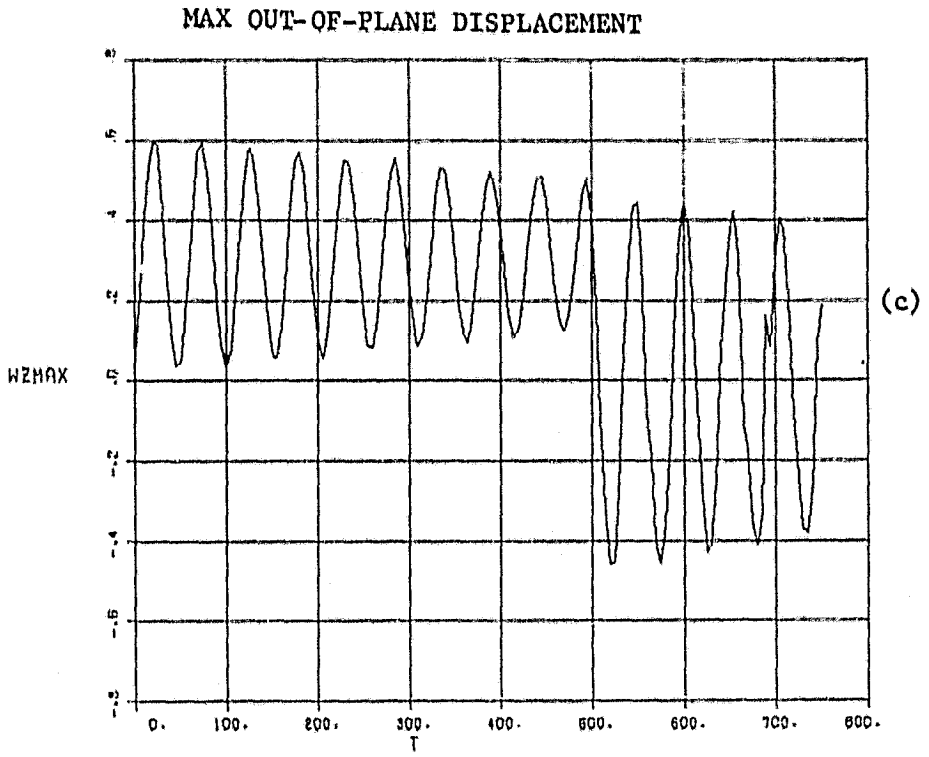

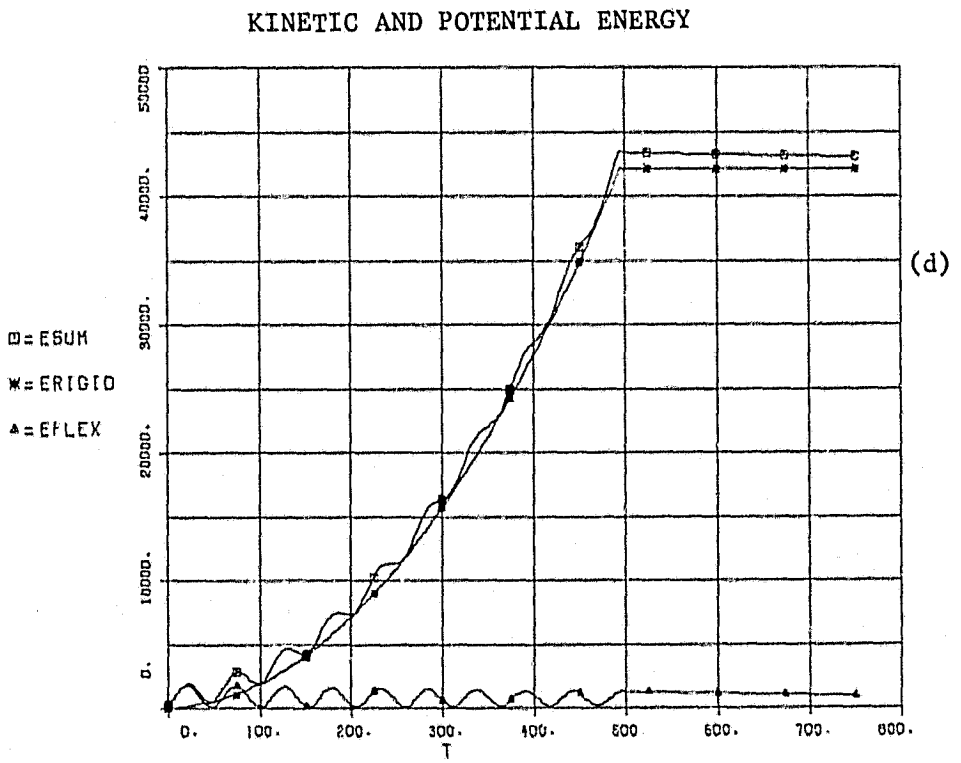

Figure 21. Surface Response to Rectangular Pulse Acceleration - Translation, F = 4000 {U(t)-U(t-500)}(Cont.).

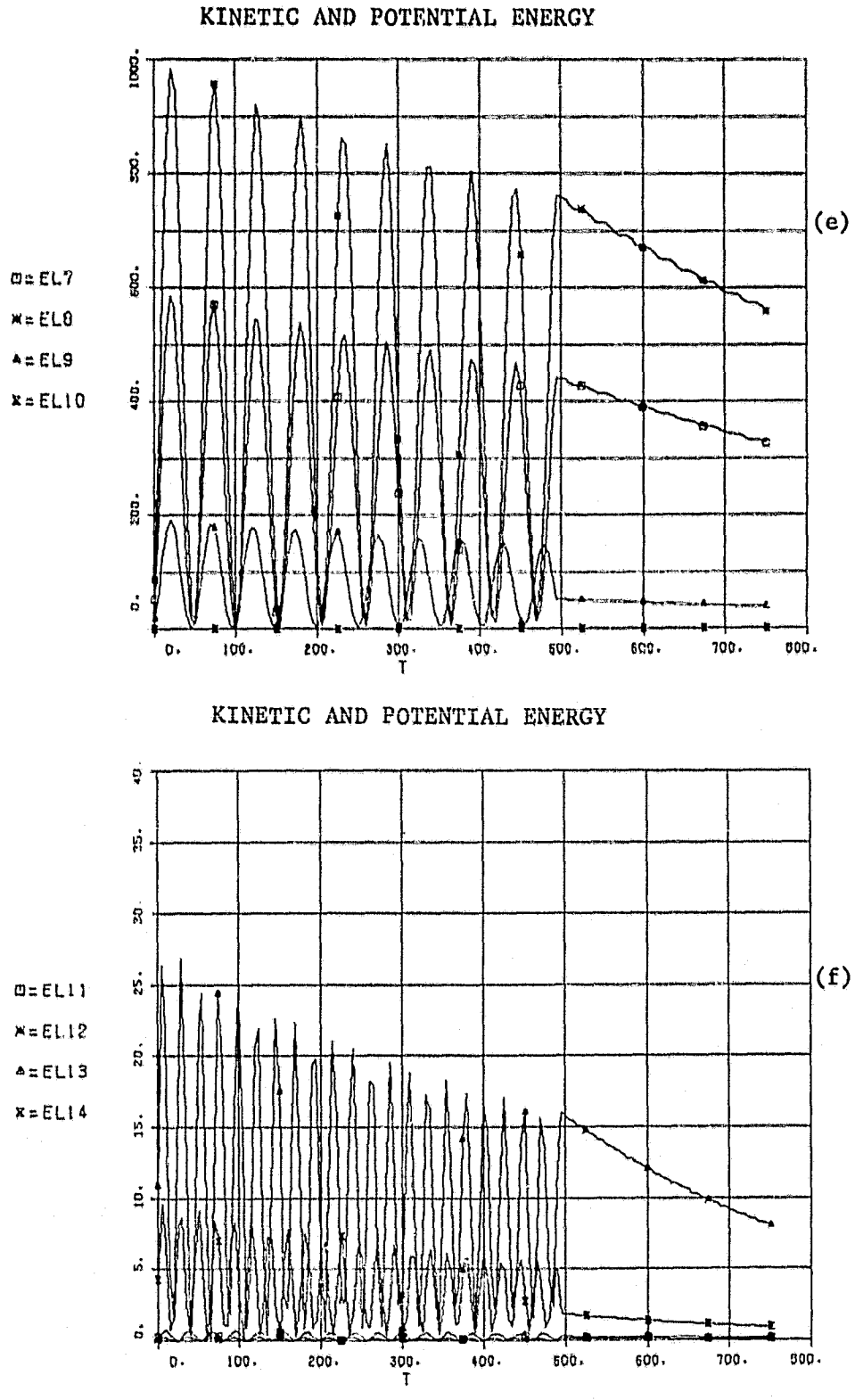

Figure 21. Surface Response to Rectangular Pulse Acceleration - Translation, F = 4000 {U(t)-U(t-500)} (Cont.).

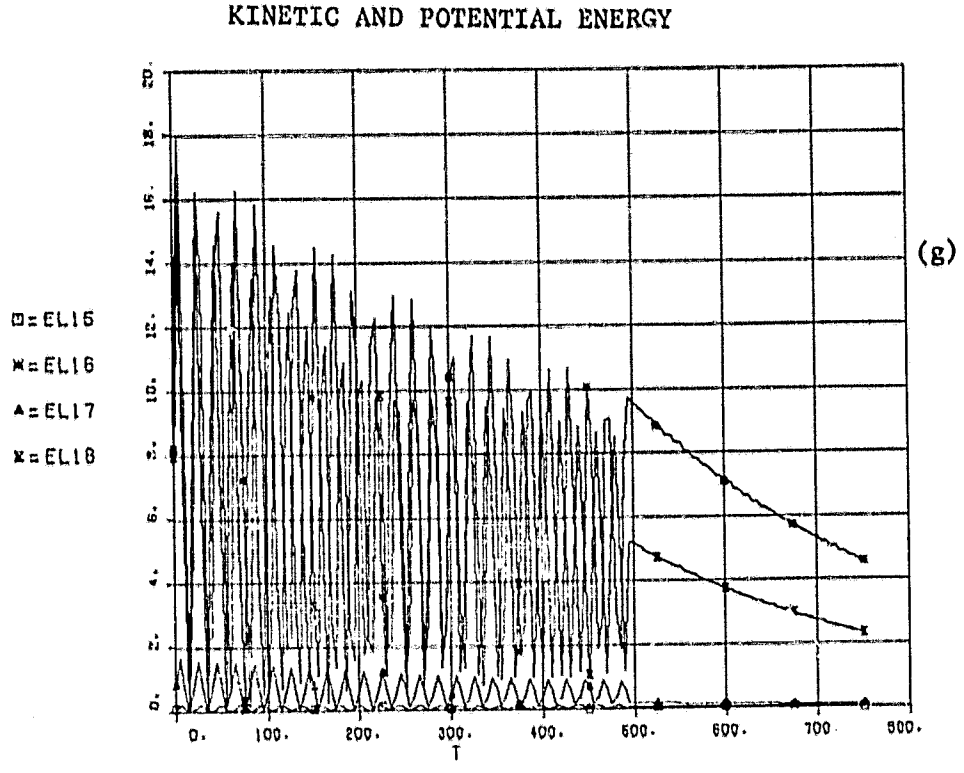

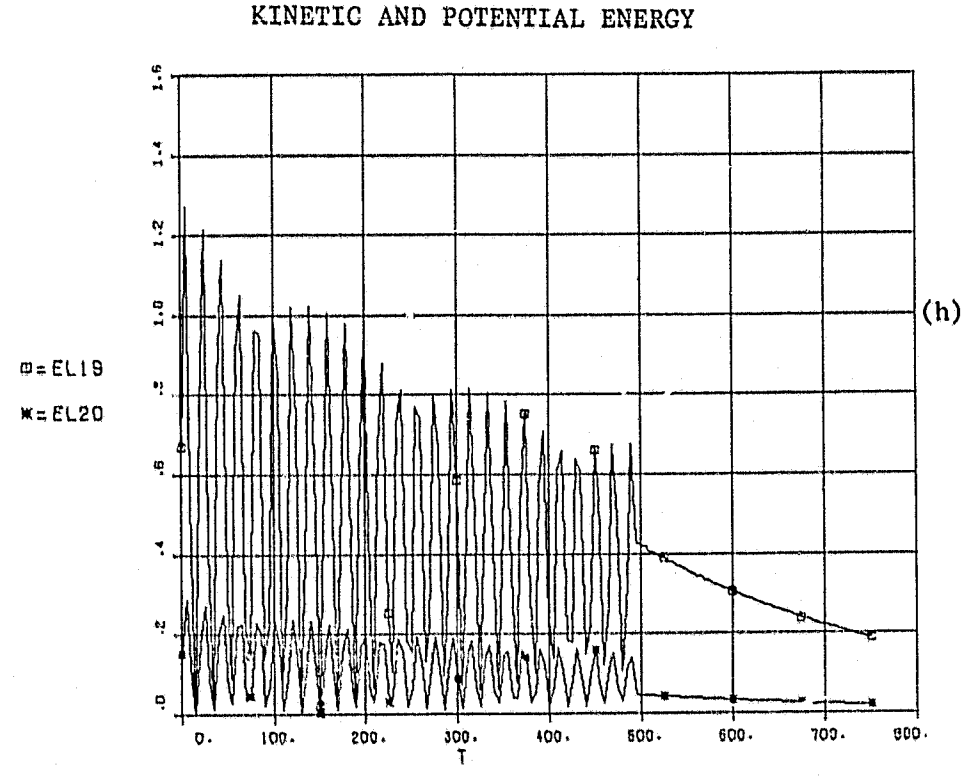

Figure 21. Surface Response to Rectangular Pulse Acceleration - Translation, F = 4000 {U(t)-U(t-500)} (Cont.).

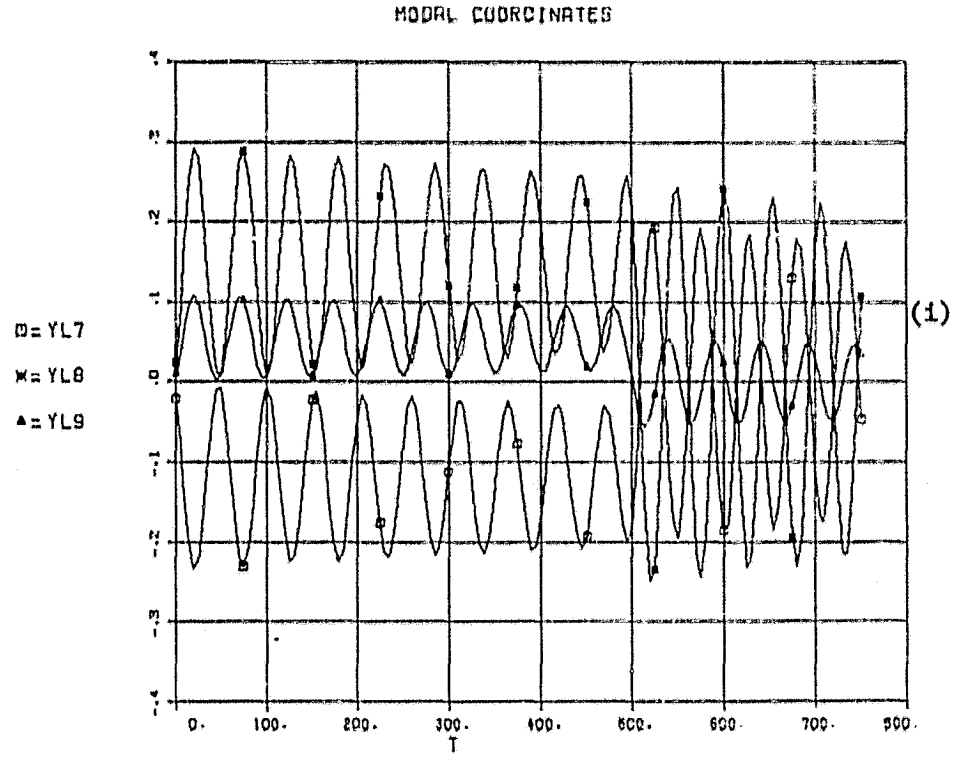

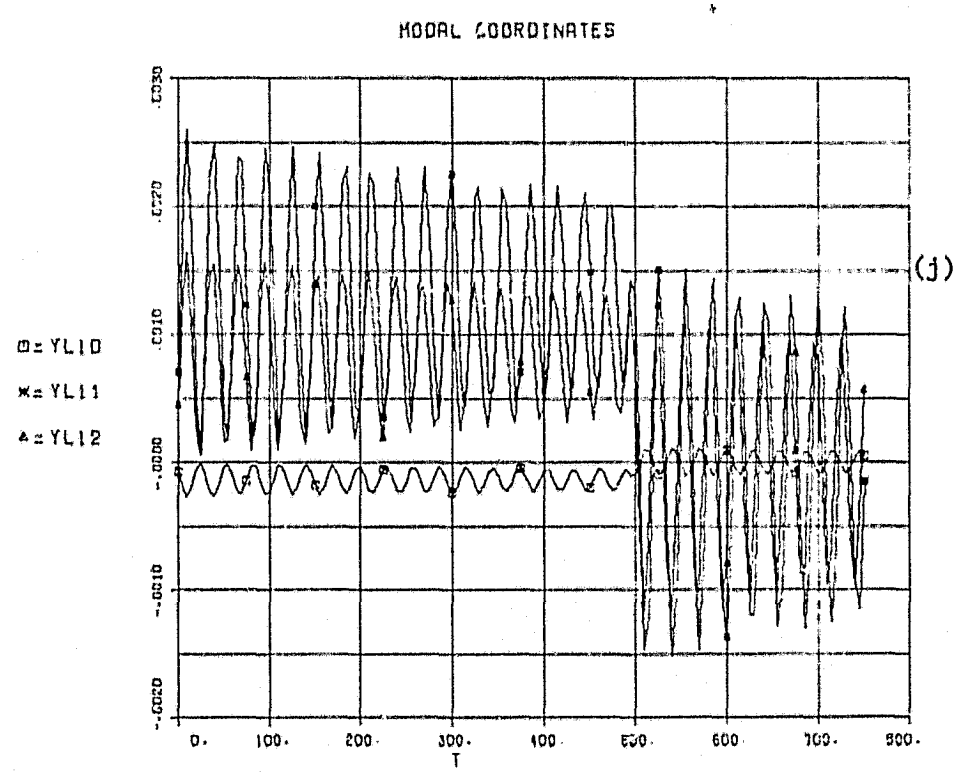

Figure 21. Surface Response to Rectangular Pulse Acceleration - Translation, F = 4000 {U(t)-U(t-500)} (Cont.).

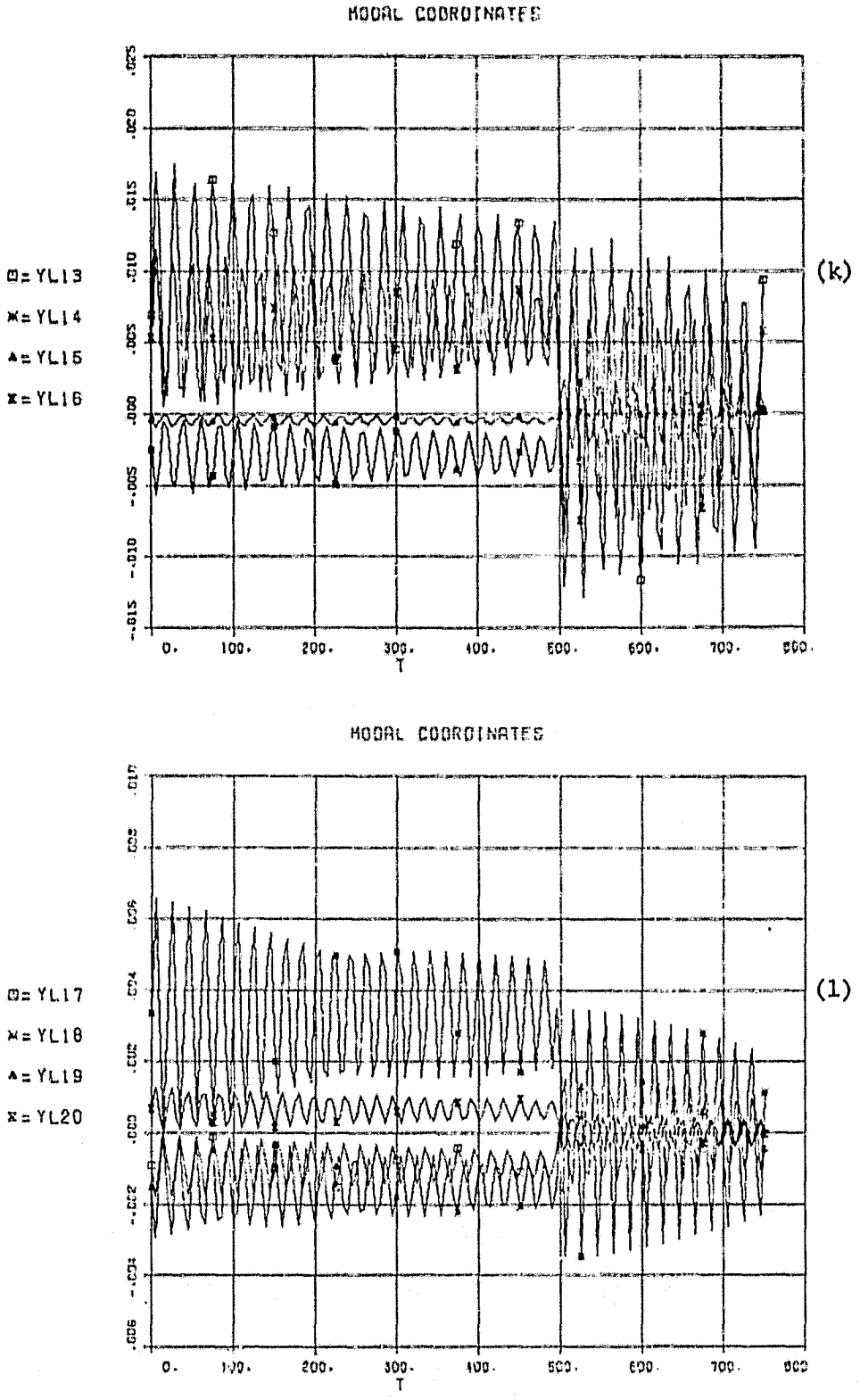

Figure 21. Surface Response to Rectangular Pulse Acceleration - Translation, F = 4000 {U(t)-U(t-500)}" (Cont.).

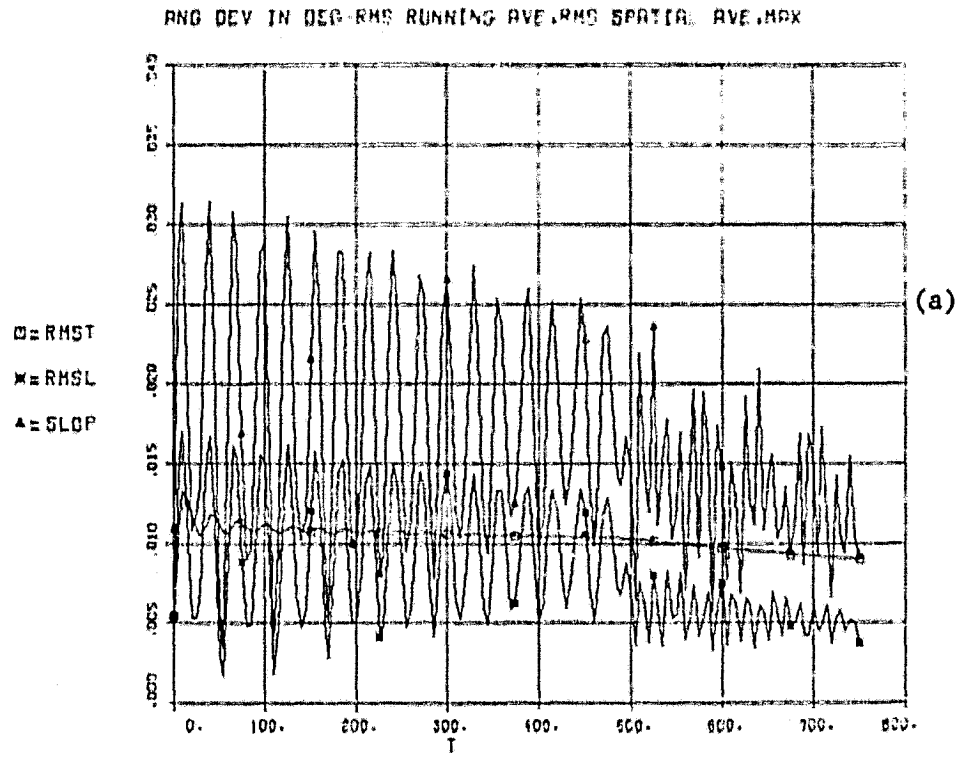

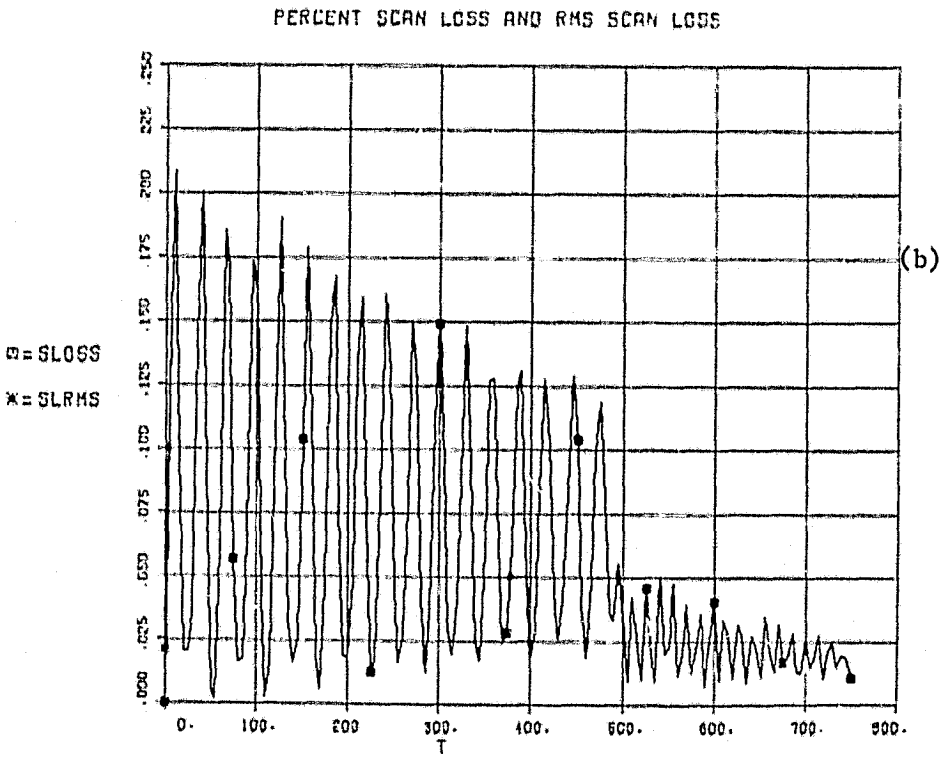

Figure 22. Surface Response to Rectangular Pulse Acceleration - Rotation, $\tau = 2 \times 10^6$ {U(t)-U(t-500)}.

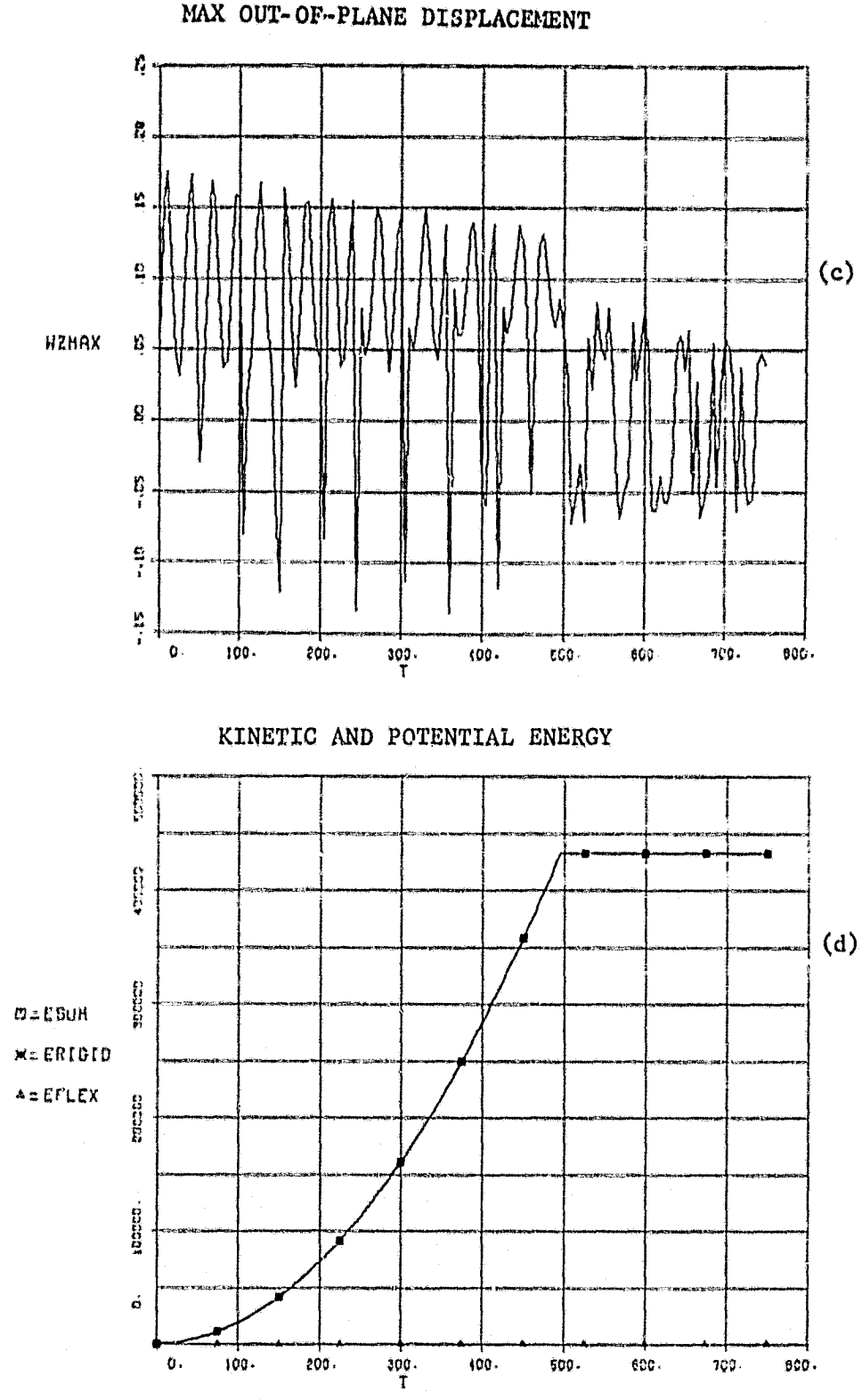

Figure 22. Surface Response to Rectangular Pulse Acceleration - Rotation, $\tau = 2 \times 10^6$ {U(t)-U(t-500)} (Cont.).

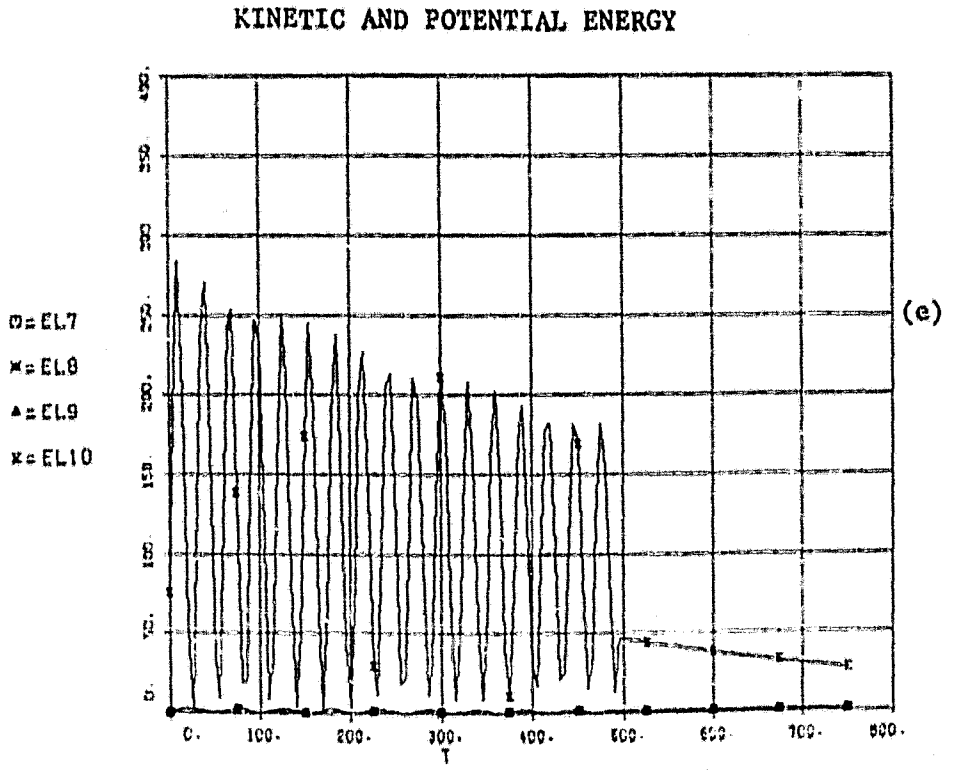

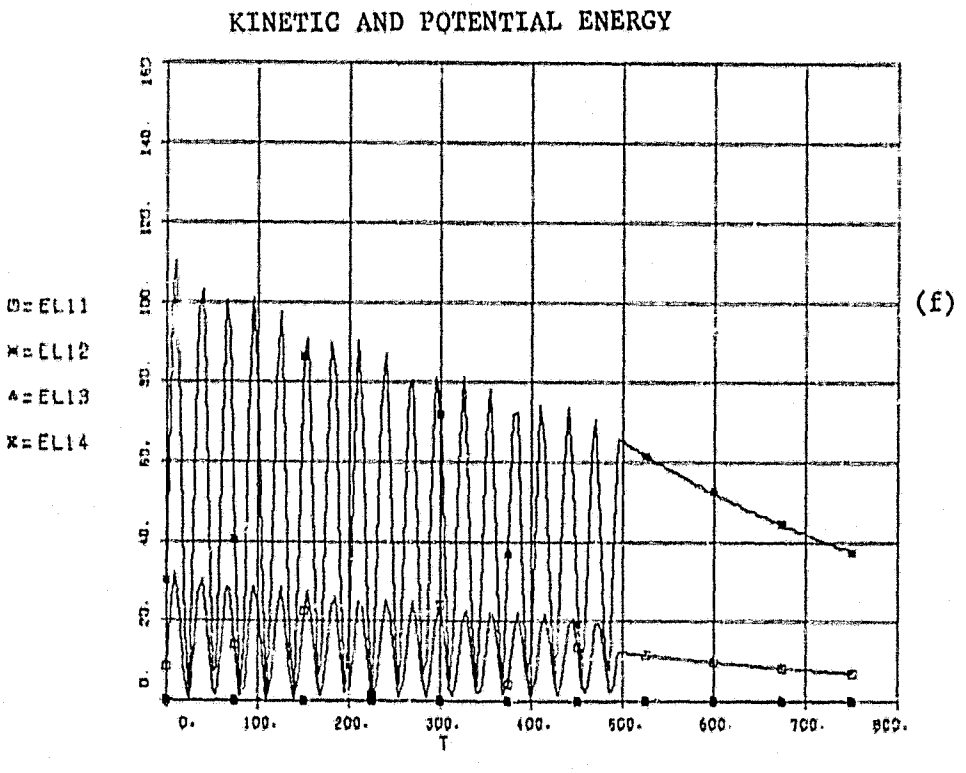

Figure 22. Surface Response to Rectangular Pulse Acceleration - Rotation, $\tau = 2 \times 10^6$ {U(t)-U(t-500)} (Cont.).

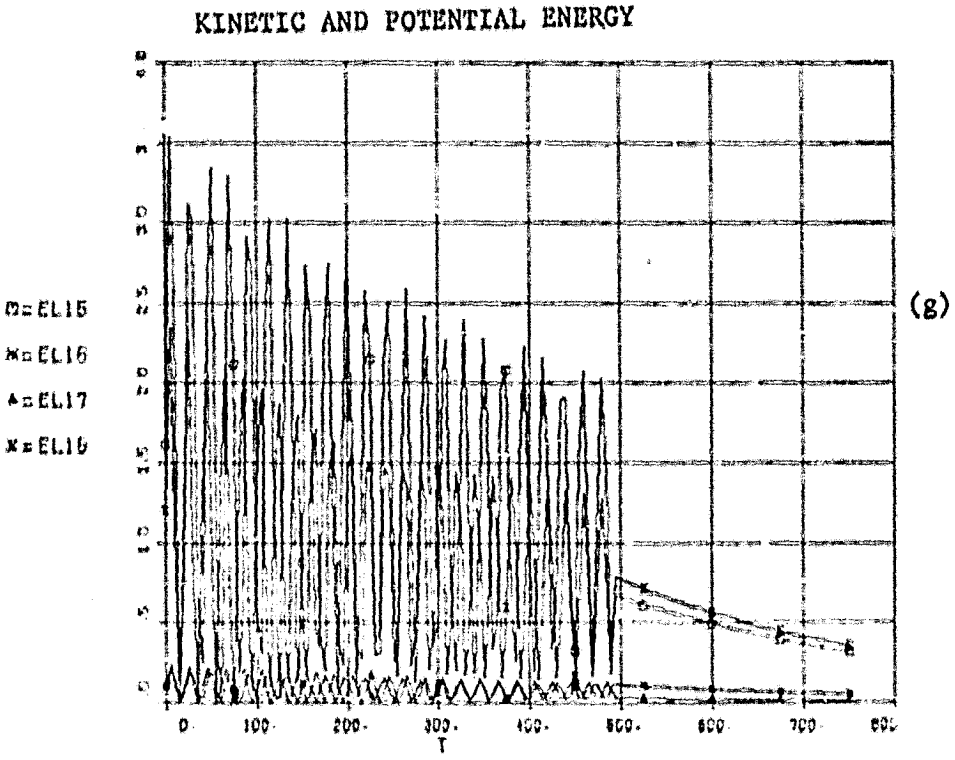

(g)

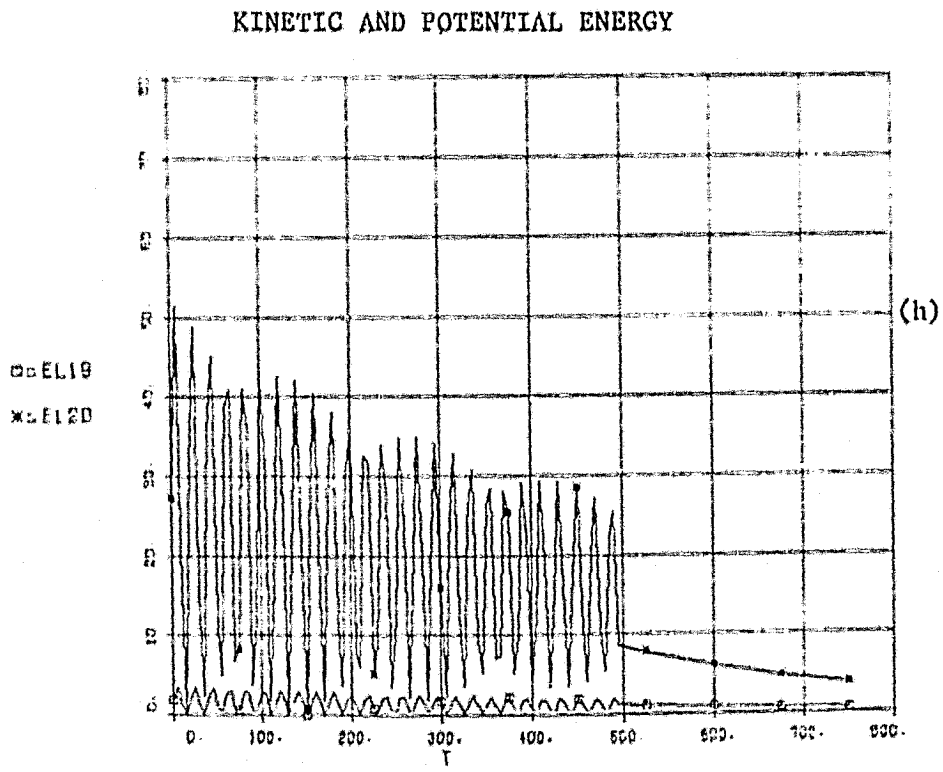

(h)

Figure 22. Surface Response to Rectangular Pulse Acceleration - Rotation, $\tau = 2 \times 10^6$ {U(t)-U(t-500)} (Cont.).

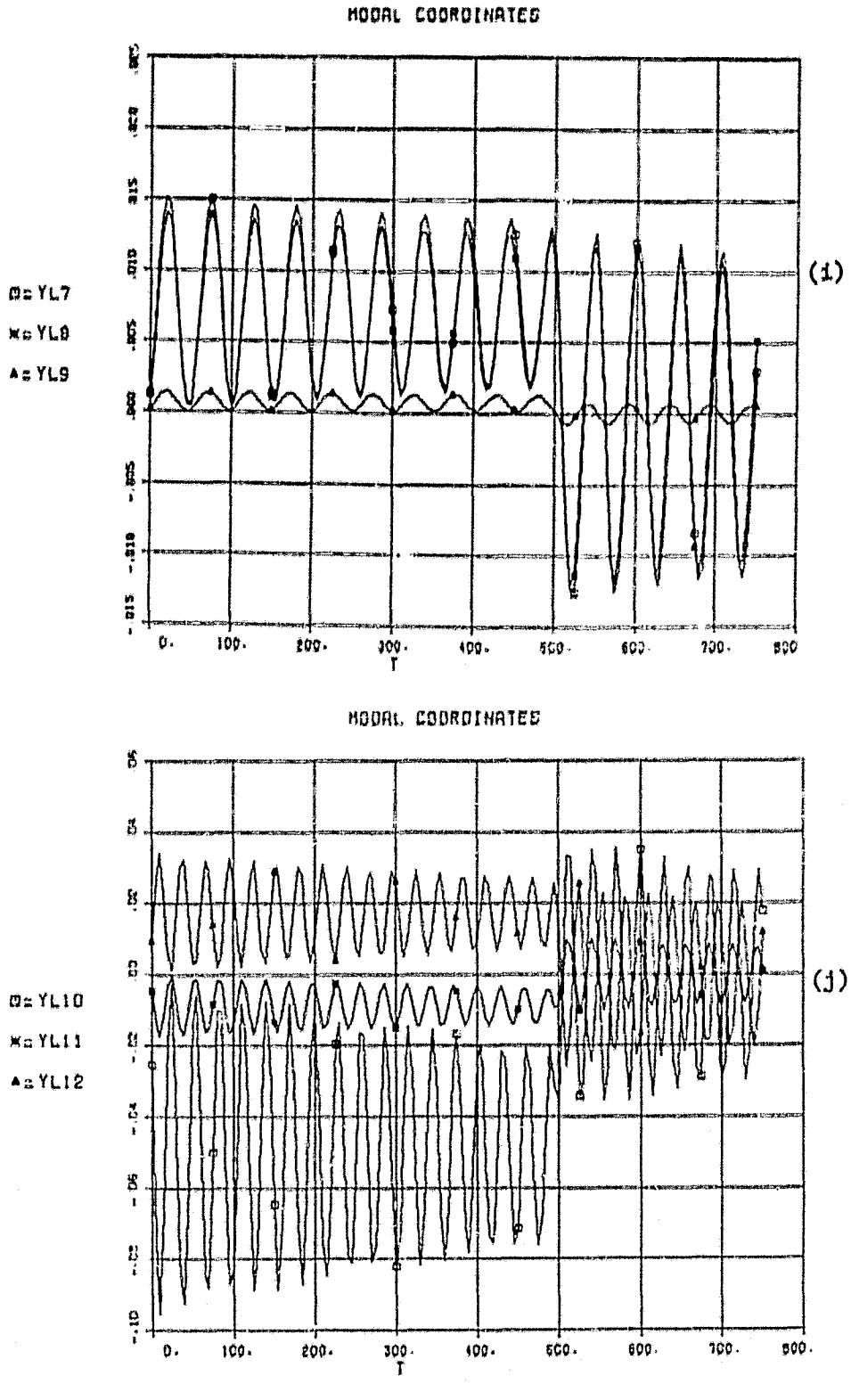

Figure 22. Surface Response to Rectangular Pulse Acceleration - Rotation, $\tau = 2 \times 10^6$ {U(t)-U(t-500)} (Cont.).

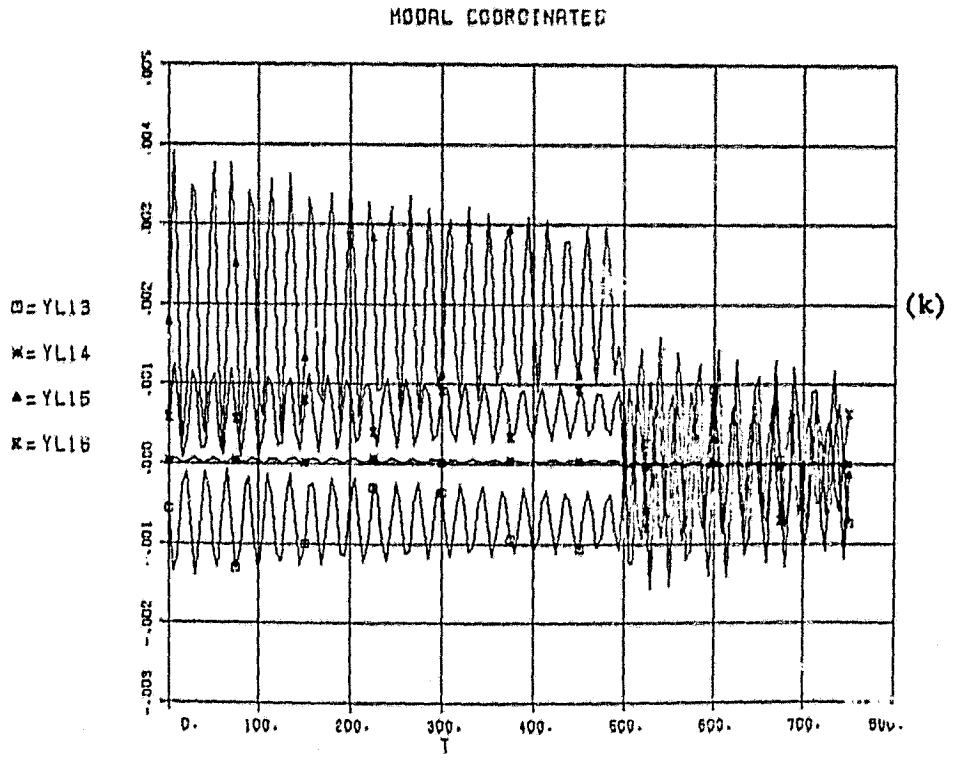

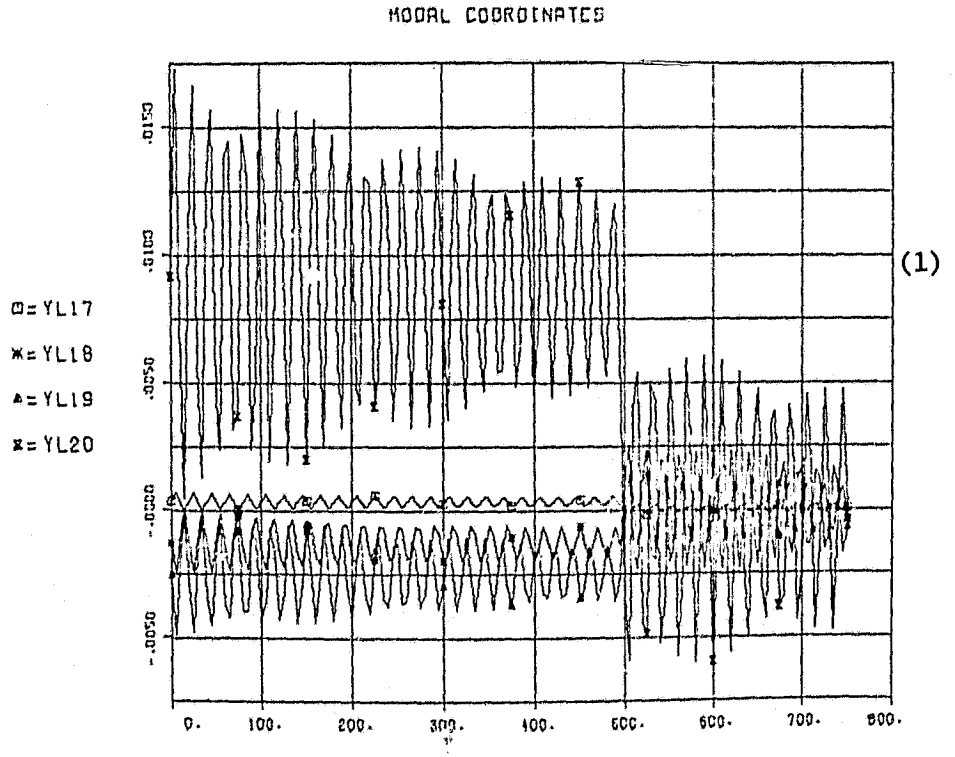

Figure 22. Surface Response to Rectangular Pulse Acceleration - Rotation, $\tau = 2 \times 10^6$ {U(t)-U(t-500)} (Cont.).

C-2

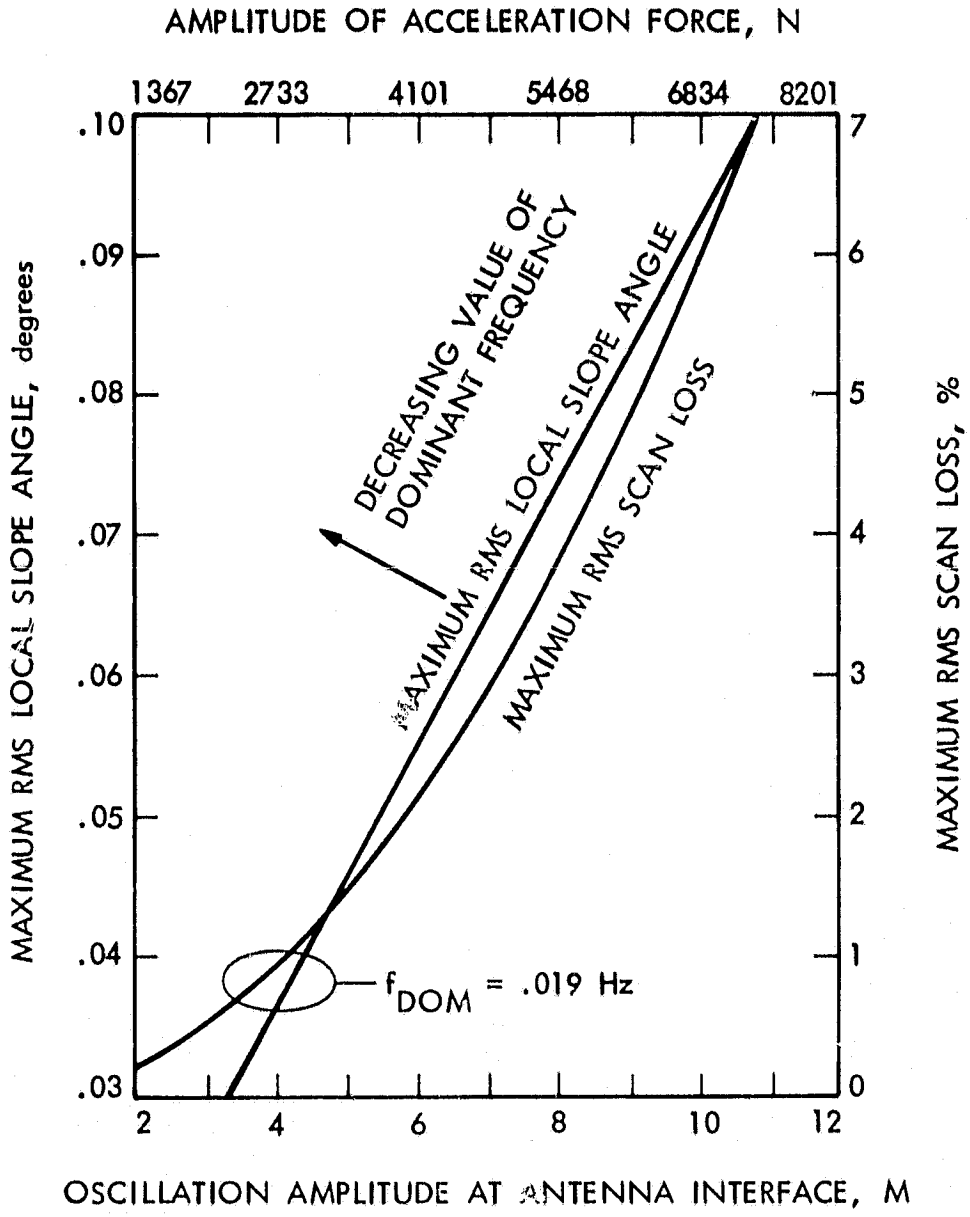

Figure 23. MPTS Surface Deformation vs. Amplitude of Collector Bending Oscillation

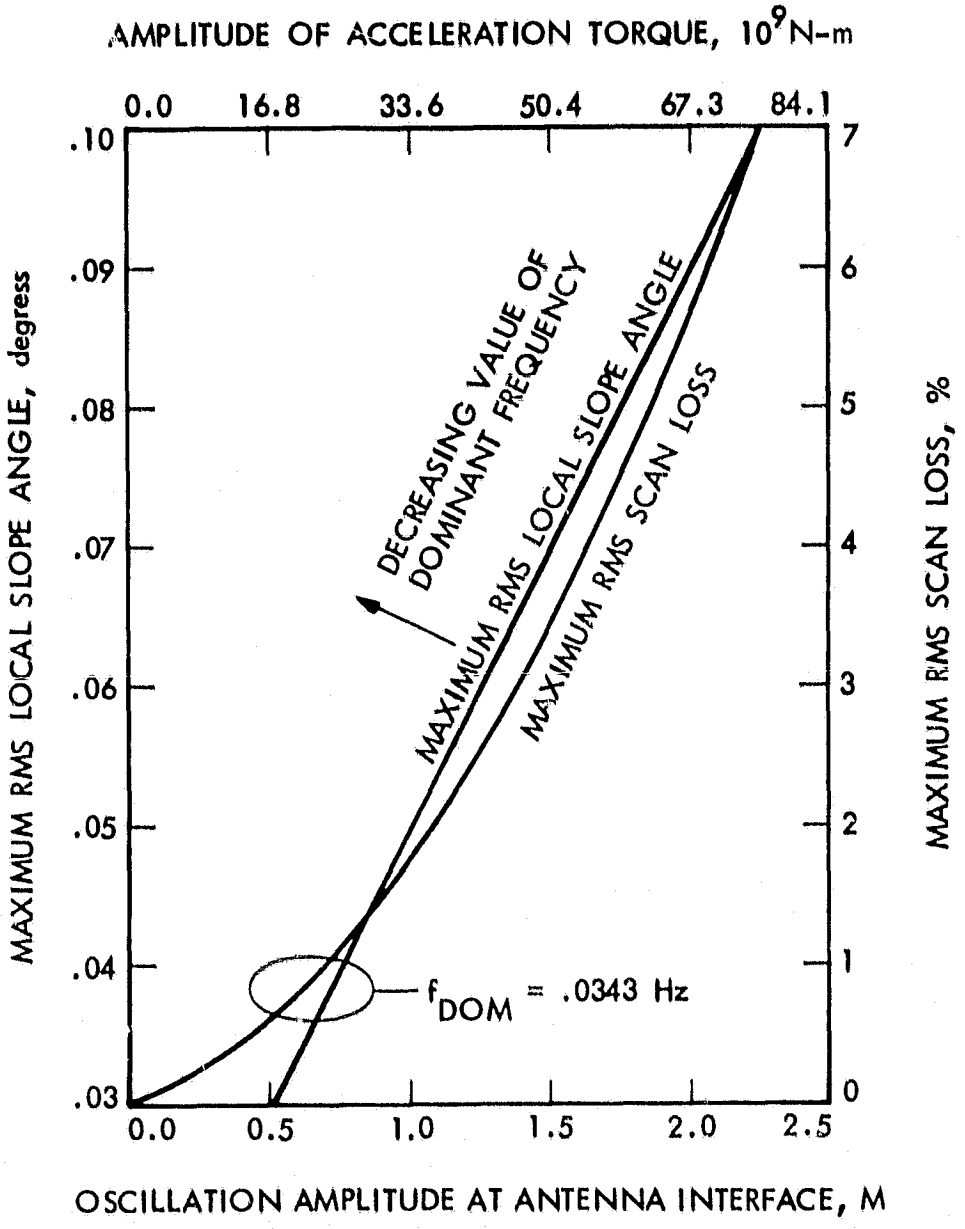

Figure 24. MPTS Surface Deformation vs. Amplitude of Collector Torsional Oscillation

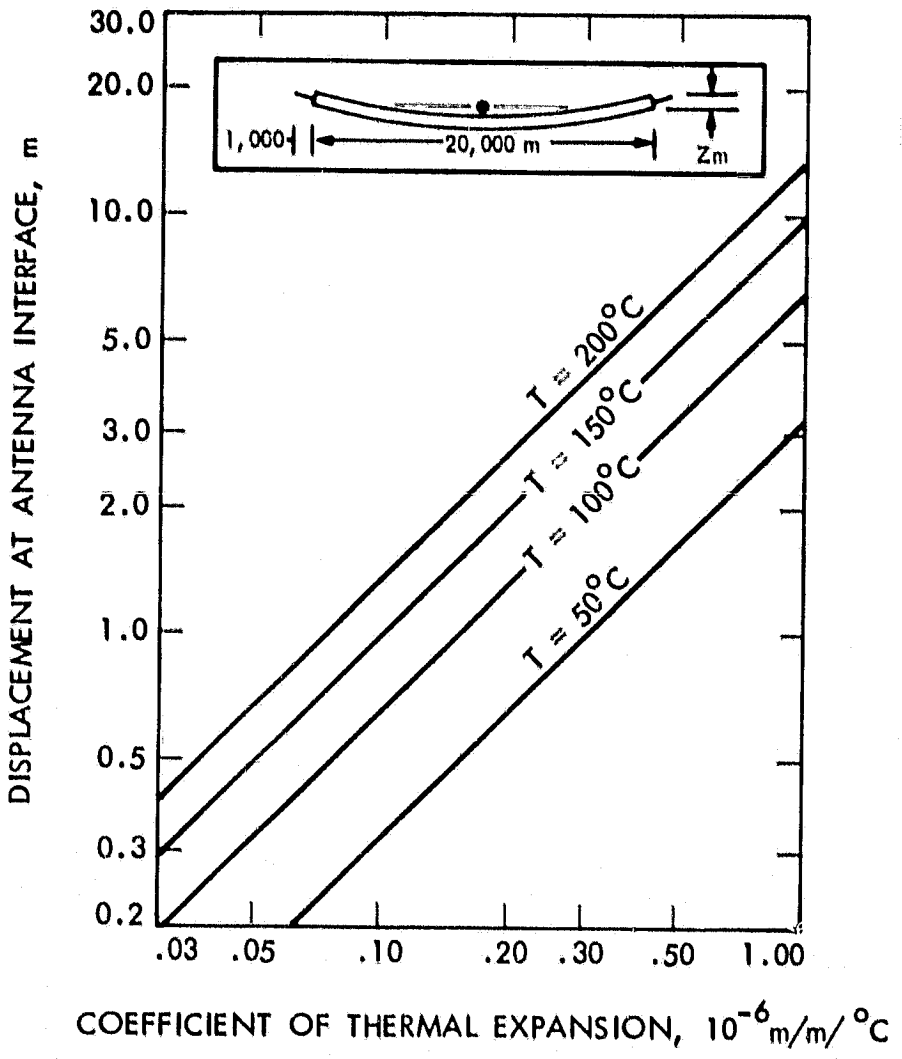

Figure 25. Collector/Antenna Boundary Displacement vs. Coefficient of Thermal Expansion of Solar Collector Structure

REFERENCES

1. S.J. Wang, "Dynamic and Control Analysis of the MPTS Antenna, I: Dynamic Model," JPL Eng. Memo 347-56, Feb. 7, 1980, (JPL internal document).

2. "Satellite Power System, Concept Development and Evaluation Program, Reference System Report," DOE/ER-0023, DOE Office of Energy Research, Washington, D.C. 20545 and the National Aeronautics and Space Administration, October 1978 (Published Jan. 1979).

3. "Achievable Flatness in a Large Microwave Power Antenna Study," Final Report, Rept. No. CASD-NAS-78-011, General Dynamics, Convair Division, August 18, 1978.

4. F.J. Stebbins, NASTRAN Program for MPTS Antenna, JSC., August 10, 1979.

5. F.J. Stebbins, "A Study of the Normal Frequencies vis-a-vis the Structural Parameters of the MPTS/SPS," NASA JSC Memo., September 1979.

APPENDIX A

Local Slope and Scan Loss Program

```
@RUN,/R SLL88,J8C26L,SOLAR,5,200/9999,,196/658     .SJW
@ASG,A SPS.
@DELETE,C 28.
@CAT,P 28.
@ASG,A 28.
@FOR,IS SUB1
      SUBROUTINE GRSTR(Y,NN)
      PARAMETER NPLOT=8
      REAL Y(20),YPLOT(NPLOT,20)
      COMMON/GRSTR1/YPLOT
C
C     HERE ONLY THE FLEX MODES ARE RECORDED.  TO INCLUDE RIGIL BODY
C     MODES, CHANGE THE RANGE OF K IN THE NEXT INSTRUCTION TO 1,20
C
      DO 20 K=7,20
   20     YPLOT(NN,K)= Y(K)
      RETURN
      ENTRY GRR
      CALL MOUT(YPLOT,8,8,20,3,3HOA=)
      DO 30 I=1,NPLOT
      WRITE(28,40) (YPLOT(I,J),J=1,10)
   30 CONTINUE
      DO 35 I=1,NPLOT
      WRITE(28,40) (YPLOT(I,J),J=11,20)
   35 CONTINUE
   40 FORMAT(1,0E12.6)
      ENDFILE 28
      REWIND 28
      RETURN
      END
@FOR,IS SUB2
      SUBROUTINE GETDAT(RX,RY,RZ,TX,TY,TZ, IPES,IGRD)
      PARAMETER NP=166,NM=20,NE=61
      REAL RX(NP),RY(NP),RZ(NP)
      REAL TX(NP,NM),TY(NP,NM),TZ(NP,NM)
      INTEGER IGRD(NP),IPE(NE,4),IPES(NE,4)
C
C     NP=NO OF NODES
C     NM=NO OF MODES
C     NE=NO OF PLATES ELEMENTS
C
C     RX,RY,RZ=COORD OF GRID POINTS
C     UX,UY,UZ=DEFORMATION OF THE GRID POINTS
C     TX,TY,TZ=EIGEN VECTOR MATRICES
C     IGRD=ARRAY OF GRID POINT ID
C     IPE=THE MATRIX OF THE PLATE ELEMENTS
C     IPES=THE SEQ NO ARRAY FOR THE GRID POINTS IN IPE
C
C     READ GRID POINT FROM SPS.MPTGP
C
```

```
      DO  10 I=1,4
      READ(5,11,ERR=10) RX(I),RY(I),RZ(I)
   10 CONTINUE
      DO 20 I=1,NP
      READ(5,11) IGRD(I),RX(I),RY(1),RZ(I)
   11 FORMAT(I5,3F15.4)
   20 CONTINUE
C
C     READ EIGENVECTORS FROM SPS.MPTEVT
C
      DO 40 K=1,NM
      DO 30 I=1,3
      READ(5,31,ERR=30) TX(I,K),TY(I,K),TZ(I,K)
   30 CONTINUE
   31 FORMAT(8X,E12.7,2E15.7)
      DO 40 I=1,NP
      READ(5,31) TX(I,K),TY(I,K),TZ(I,K)
   40 CONTINUE
C
C     READ PLATE ELEMENTS FROM CARDS
C
      READ(5,51) ((IPE(I,J),J=1,4),I=1,NE)
   51 FORMAT(16I5)
C
C     TEST
C
      WRITE(6,51) ((IPE(I,J),J=1,4),I=1,NE)
C
C     DETERMINE SEQ NO FOR IPE
C
      DO 60 I=1,NE
      DO 60 K=1,NP
      IPES(I,1)=IPE(I,1)
      DO 60 J=2,4
      IF(IPE(I,J).EQ.IGRD(K)) IPES(I,J)=K
   60 CONTINUE
C
C     TEST
C
      WRITE(6,51) ((IPES(I,J),J=1,4),I=1,NE)
      RETURN
      END
@FOR,IS SUB3
      SUBROUTINE MSSE(IPES,NE,UX,UY,UZ,ICNT,RMSTP,C1,ABC1,SLOP,ISLOP,
     1                RMSL,RMST,SLOSS,SLRMS)
C
C     THIS SUBR COMPUTES THE LOCAL SLOPES OR THE DEVIATIONS OF LOCAL
C     NORMAT FROM ITS UNDISTURBED NORMAL VALUE.  SINCE THE ANGLES ARE
C     SMALL, DOUBLE PRECISION FOR SOME VARIABLES IS REQURED
C
```

```
C       IPES=THE SEQ NO ARRAY FOR THE GRID POINTS OF THE PLATE ELEMENTS
C       NE=NO OF PLATE ELEMENTS IN THIS COMPUTATION
C       UX,UY,UZ=THE INSTANTANUOUS COORDINATE VECTORS OF THE GRIDS
C       SLOP=MAX SLOPE IN THE INTERVAL
C       ISLOP=PLATE ELEMENT NO OF MAX SLOPE
C       RMSL=SPATIAL AVERAGE, RMS SLOPE ERROR, DEGREE
C       RMST=RUNNING AVERAGE, RMS SLOPE ERROR, DEGREE
        DIMENSION IPES( 61,4),UX(166),UY(166),UZ(166)
        DOUBLE PRECISION A,B,C,CC,ABC
        INTEGER H
C
C       PDL=PI*DE/LAMBDA*(PI/180.), THETA IN DEGREE
C       DE=10.39 METERS
C       LAMDA=.1224 METER       (FREQ=2.45 GHZ)
C       SLOSS IS THE PERCENT SCAN LOSS OF THE ARRAY
C       SLRMS IS THE SCAN LOSS COMPUTED BASED ON RMS SCAN ANGLE
C
        PDL=4.654375
        SLOSS=0.
C
        SLOP=0.
        RMSL=0.
        DO 80 IE=1,NE
        H=IPES(IE,2)
        J=IPES(IE,3)
        K=IPES(IE,4)
COMMENT H, J, K ARE THE 1ST, 2ND, 3RD POINT THAT DEFINES PLATE ELEM IE
        A1=UX(J)-UX(H)
        A2=UY(J)-UY(H)
        A3=UZ(J)-UZ(H)
        B1=UX(K)-UX(H)
        B2=UY(K)-UY(H)
        B3=UZ(K)-UZ(H)
        A=-A3*B2+A2*B3
        B=A3*B1-A1*B3
        C=-A2*B1+A1*B2
        CC=DABS(C)
        ABC=DSQRT(A*A+B*B+C*C)
C
C       COMPUTE LOCAL SLOPE ANGLE IN DEGREES
C
        TEMP=SNGL((DACOS(CC/ABC))*57.295780)
        IF(TEMP.LE.SLOP) GO TO 70
        SLOP=TEMP
        ISLOP=IPES(IE,1)
        C1=SNGL(C)
        ABC1=SNGL(ABC)
   70 CONTINUE
```

```
C
C       COMPUTE ELEMENT PATTERN, RECTANGULAR APERTURE AND UNIFORM
C       ILLUNINATION
C
        IF(TEMP.EQ.0) GOTO 80
        ANG=PDL*TEMP
        TEMP1=SIN(ANG)/ANG
        SLOSS=SLOSS+TEMP1*TEMP1
        RMSL=RMSL+TEMP*TEMP
   80   CONTINUE
        SLOSS=(1.-SLOSS/NE)*100.
        IF(ICNT.EQ.0) SLOSS=0.
        RMSL=RMSL/NE
        RMST=RMSTP*RMSTP*ICNT+RMSL
COMMENT RMSL IS THE RMS SLOPE - SPATIAL AVERAGE, RMST IS THE TIME AVE
        ICNTP=ICNT+1
C
        RMST=SQRT(RMST/ICNTP)
        RMSL=SQRT(RMSL)
C
C       COMPUTE RMS SCAN LOSS
C
        ANG=PDL*RMSL
        TEMP1=SIN(ANG)/ANG
        SLRMS=(1.0-TEMP1*TEMP1)*100.
        RETURN
        END
@ASG,A CSSL*TRAN.
@XQT,G CSSL*TRAN.CSSL
PROGRAM SLOPE OF 1000-METER SPS ANTENNA
INITIAL
        ARRAY W(20),Y(20),YU(20),YP(20),YUP(20),Z(20),WO(20),RHO(20),E(20)
        ARRAY U(20),BETA(20),C8(20),C1(20),S1(20),TPLOT(8)
        ARRAY RX(166),RY(166),RZ(166),TX(166,20),TY(166,20),TZ(166,20)
        ARRAY UX(166),UY(166),UZ(166),UU(3),VV(3),WW(3)
        ARRAY WX(166),WY(166),WZ(166)
        ARRAY MS(20),PF(20)
        INTEGER KK,NN,NPLOT,IP,NE,ICNT
        INTEGER IGRD(166),IPES(61,4),ISLOP,IPMAX
        DT=2.5
        TF=750.
COMMENT THE MAX NO OF PLATE ELEMENTS IS 61
        NE=61
COMMENT APPLIED FORCE IN NEWTON
        FORCE=854.3
CONSTANT NPLOT=8
CONSTANT W=0.,0.,0.,0.,0.,0.,.1186656,.1191997,.1231927,.2155254, ...
```

```
          .2170462,.2188395,.2702198,.2869165,.2910554,.2960338, ...
          .3132678,.3175584,.3233108,.3248956
CONSTANT MS=3180000.,3900000.,14800000.,2680000.,7180000., ...
            1780000.,1520000.,1610000.,2150000.,1340000., ...
            4490000.,3980000.,2400000.,7250000.,5440000., ...
            3000000.,10200000.,7120000.,2810000.,3260000.
CONSTANT TPLOT=100.,200.,300.,400.,500.,600.,700.,800.
       DO L4 KK=1,20
          YD(KK)=0.
       Y(KK)=0.
       Z(KK)=.005
L4..CONTINUE
       DO L6 KK=1,20
          CB(KK)=SQRT(1.0 - Z(KK)*Z(KK))
          BETA(KK)= Z(KK)/CB(KK)
          WO(KK)= W(KK)*CB(KK)
          C1(KK)= COS(WO(KK)*DT)
          S1(KK)= SIN(WO(KK)*DT)
         RHO(KK)= EXP(-Z(KK)*W(KK)*DT)
L6..CONTINUE
       NN=1
       SLOP=0.
       ISLOP=0
       RMSL=0.
       RMST=0.
       C=0.
       ABC=0.
       ICNT=0
       SLOSS=0.
       SLRMS=0.
COMMENT CALL GETDAT TO GET DATA FROM SPS FILES AND FROM CAPOS
       CALL GETDAT(RX,RY,RZ,TX,TY,TZ,IPES,IGRD)
COMMENT INITIALIZE DISPLACMENT
       DO L10 IP=1,166
       WX(IP)=0.
       WY(IP)=0.
       WZ(IP)=0.
L10..CONTINUE
       DO L15 KK=1,20
       PF(KK)=(TZ(136,KK)+TZ(53,KK)+.5*(TZ(140,KK)+TZ(156,KK)+ ...
          TZ(58,KK)+TZ(77,KK)))/MS(KK)
L15..CONTINUE
END
DYNAMIC
CINTERVAL CI=2.5
       IF(T.GT.TF)GO TO FIN
       IF(DT.NE.CI) GO TO FIN
       DO L16 IP=1,166
       WX(IP)=0.
       WY(IP)=0.
       WZ(IP)=0.
L16..CONTINUE
       DO L18 KK=1,20
       U(KK)=PF(KK)*FORCE*COS(.00675*T)
```

```
L18..CONTINUE
      DO L20 KK=1,20
      YP(KK)=Y(KK)
      YDP(KK)= YD(KK)
L20..CONTINUE
      DO L24 KK=1,20
      IF(KK.GT.6) GO TO L23
COMMENT COMPUTE RIGID BODY MODES
      Y(KK)=YP(KK) + YDP(KK)*DT + (U(KK)*DT*DT/2.0)
      YD(KK) = YDP(KK) + U(KK)*DT
      GO TO L24
L23.. CONTINUE
COMMENT COMPUTE FLEXIBLE MODES
      Y(KK)=RHO(KK)*(C1(KK)+ BETA(KK)*S1(KK))*YP(KK)+ ...
            RHO(KK)*S1(KK)*YDP(KK)/WO(KK)+              ...
            U(KK)*(1.0-RHO(KK)*(C1(KK)+BETA(KK)*S1(KK)))/(W(KK)*W(KK))
      YD(KK)=-RHO(KK)*W(KK)*(S1(KK)/CB(KK))*YP(KK)  + ...
               RHO(KK)*(C1(KK)-BETA(KK)*S1(KK))* YDP(KK)+ ...
               U(KK)*RHO(KK)*S1(KK)/(W(KK)*CB(KK))
L24.. CONTINUE
COMMENT COMPUTE GRID POINT DISPLACEMENT
COMMENT *****
COMMENT TO INCLUDE RIGIDBODY MOTION KK IN L25 SHOULD START AT 1
COMMENT *****
      DO L25 KK=7,20
      DO L25 IP=1,166
      WX(IP)=WX(IP)+Y(KK)*TX(IP,KK)
      WY(IP)=WY(IP)+Y(KK)*TY(IP,KK)
      WZ(IP)=WZ(IP)+Y(KK)*TZ(IP,KK)
L25..CONTINUE
COMMENT GRID POINT POSITION
      WMAX=0.
      TEMP=0.
      IPMAX=0
      DO L26 IP=1,166
      UX(IP)=RX(IP)+WX(IP)
      UY(IP)=RY(IP)+WY(IP)
      UZ(IP)=RZ(IP)+WZ(IP)
COMMENT COMPUTE MAX OUT-OF-PLAN DISPLACEMENT
      ABSWZ=ABS(WZ(IP))
      IF(TEMP.GE.ABSWZ) GO TO L26
      WZMAX=WZ(IP)
      TEMP=ABS(WZMAX)
      IPMAX=IGRD(IP)
L26..CONTINUE
COMMENT COMPUTE SPATIAL AVE RMS SLOPE ERROR AND RUNNING AVE RMS SLOPE ERROR
      RMSTP=RMST
      CALL MSSE(IPES,NE,UX,UY,UZ,ICNT,RMSTP,C,ABC,SLOP,ISLOP,RMSL, ...
                RMST,SLOSS,SLRMS)
      ICNT=ICNT+1
      IF(NN.GT.NPLOT) GO TO L30
      IF(T.LT.TPLOT(NN)) GO TO L30
      CALL GRSTR(Y,NN)
            NN=NN+1
```

```
L30..CONTINUE
      ERIGID=0.
      EFLEX=0.
      DO L50 KK=1,20
      E(KK) = YD(KK)*YD(KK) + W(KK)*W(KK)*Y(KK)*Y(KK)
      E(KK)=.5*MS(KK)*E(KK)
L50..CONTINUE
      DO L55 KK=1,6
      ERIGID=ERIGID+E(KK)
L55.. CONTINUE
      DO L60 KK=7,20
      EFLEX=EFLEX+E(KK)
L60.. CONTINUE
      ESUM=ERIGID+EFLEX
      YL1=Y(1) $ YL2=Y(2) $ YL3=Y(3) $ YL4=Y(4) $ YL5=Y(5)
      YL6=Y(6) $ YL7=Y(7) $ YL8=Y(8) $ YL9=Y(9) $ YL10=Y(10)
      YL11=Y(11) $ YL12=Y(12) $ YL13=Y(13) $ YL14=Y(14) $ YL15=Y(15)
      YL16=Y(16) $ YL17=Y(17) $ YL18=Y(18) $ YL19=Y(19) $ YL20=Y(20)
      EL1=E(1) $ EL2=E(2) $ EL3=E(3) $ EL4=E(4) $ EL5=E(5)
      EL6=E(6) $ EL7=E(7) $ EL8=E(8) $ EL9=E(9) $ EL10=E(10)
      EL11=E(11) $ EL12=E(12) $ EL13=E(13) $ EL14=E(14) $ EL15=E(15)
      EL16=E(16) $ EL17=E(17) $ EL18=E(18) $ EL19=E(19) $ EL20=E(20)
OUTPUT YL1,YL2,YL3,YL4,YL5,YL6,YL7,YL8,YL9,YL10,YL11,YL12,YL13, ...
       YL14,YL15,YL16,YL17,YL18,YL19,YL20,RMST,RMSL,ISLOP,SLOP, ...
       C,ABC,SLOSS,SLRMS,IPMAX,WZMAX,ESUM,ERIGID,EFLEX
PREPAR YL1,YL2,YL3,YL4,YL5,YL6,YL7,YL8,YL9,YL10,YL11,YL12,YL13, ...
       YL14,YL15,YL16,YL17,YL18,YL19,YL20,RMST,RMSL,SLOP,ESUM, ...
      EL1,EL2,EL3,EL4,EL5,EL6,EL7,EL8,EL9,EL10,EL11,EL12,EL13, ...
      EL14,EL15,EL16,EL17,EL18,EL19,EL20,SLOSS,SLRMS,WZMAX, ...
      ESUM,ERIGID,EFLEX
DERIVATIVE GRP
      YD1=1.0
      Y1=INTEG(YD1,0.0)
END
END
TERMINAL
FIN..CONTINUE
      CALL GRR
END
END
```

Appendix A--Local Slope and Scan Loss Program

```
START
$ADD SPS.MPTGP
$ADD SPS.MPTEVT
    1 6024 6045 6025    3 6023 6044 6024    5 6022 6043 6023    7 6021 6042 6022
    9 2021 2041 6021   11 2022 2042 2021   13 2023 2043 2022   15 2024 2044 2023
   17 2025 2045 2024   19 7044 6024 7045   21 7043 6023 7044   23 7042 6022 7043
   25 3041 6021 7042   27 3042 2021 3041   29 3043 2022 3042   31 3044 2023 3043
   33 3045 2024 3044   35 7063 7044 7064   37 7062 7043 7063   40 7061 7042 7062
   42 3061 3041 7061   44 3062 3042 3061   46 3063 3043 3062   48 3064 3044 3063
   51 7083 7063 7084   53 7082 7062 7083   55 3081 7061 7082   57 3082 3061 3081
   59 3083 3062 3082   61 3084 3063 3083   64 7102 7083 7103   66 7101 7082 7102
   68 3101 3081 7101   70 3102 3082 3103   72 3103 3083 3104   74 6044 6064 6045
   76 6043 6063 6044   78 6042 6062 6043   80 6041 6061 6042   82 2042 2061 2041
   84 2043 2062 2042   86 2044 2063 2043   88 2045 2064 2044   89 6063 6084 6064
   91 6062 6083 6063   93 6061 6082 6062   95 2061 2081 6061   97 2062 2082 2061
   99 2063 2083 2062  101 2064 2084 2063  102 6083 6103 6064  104 6082 6102 6083
  106 2061 6101 6062  108 2082 2101 2061  110 2083 2102 2062  112 2084 2103 2083
  113 6102 6123 6103  115 6101 6124 6102  117 2101 2121 6101  119 2102 2122 2101
  121 2103 2123 2102
FACTOR(.75)
LABEL MODAL COORDINATES
GRAPH T,YL7,YL8,YL9
LABEL MODAL COORDINATES
GRAPH T,YL10,YL11,YL12
LABEL MODAL COORDINATES
GRAPH T,YL13,YL14,YL15,YL16
LABEL MODAL COORDINATES
GRAPH T,YL17,YL18,YL19,YL20
LABEL KINETIC AND POTENTIAL ENERGY
GRAPH T,EL7,EL8,EL9,EL10
LABEL KINETIC AND POTENTIAL ENERGY
GRAPH T,EL11,EL12,EL13,EL14
LABEL KINETIC AND POTENTIAL ENERGY
GRAPH T,EL15,EL16,EL17,EL18
LABEL KINETIC AND POTENTIAL ENERGY
GRAPH T,EL19,EL20
LABEL KINETIC AND POTENTIAL ENERGY
GRAPH T,ESUM,ENIGID,EFLEX
LABEL MAX OUT-OF-PLAN DISPLACEMENT
GRAPH T,DZMAX
LABEL ANG DEV IN DEG - RMS RUNNING AVE, RMS SPATIAL AVE, MAX
GRAPH T,RMST,RMSL,SLOP
LABEL PERCENT SCAN LOSS AND RMS SCAN LOSS
GRAPH T,SLOSS,SLRMS
STOP
$EDIT 23.,SPS.28
$EOF
$FIN
```

Appendix B

3-D Plotting Program of Spatial Surfaces

```
@RUN,/R SPSAN,J8C2GL,SOLAR,3,200/9999,,198/658    .SJW
@ASG,A SPS.
@FOR,IS MAIN
      PARAMETER NP=166,NM=20,NC=272,NPLOT=8,NM2=10,NPLOT2=16
      REAL RX(NP),RY(NP),RZ(NP),Y(NM),YEQU(NPLOT2,NM2)
      REAL UX(NP),UY(NP),UZ(NP),T1(NP,NM),T2(NP,NM),T3(NP,NM)
      INTEGER SEQ(NC),SEQ1(NP)
C
C     NP=NUMBER OF NODES
C     NM=NUMBER OF MODES
C     NC=NUMBER OF PLOT COMMANDS
C     NPLOT=NUMBER OF PLOTS
C     NM2=NM/2
C     NPLOT2=NPLOT*2
      NM21=NM2+1
      DR=3.1416/180.0
      CALL PLOTS
      CALL PLOT(6.0,4.0,-3)
      CALL FACTOR(0.5)
C     READ GRID
      DO 5 I=1,4
      READ(5,333,ERR=5) RX(I),RY(I),RZ(I)
5     CONTINUE
      DO 10 I=1,NP
      READ(5,333) SEQ1(I),RX(I),RY(I),RZ(I)
333   FORMAT(I5,3F15.1)
10    CONTINUE
C     READ PLOT COMMAND SEQUENCE
      READ(5,334)(SEQ(J),J=1,NC)
334   FORMAT(16I5)
C     READ EIGENVECTORS
      DO 20 K=1,NM
      DO 22 I=1,3
      READ(5,335,ERR=22) T1(I,K),T2(I,K),T3(I,K)
22    CONTINUE
335   FORMAT(8X,E12.1,2E15.1)
      DO 20 I=1,NP
   20 READ(5,335) T1(I,K),T2(I,K),T3(I,K)
      READ(5,336) ((YEQU(I,J),J=1,NM2),I=1,NPLOT2)
  336 FORMAT(10E12.6)
      DO 30 I=1,NPLOT
      DO 25 J=1,NM2
      Y(J)=YEQU(I,J)
   25 CONTINUE
      DO 27 J=NM21,NM
      Y(J)=YEQU(NPLOT+I,J-NM2)
   27 CONTINUE
C
```

```
      CALL GRSUM(Y,RX,RY,RZ,T1,T2,T3,UX,UY,UZ)
      CALL DRAW(UX,UY,UZ,SEQ,SEQ1)
      CALL PLOT(10.0,0.0,-3)
   30 CONTINUE
C
      CALL PLOT(10.0,0.0,999)
   50 CONTINUE
      STOP
      END
@FOR,IS SUB1
      SUBROUTINE GRSUM(Y,RX,RY,RZ,T1,T2,T3,UX,UY,UZ)
      PARAMETER NM=20,NP=166
      REAL T1(NP,NM),T2(NP,NM),T3(NP,NM)
      REAL Y(NM),RX(NP),RY(NP),RZ(NP),UX(NP),UY(NP),UZ(NP)
      SCL1=0.005
      SCL2=2.
      DO 5 I=1,NP
      UX(I)=0.0
      UY(I)=0.0
    5 UZ(I)=0.0
      DO 10 K=1,NM
      DO 10 I=1,NP
      UX(I)= UX(I)+ Y(K)*T1(I,K)*SCL2
      UY(I)= UY(I)+ Y(K)*T2(I,K)*SCL2
   10 UZ(I)= UZ(I)+ Y(K)*T3(I,K)*SCL2
      DO 20 I=1,NP
      UX(I)= RX(I)*SCL1 + UX(I)
      UY(I)= RY(I)*SCL1 + UY(I)
   20 UZ(I)= RZ(I)*SCL1 + UZ(I)
      RETURN
      END
@FOR,IS SUB2
      SUBROUTINE DRAW(UX,UY,UZ,SEQ,SEQ1)
      PARAMETER NP=166,NC=272
      REAL UX(NP),UY(NP),UZ(NP)
      INTEGER SEQ(NC),FLAG,SEQ1(NP)
      DO 10 I=1,NC
         J=IABS(SEQ(I))
      DO 5 K=1,NP
      IF(SEQ1(K).EQ.J) KK=K
5     CONTINUE
         FLAG=2
         IF(SEQ(I).LT.0) FLAG=3
      X = UX(KK)
      Y=UY(KK)
      Z=UZ(KK)
      CALL TRANS(X,Y,Z,XP,YP)
      CALL PLOT(XP,YP,FLAG)
   10 CONTINUE
      RETURN
      END
```

Appendix B--3-D Plotting Program of Spatial Surfaces

```
@FOR,IS SUB3
      SUBROUTINE TRANS(X,Y,Z,XP,YP)
      REAL X,Y,Z,XP,YP
      THETA=30.0
      DR=3.1416/180.0
      XP=(X-Y)*COS(THETA*DR)
      YP=(X+Y)*SIN(THETA*DR)+Z
      RETURN
      END
@MAP
 LIB LIB*JPLS,LIB*PLOTS
@XQT
@ADD SPS.MPTGP
-4103 4102 4101  101  102  103  -86   83   82   81 4082 4083 4084-4064 4063 4062
 4061   61   62   63   64  -45   44   43   42   41 4042 4043 4044 4045-4025 4024
 4023 4022 4021   21   22   23   24   25   -6    5    4    3    2    1 4002 4003
 4004 4005 4006-5025 5024 5023 5022 5021 1021 1022 1023 1024 1025-1045 1044 1043
 1042 1041 5042 5043 5044 5045-5064 5063 5062 5061 1061 1062 1063 1064-1084 1083
 1082 1081 5082 5083 5084-5103 5102 5101 1101 1102 1103 1084 1064 1045 1025    2
  -25    5 1024 1044 1063 1083 1102-1101 1082 1062 1043 1023    4   24   45  -64
   44   23    3 1022 1042 1061 1081 5101-5102 5082 5061 1041 1021    2   22   43
   63   84 -103   83   62   42   21    1 5021 5042 5062 5083 5103-5084 5063 5043
 5022 4002 4021   41   61   82  102 -101   81 4061 4042 4022 4003 5023 5044 5064
-5045 5024 4004 4023 4043 4062 4082 4101-4102 4083 4063 4044 4024 4005 5025-4006
 4025 4045 4065 4084 4103 -103   84   64   45   25    6-1025    5   24   44   63
   83  102 -101   82   62   43   23    4 1024 1045-1064 1044 1023    3   22   42
   61   81 4101-4102 4082 4061   41   21    2 1022 1043 1063 1084-1103 1083 1062
 1042 1021    1 4021 4042 4062 4083 4103-4084 4063 4043 4022 4002 5021 1041 1061
 1082 1102-1101 1081 5061 5042 5022 4003 4023 4044 4064-4045 4024 4004 5023 5043
 5062 5082 5101-5102 5083 5063 5044 5024 4005 4025-4006 5025 5045 5064 5084 5103
@ADD SPS.MPTEVT
@ADD SPS.28
@FIN                                                                    NIF$
```